

Федеральное государственное автономное образовательное учреждение  
высшего образования «Уральский федеральный университет имени первого  
Президента России Б.Н. Ельцина»  
Уральский энергетический институт  
Кафедра «Электропривод и автоматизация промышленных установок»

На правах рукописи

Текле Самуэль Исаак

**РАЗРАБОТКА И ИССЛЕДОВАНИЕ МЕТОДОВ  
ДИАГНОСТИКИ И ПОВЫШЕНИЯ  
ЭНЕРГОЭФФЕКТИВНОСТИ ШТАНГОВЫХ  
ГЛУБИННО-НАСОСНЫХ УСТАНОВОК С ПРИВОДОМ ОТ  
АСИНХРОННОГО ДВИГАТЕЛЯ**

2.4.2. Электротехнические комплексы и системы

**ДИССЕРТАЦИЯ**

на соискание учёной степени

кандидата технических наук

Научный руководитель:  
доктор технических наук, доцент  
Зюзов Анатолий Михайлович

Екатеринбург — 2023

Federal State Autonomous Educational Institution Higher Education «Ural Federal  
University named after the first President of Russia B.N. Yeltsin»  
Ural Power Engineering Institute  
Department of «Electric Drive and Automation of Industrial Plants»

As a manuscript

Tecele Samuel Isaac

**DEVELOPMENT AND RESEARCH ON FAULT DIAGNOSIS  
AND ENERGY EFFICIENCY IMPROVEMENT METHODS  
FOR SUCKER ROD PUMPS DRIVEN BY AN INDUCTION  
MOTOR**

2.4.2. Electrotechnical complexes and systems

DISSERTATION

Degree of Candidate of Technical Sciences

Scientific supervisor:

Doctor of Technical Sciences, Associate Professor

Ziuzev Anatolii Michaelovich

Yekaterinburg — 2023

## Table of Contents

	Page
<b>Introduction</b> . . . . .	7
<b>Chapter 1. Sucker Rod Pump Modeling and Analysis</b> . . . . .	13
1.1 Introduction . . . . .	13
1.2 Artificial Lifting Methods . . . . .	13
1.2.1 Sucker Rod Pump . . . . .	14
1.2.2 Hydraulic Pump . . . . .	15
1.2.3 Progressive Cavity Pump . . . . .	17
1.2.4 Electric Submersible Pump . . . . .	18
1.2.5 Selection Guide . . . . .	19
1.3 Sucker Rod Pump Components . . . . .	21
1.4 Mathematical Modeling of Sucker Rod Pump . . . . .	22
1.4.1 Sucker Rod String . . . . .	22
1.4.2 Surface Model . . . . .	23
1.4.3 Subsurface Pump Model . . . . .	28
1.4.4 Reservoir Model . . . . .	30
1.5 Simulation Results . . . . .	31
1.6 Summary . . . . .	38
<b>Chapter 2. Sucker Rod Pump Working State Diagnosis</b> . . . . .	41
2.1 Introduction . . . . .	41
2.2 Sucker Rod Pump Operation Analysis . . . . .	42
2.3 Sucker Rod Pump Working States and Characteristics . . . . .	43
2.4 Review on Sucker Rod Pump Monitoring and Diagnosis . . . . .	45
2.4.1 Monitoring Sucker Rod Pump Operating Condition . . . . .	45
2.4.2 Sensor Based Measurements . . . . .	48

	Page	
2.4.3	Inferring Polished Rod Load and Displacement from Estimated Rotor Speed and Torque . . . . .	50
2.5	Computer Aided Diagnostic System . . . . .	51
2.5.1	Feature Extraction . . . . .	53
2.5.2	SVM Based Diagnostic Model . . . . .	54
2.6	Simulation Results . . . . .	59
2.6.1	Training Data Generation . . . . .	59
2.6.2	Diagnosis . . . . .	61
2.7	Summary . . . . .	63
 <b>Chapter 3. Optimal Energy Efficiency Operation of Sucker Rod Pump . . .</b>		<b>66</b>
3.1	Introduction . . . . .	66
3.2	Sucker Rod Pump Drive's Power Requirement . . . . .	66
3.2.1	Subsurface Energy Losses . . . . .	67
3.2.2	The Surface Transmission Energy Losses . . . . .	68
3.2.3	Optimal Counterbalance . . . . .	69
3.2.4	Reducing Inertial Torque . . . . .	72
3.2.5	Sucker Rod Pump Prime Movers . . . . .	72
3.3	Review of Efficiency Optimization Methods for Induction Motor . . . .	75
3.4	Modeling Adjustable Speed Drive Based on Induction Motor . . . . .	78
3.4.1	Switching Network . . . . .	79
3.4.2	PWM Boost Rectifier Modeling . . . . .	81
3.4.3	Control Strategies for Boost Rectifier . . . . .	83
3.4.4	Modeling Voltage Source Inverter Fed Induction Motor . . . . .	85
3.5	Loss Model and Optimal Magnetizing Current Generation . . . . .	91
3.5.1	Derivation of Loss Equation . . . . .	91
3.5.2	Optimal Magnetizing Current Generation in Steady State . . . .	92

	Page
3.5.3 Optimal Magnetizing Current Generation under Voltage and Current Constraints . . . . .	93
3.5.4 Optimal Magnetizing Current Generation for Sucker Rod Pump Applications . . . . .	96
3.6 Simulation Results . . . . .	99
3.7 Summary . . . . .	103
<b>Chapter 4. Emulating Sucker Rod Pump Dynamics . . . . .</b>	<b>104</b>
4.1 Introduction . . . . .	104
4.2 Motivation for Sucker Rod Pump Emulation . . . . .	104
4.3 Test Bench Configuration and Dynamics . . . . .	106
4.4 Review on Dynamometer Control Strategies for Emulating Mechanical Loads . . . . .	107
4.4.1 Principle of Inverse Mechanical Dynamics . . . . .	108
4.4.2 Feed Forward Speed Tracking with Analytical Compensator . . . . .	110
4.4.3 Nonlinear Control Based Speed Tracking . . . . .	111
4.5 An Approach for Emulating Sucker Rod Pump Dynamics in Reduced Scale . . . . .	114
4.6 Experimental Test Bench . . . . .	117
4.6.1 Overview of Experimental Test Bench . . . . .	117
4.6.2 Sucker Rod Pump Real Time Simulator . . . . .	118
4.6.3 ABB ACS 580 . . . . .	120
4.6.4 Current, Voltage, Torque, and Speed Measurement . . . . .	121
4.6.5 Creation of Surface Dynamometer Card from Motor Measurements . . . . .	122
4.7 Experimental Results . . . . .	124
4.8 Emulating the Sucker Rod Pump Using PHiL Simulator . . . . .	126
4.9 Summary . . . . .	133

	Page
<b>Conclusion</b> . . . . .	134
<b>References</b> . . . . .	137
<b>Appendix A. Sucker Rod Pump Simulator: program registration and Its Interface</b> . . . . .	153
<b>Appendix B. Implementation of Results</b> . . . . .	156

## Introduction

**Relevance of the topic.** Oil continues to account one of the largest shares of global primary energy. According to BP's report in 2022 [1], oil production in 2021 remains high (89.877 million barrels per day) with the largest producers: USA (16.585 million barrels per day) and Russian Federation (10.944 million barrels per day). In [2], it is reported that more than 70% of the existing oil producing wells employ artificial methods to lift oil to the surface. Majority of the installations use sucker rod pumping system, which is the earliest artificial oil extraction method [3; 4]. Sucker rod pump system has already come to full development and offers low comprehensive cost, simplicity, and adaptability to wide range of production rates. However, still there is demand for research to find ways for improving its operational performance.

One way of achieving this objective is through development of efficient monitoring and diagnostic systems. The sucker rod pump has subsurface parts, which work thousands of meters dip in underground under severe circumstances. Consequently, the failure rate of the subsurface parts is expected to be high. The report in [5] about failure analysis of sucker rod pump indicates that majority of failures are associated with subsurface pump, sucker rod string or tubing string. Due to the subsurface component failure or unstable liquid supply, many faulty working states are likely to occur. Operation at some faulty working state may cause abnormal event advancement, economic loss, and invisible danger. The dynamometer card (a closed locus, which shows relation between the polished rod displacement and load) has been the primary tool for detecting subsurface working state in oil engineering since 1963 [6]. Different working conditions of sucker rod pumping systems can be distinctly recognized by the shapes of dynamometer card [7]. In the conventional diagnosis approach, skilled staff can diagnose the subsurface working state based on the shape of dynamometer card. However, diagnosis based on this method is inefficient because its accuracy is affected by the personal know-how of the technical staff and does not support a means for real time monitoring. Moreover, diagnosis based on

dynamometer card relies on unreliable sensors. On the other hand, the motor power curve is a promising alternative evidence to dynamometer card. It is informational but diagnosis based on motor power curve requires computer aided techniques, which have attracted much research attention.

Another heavily discussed problem in literature is the power requirement of sucker rod pump drive, which is more complicated due to the nature of gearbox's torque loading during the pumping cycle. In sucker rod pump installations, the power bill is occupying a commanding part of the operating cost [8]. Therefore, a reduction in operating cost can be obtained by reducing the energy consumption of the sucker rod pump drive. Since, there are large number of sucker rod pump installations worldwide, any effort which saves energy consumption will produce considerable economic benefit and help to meet the energy efficiency targets and standards.

Several techniques have been developed to save energy consumption in sucker rod pump installations. The effect of counterbalance and choice of pumping mode (combination of plunger size, stroke length, pumping speed) on the power requirement has been discussed in [4]. Considerable energy saving has been achieved by means of power off control, which was implemented in [9] by monitoring the position of the polished rod. However, the practical application of this technique is limited to loads which contain generation mode. The pumpoff control based on monitoring liquid level introduced in [10] also enables to save some energy when inadequate liquid level is examined. However, this method is not suitable for wells with water flooding. Multi-function energy saving device that incorporates power off control, wye delta automatic conversion and auto reactive power compensation, has been developed in [11]. This method is applicable for different kinds of load profiles: light load with generator mode, light load without generator mode, heavy load with generator mode, heavy load without generator mode. Operating cost reduction by adapting some control strategies that minimize motor losses is also another achievable solution.

Research related to easing the experimentation of many mechanical systems has also attracted research attention. The sucker rod pump is one of them. Due to space and financial reasons, it is impractical to keep the sucker rod pump in laboratory for

experimental purpose. However, in different way, the experimentation task can be carried out in laboratory by employing alternate facilities such as electromechanical test bench, Hardware-In-Loop (HiL) with its extension Power Hardware-In-Loop (PHiL) and their combination.

**The degree of elaboration of the research topic.** The sucker rod pump is the leading artificial lifting method in the oil and gas industry. For the development of sucker rod pump installations, significant contribution in connection to modeling, monitoring and diagnosis, design and production cost analysis have been made by Russian and foreign researchers: R.T. Akhmetgaryaev, E.M. Solodkiy, G. Guluyev, V.B. Sadov, I.N. Shardakov, S. G. Gibbs, Tackas Gobar, A Koncz, S. Miska, B.M. Wilamowski, L. H. Torres, B. Ordonez, M. Xing, G. Xianwen, S. Dong, Z. Boyuan, X. Sun, F. ZiMing, X.Liu etc. The energy efficiency optimization of electrical drives in general has also been the focus of many researcher such as V. N. Polykov, R.T. Shirener. This indicates that there is a potential for research in this research direction.

**Goal of dissertation work** is to develop fault diagnostic and efficiency improvement methods for sucker rod pumps driven by an induction motor. To achieve these goals, the following tasks were set and solved. **Tasks:**

1. Development of an integrated sucker rod pump simulation model that enable to simulate different working states.
2. Building a training set using feature vectors extracted from samples of motor power curve and developing a diagnostic model for sucker rod pump.
3. Development of a special strategy for generating magnetizing current trajectory to command a vector control system of frequency-controlled induction motor drive for sucker rod pump and evaluation of its effectiveness.
4. Development of real time simulators for sucker rod pump drive.

**Scientific novelty** of the work is as follows:

1. An integrated sucker rod pump simulation model, which enables to reproduce different sucker rod pump working states, has been developed in MATLAB.

2. A fault diagnosis model for sucker rod pump has been developed based on motor power curves and Support Vector Machine (SVM) by constructing a training set with the help of sucker rod pump simulation model.
3. A special strategy for generating magnetizing current trajectory, which provides some reduction in energy consumption, is proposed for an induction motor controlled based on vector control system and driving sucker rod pump.
4. A real time sucker rod pump simulation model has been developed in LabVIEW programming environment and on its bases electromechanical test bench has been constructed for emulating the sucker rod pump dynamics.
5. A strategy for controlling load machine in electromechanical test bench was proposed and implemented for emulating sucker rod pump (in reduced scale).

**Theoretical significance of the work** consists of the development of mathematical and simulation model of sucker rod pump drive, which allow to conduct a detailed study on operation and different working states of the sucker rod pump and proposed methods to solve problems in sucker rod pump related to reducing energy consumption and building training set, which is useful in developing computer aided diagnostic methods.

**Practical significance of the work** includes development of diagnostic algorithms, which are essential for developing intelligent diagnostic system for sucker rod pump installations and real time sucker rod pump simulator, which is fundamental to construct a test bench for studying the performance of sucker rod pump. In addition, the sucker rod pump emulator can be used for conducting studies aimed at improving the efficiency of rod pump electric drives.

**The main provisions of the dissertation submitted for defense:**

1. The developed sucker rod pump simulation model for generating samples of motor power curve representing its different working states.
2. Fault diagnostic model based on motor power curve and SVM.
3. A special procedure for generating magnetizing current trajectory, which reduces energy consumption for an induction motor controlled based on vector control system and driving sucker rod pump.

4. The real time model of sucker rod pump in LabVIEW programming environment.
5. The load machine control strategy for emulating sucker rod pump (in reduced scale).

**Dissertation research methods.** In the dissertation work, theoretical and experimental research methods are used to solve the specified tasks. Theoretical research is based on the provisions of theory of electric drives, electrical machines, mechanics, automatic control systems, differential equations, methods of numerical integration, direct and inverse Laplace transform, optimization methods such as Lagrange. Experimental methods include computer simulation and electromechanical test bench. The following software products were used in the studies: MATLAB R2019b, LabVIEW 8.0.

**Degree of reliability of scientific research and results.** The diagnosis part of dissertation work is based on motor power curve, in which its characteristics can be directly related to subsurface pump operation. The motor power curve is periodic with period equal to the period of one cycle of pump operation and it reflects the effects of different forces exerted on the surface and subsurface components along their corresponding time. The development and research of a strategy to reduce energy consumption is based on minimizing motor current by acting on magnetizing current, which is widely accepted method. The results of experiment from the electromechanical test bench validate the accuracy of the developed simulation model. The shape of the dynamometer card calculated using the motor measurements show that the simulated working states by the real time simulator are correctly reflected on the drive machine.

**Implementation of work results.** The results presented in this work were used in testing mobile wattmetering system for oil production facilities of type СК ШС-2 (ПКБСК) manufactured by «БОЛЬШИЕ СИСТЕМЫ».

**Approbation of work.** The main results of this work were reported at 6 conferences listed below:

- 2019 IEEE Russian Workshop on Power Engineering and Automation of Metallurgy Industry: Research and Practice (PEAMI), Magnitogorsk, Russia.

- 2020 27th International Workshop on Electric Drives: MPEI Department of Electric Drives 90th Anniversary (IWED), Moscow, Russia.
- 2020 XI International Conference on Electrical Power Drive Systems (ICEPDS), St. Petersburg, Russia.
- 2020 IEEE Russian Workshop on Power Engineering and Automation of Metallurgy Industry: Research and Practice (PEAMI), Magnitogorsk, Russia.
- 2021 XVIII International Scientific Technical Conference Alternating Current Electric Drives (ACED), Ekaterinburg, Russia.
- 2022 29th International Workshop on Electric Drives: Advances in Power Electronics for Electric Drives (IWED), Moscow, Russia.

**Personal contribution.** The author has taken an active part in developing a fault diagnostic model, control strategy for optimal energy efficiency and an emulating system for a sucker rod pump.

**Publication.** The main results on the topic of the dissertation are presented in 11 printed publications, 1 of which is published in journals recommended by BAK, 2 — in periodical scientific journals indexed by Web of Science and Scopus, 8 — in conference presentations. Registered 1 program for ЭBM.

**The structure and scope of the thesis.** The dissertation consists of an introduction, 4 chapters, a conclusion and 2 appendices. In total, the dissertation has 156 pages, including 88 figures and 10 tables. The reference list contains 131 items.

## **Chapter 1. Sucker Rod Pump Modeling and Analysis**

### **1.1 Introduction**

A number of oil extraction (lifting) methods have been invented in the oil and gas industry. However, it must be noted that the choice of oil extraction method significantly influences the long term revenue of an oil field. The present chapter reviews some of the lifting methods but the sucker rod pump is the object of this thesis.

Diagnosis, optimization of production rate and energy efficiency of sucker rod pump installations are most favored research areas. For this purpose, it is essential to accurately predict the operating conditions of sucker rod pump. This chapter presents detailed mathematical model of surface components, subsurface components and reservoir. Integrating all these models, the operating conditions of the sucker rod pump can be predicted accurately.

### **1.2 Artificial Lifting Methods**

Wide range of artificial lift methods have been invented to maximize the oil recovery process. Generally, they can be classified into a group which use pump placed below liquid level and another group which use compressed air, injected in the well stream at some downhole point [3]. For different oil field conditions such as well depth, desired production rates, fluid properties, etc, there are more than one choices from the group which employ subsurface pump. However, it must be noted that the selection of proper lifting method for a given well requires more than comparing the production capabilities and efficiencies, because the choice significantly determines the long-term incomes of the oil field.

### 1.2.1 Sucker Rod Pump

Sucker rod pump also known as walking beam pumping is the oldest and most widely used lifting method [3; 12]. The main elements which make the sucker rod pumping system are prime mover, V-belt, gearbox, surface pumping equipment, sucker rod string, the subsurface pump assembly, and the tubing string. The different components of sucker rod pump system are indicated in Fig. 1.1. The prime mover, V-

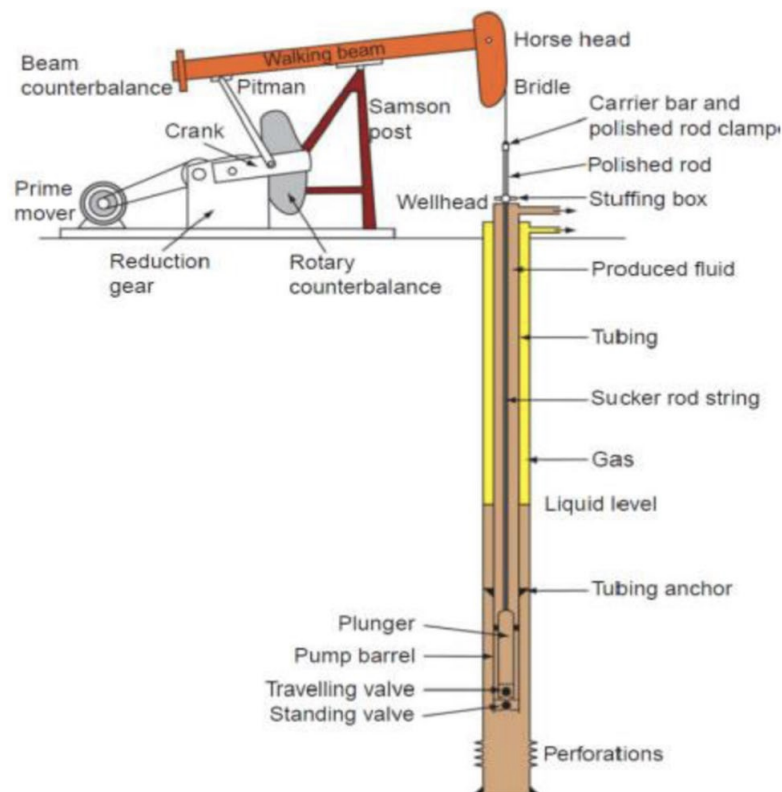


Fig. 1.1 — Sucker rod pump components[13]

belt, gearbox, and the pumping unit work together to produce an up and down movement of desired speed at the polished rod. This reciprocating movement is passed to the subsurface pump, which employs positive displacement pump, through the sucker rod string. This action helps to suck fluid and bring it to the surface.

Based on the size and application, the pumping unit can have different design types (B, C, A, M, TM) [2; 3]. The conventional design type is designated by types B or C. Type B represents for beam balanced arrangement while type C represents for crank balanced arrangement. In these design types, the horsehead is on the opposite side of

the driven part of the walking beam. Type B and C can be driven either clockwise or anticlockwise. Unfortunately, due to their structural and dynamic property, the energy consumption for types B and C is higher. In type A, which is also called air balanced, the conventional type design is modified in such a way that the total weight is reduced. Type M and TM designs provide a lower torque and power requirement than conventional type. However, these two designs can only be driven in one direction. Changes in the balance block are nonlinear and it cannot fully balance with the polished rod load. To meet the demand of technical parameters with characteristics of smooth motion and efficient energy saving, a four bar pumping unit was designed in [14].

The main reasons why sucker rod pump is still in wide use are its availability in many different sizes and material combinations, simple technical installation, relatively good overall efficiency and simple adjustment of the operation parameters [15; 16]. However, due to limitation in strength of steel materials used in rod manufacturing, the sucker rod pump requires certain load reduction arrangement when employed for deep pumping.

### **1.2.2 Hydraulic Pump**

Hydraulic pumping is one of the widely accepted lifting method since 1930 [17]. It integrates several different systems for treating problems created due to corrosion, paraffin, emulsions, salt deposits, high viscosity of the produced fluid [18]. Hydraulic pumping systems do not use connecting rod to activate the subsurface pump. Instead, they use power fluid to transmit power generated by the surface pump to the subsurface pump, which employs either piston pump or jet pump to convert the energy in the power fluid into the energy required to lift fluid to the surface. Fig. 1.2 and Fig. 1.3 show arrangement for piston pump and a jet pump assembly respectively.

In Fig. 1.2 a and b, the power fluid at high pressure is guided through the pressure pipe (3) to the hydro motor (4), which is rigidly connected to the piston of well pump (5). This action enables the piston pump to suck and lift oil to the surface. In case

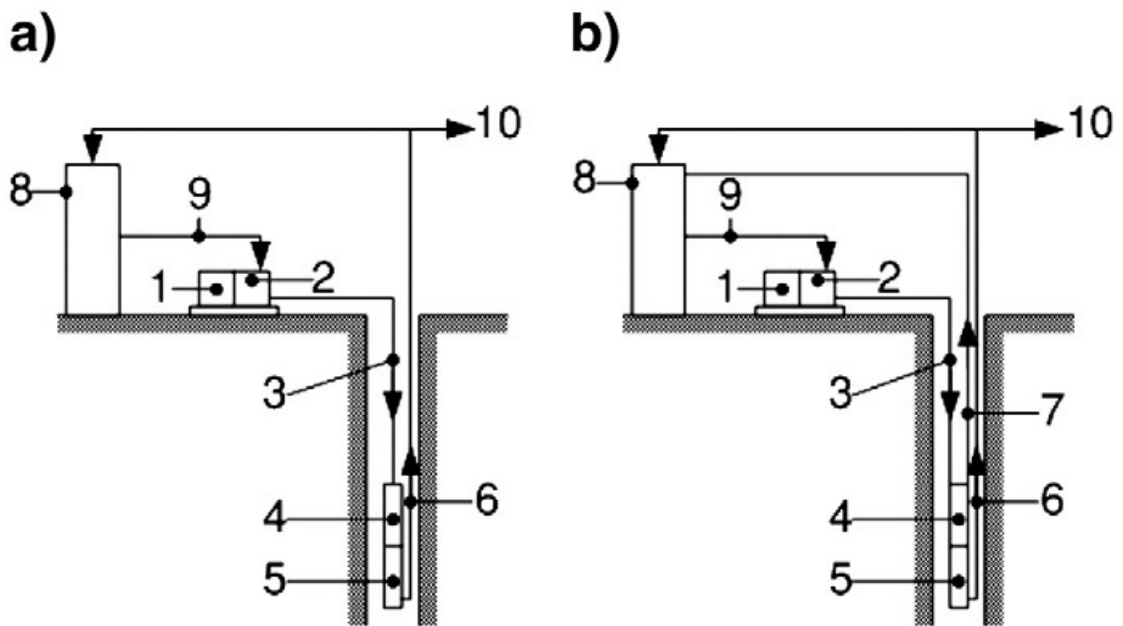


Fig. 1.2 — Piston pump [19]. a. open fluid circulation b. closed fluid circulation

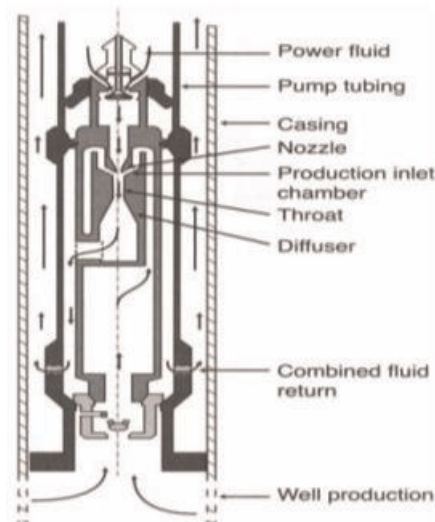


Fig. 1.3 — Jet pump [20]

of open fluid circulation (Fig.1.2a), the power fluid returns mixed with the produced fluid through discharge pipe (6). However, in case of closed fluid circulation (Fig. 1.2b), the power fluid returns through a separate return pipe (7). The processing and preparation facilities at the surface produce the required amount of power fluid for another new energy conversion cycle in case of open fluid circulation. However, for the case with closed fluid circulation only small amount to compensate the power fluid loss is required.

The jet pump assembly contains nozzle, throat and diffuser to convert first high pressure power fluid flow to high velocity flow which induces low pressure sufficient to entrain fluid from its suction section, and then to high pressure mixed fluid flow.

Although the initial cost of hydraulic pump systems is high but it has got good application where other lifting methods are not suitable due to the advantages listed in [18]:

- adjustable production rate,
- provides corrosion control,
- handles viscous oil very well,
- handles paraffin, solids, and gas,
- suitable for deeper and deviated wells.

### **1.2.3 Progressive Cavity Pump**

Progressive cavity pump(PCP) consists of prime mover, sucker rod string, production tubing and pump assembly. The pump assembly consists of stator and rotor but no valves [3]. The stator is fixed to the production tubing whereas rotor is connected to the sucker rod string, which is rotated by the prime mover. When the rotor is rapidly rotated, pumping action is produced and hence fluid is lifted to the surface. Fig. 1.4 illustrates the basic surface driven PCP configuration.

Progressive cavity pump owns commonly needed merits such as simple installation, low capital cost, low operating cost, high total system efficiency as a result of its unique design features. Progressive cavity pump is suitable in application where it is required to handle high viscous fluids, sand/solid matters, high percentage of free gas. However, certain considerations such as pumping depth, temperature capability, production rates, fluid level have to be taken into account during selection.

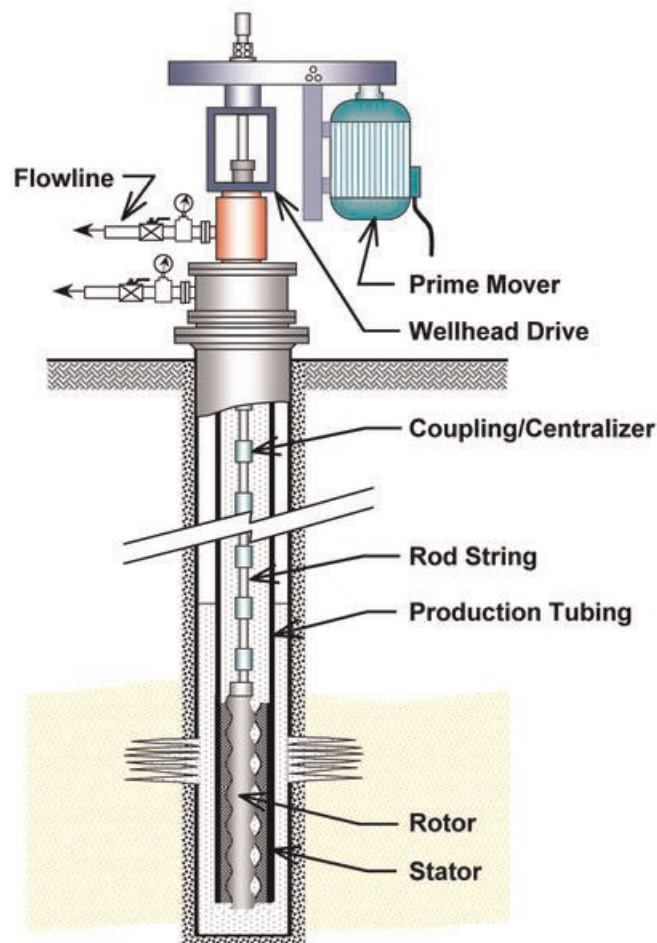


Fig. 1.4 — Progressive cavity pump [21]

#### 1.2.4 Electric Submersible Pump

Electric submersible pump (ESP) shown in Fig. 1.5 is a type of oil lifting method that utilize a multistage centrifugal pumps to lift oil to the surface by producing centrifugal force. The ESP system consists of surface and subsurface equipment. The surface equipment include transformer, motor controller, ESP well head, adjustable speed drive. The subsurface equipment includes three phase electric motor, seal section (protector), pump intake, multistage centrifugal pump, electric power cable and cable bands. Each stage is stacked on the shaft and compressed in the housing. Each stage consists of a rotating impeller and a stationary diffuser.

ESP is a perfect choice when the application requires high volume and depth capability. Moreover, it is suitable for deviated wells. However, the major disadvantage of ESP is that it has limited adaptability to major changes in reservoir and its

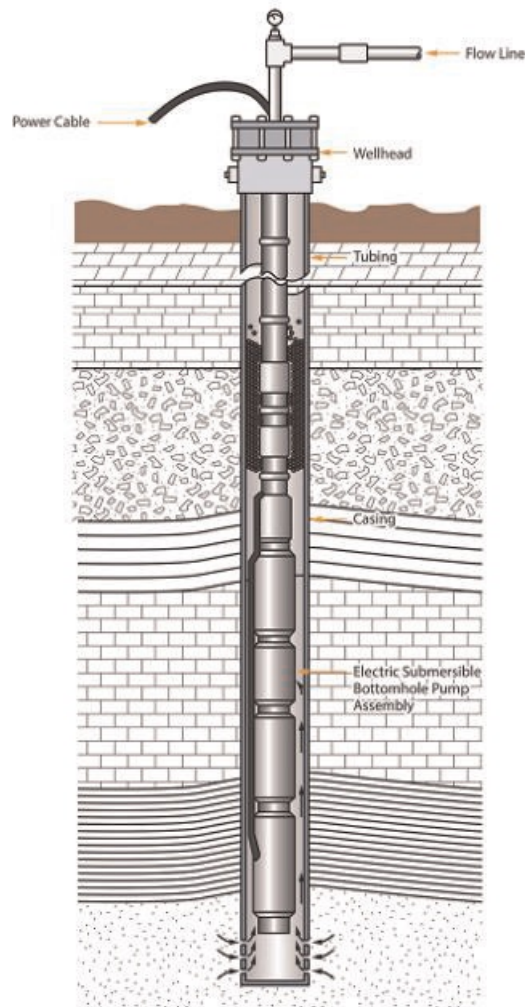


Fig. 1.5 — Electric submersible pump [22]

maintenance cost is high. It is not easy to run in high viscous fluids and is also sensitive to free gas and/or abrasives.

### 1.2.5 Selection Guide

During selection of artificial lifting methods, the objective is to select an artificial lifting method that can: give maximum production rate, provide flexibility in production rate, increase reliability and uptime, have lowest purchase and operating cost and minimum footprint. However, every artificial lift method has some advantages and disadvantages. Therefore, certain criteria's such as operating depth, operating volume, operating temperature, corrosion handling, gas handling, solid handling, servicing,

prime mover, offshore application, overall system efficiency can be used during selection. Table 1 gives comparison of the different artificial lifting methods based on the given criteria.

Table 1 — Selection guide lines [17]

Criteria	Rod lift	PCP	Gas lift	plunger lift	Hydr. piston	Hydr. jet	ESP
Max. operating depth(m)	16000	6000	15000	19000	17000	15000	15000
Operating volume(BDP)	to 5000	to 4500	to 30000	50	50 to 4000	300 to 15000	200 to 30000
Operating temperature (oF)	100/500	75/250	100/400	120/500	100/500	100/500	100/400
Corrosion handling	good to excellent	fair	good to excellent	excellent	good	excellent	good
gas handling	fair to good	fair	excellent	excellent	fair	good	poor to fair
solid handling	fair to good	excellent	good	poor to fair	poor	good	poor to fair
Fluid gravity(oAPI)	> 8	< 35	< 35	1*	> 8	> 8	> 10
servicing	Workover or pulling rig	Workover or pulling rig	Wireline or workover	Wellhead catcher or wireline	Hydraulic or wireline	Hydraulic or wireline	Workover or pulling rig
Prime mover	Gas engine or electric	Gas engine or electric	compressor	Well's natural energy	Gas engine or electric	Gas engine or electric	electric motor
Offshore application	limited	good	excellent	N/A	good	excellent	excellent
Overall system efficiency	40-60	40-70	10-30	N/A	45-55	10-30	35-60

1\* – *GLR required 300 scf/bbl/1000/depth*

### 1.3 Sucker Rod Pump Components

The sucker rod pump consists of various surface and subsurface components, which all together function to bring oil from the subsurface to the surface [23]. Most sucker rod pump components are indicated in Fig. 1.1.

The main surface components are:

- Prime mover is the source of mechanical energy, which is transmitted to the subsurface pump assembly through the shaft, V-belt, gear box, pumping unit, rod string. Either internal combustion engine or induction motors could be selected based on operating cost analysis.
- Gear box helps to reduce the prime mover speed to the desired crank speed. This action increases the gearbox torque.
- Pumping unit is a four-bar linkage mechanism that helps to convert rotational speed at the crank to up and down movement at the polished rod.
- Polished rod is made of a durable material that connects the walking beam with the sucker rod string.
- Counterweight is a certain mass fixed at the crank or walking beam to smooth load on the prime mover.

The main subsurface components are:

- Sucker rod string is a long slender that reciprocates inside a tubing. At the upper end it is connected to the polished rod while at the lower end it is connected to the plunger of subsurface pump.
- Tubing is the piping which houses the sucker rod string and through it, fluid is produced.
- Subsurface pump is composed of fixed barrel, plunger and two valves (standing valve and traveling valve). This assembly forms a positive displacement pump. The displacement of plunger relative to barrel influences the state of the valves.

## 1.4 Mathematical Modeling of Sucker Rod Pump

The operating process of sucker rod pump is complex that involves multivariable coupling. Hence, derivation of its mathematical model is not easy. The most essential part of sucker rod pump's model is the longitudinal vibration model of sucker rod string, which is a boundary problem. Its solution requires information about the kinematics of the suspension point and load on the plunger.

### 1.4.1 Sucker Rod String

The most important physical property of the sucker rod string is elasticity. Due to this physical property, the impact of any load applied to the polished rod due to the effects of the pumping unit's motion is transmitted to the subsurface. Likewise, the impact of different loads in the subsurface are reflected on the polished rod load as well as at the input of the prime mover. The accuracy acquired when designing or studying sucker rod pump installations depends on how exactly the sucker rod string's physical property is simulated. The wave equation is the most recommended mathematical model to describe the sucker rod string's dynamic nature. The wave equation in which its derivation can be found in [3; 24] is given by:

$$\frac{\partial^2 u}{\partial t^2} = \frac{E_r}{\rho} \frac{\partial^2 u}{\partial x^2} - \frac{v_e}{\rho A_r} \frac{\partial u}{\partial t}, \quad (1.1)$$

where:  $\sqrt{\frac{E_r}{\rho}}$  – equal to the speed of stress waves,

$v_e$  – viscous damping coefficient per unit length of sucker rod string,

$E_r$  – Young's modulus of elasticity for rod material,

$\rho$  – the density of the rod material,

$A_r$  – cross-sectional area of the rod,

$\frac{\partial u}{\partial x}$  – change of the rod displacement over the rod length,

$\frac{\partial u}{\partial t}$  – shear velocity between the fluid and the rods.

The physical property of the sucker rod string can also be described by considering the sucker rod string as a dispersed spring-mass-damper system as shown in Fig.1.6. Rod-fluid-tubing viscous friction and rod-tubing Coulomb friction have influence on the accuracy of the developed model. These effects have been considered in [25–28]. Recent excellent surveys [29–32] have also examined the impact of rod buckling. In this thesis the effect of rod buckling on sucker rod string's longitudinal vibration is neglected and the sucker rod string model is described by constant stiffness and damping coefficients. Based on these assumptions, the behavior of sucker rod string can be described by:

$$\begin{aligned}
m_1\ddot{u}_1 &= K_0(u_0 - u_1) - K_1(u_2 - u_1) + C_0(\dot{u}_0 - \dot{u}_1) - C_1(\dot{u}_2 - \dot{u}_1), \\
m_2\ddot{u}_2 &= K_1(u_1 - u_2) - K_2(u_3 - u_2) + C_1(\dot{u}_1 - \dot{u}_2) - C_2(\dot{u}_3 - \dot{u}_2), \\
&\vdots \\
m_{n-1}\ddot{u}_{n-1} &= K_{n-2}(u_{n-2} - u_{n-1}) - K_{n-1}(u_n - u_{n-1}) + \\
&\quad C_{n-2}(\dot{u}_{n-2} - \dot{u}_{n-1}) - C_{n-1}(\dot{u}_n - \dot{u}_{n-1}), \\
m_n\ddot{u}_n &= K_{n-1}(u_{n-1} - u_n) + C_{n-1}(\dot{u}_{n-1} - \dot{u}_n) - F_{pl}(t),
\end{aligned} \tag{1.2}$$

where :  $m_i$  – the mass of the  $i^{th}$  element,

$u_i$  – the displacement of the  $i^{th}$  element,

$K_i$  – the stiffness coefficient of the  $i^{th}$  element,

$C_i$  – the damping coefficient of the  $i^{th}$  element,

$F_{pl}$  – the load on the plunger.

Equation (1.2) is a boundary problem and uses the surface and subsurface models as boundary conditions.

### 1.4.2 Surface Model

The prime mover, gear reducer and the pumping unit are the main elements of the sucker rod pump in the surface.

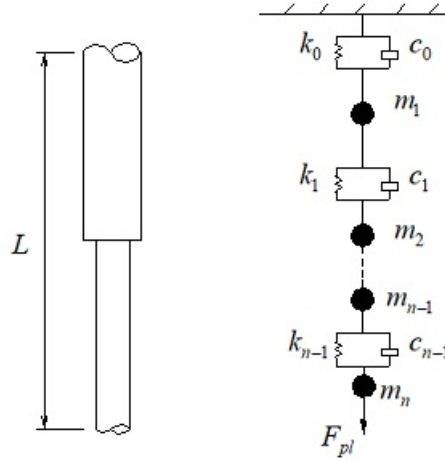


Fig. 1.6 — Sucker rod string

**Prime mover.** The prime mover is the source of mechanical energy. Internal combustion engine or electric motors can produce the required mechanical energy but the choice depends on several factors. The operational characteristics of the prime mover matters a lot when choosing prime mover for sucker rod pump application. For example, when the choice is electric motor, induction motor of design D is most preferred choice. The state space model of induction motor in two-phase reference frame [33] is expressed as:

$$\begin{aligned}
 \frac{di_{sd}}{dt} &= -di_{sd} + \omega_s i_{sq} + ci_{md} + c\omega T_r i_{mq} + au_{sd}, \\
 \frac{di_{sq}}{dt} &= -\omega_s i_{sd} - di_{sq} - c\omega T_r i_{md} + ci_{mq} + au_{sq}, \\
 \frac{di_{md}}{dt} &= \frac{1}{T_r} (i_{sd} - i_{md}) + (\omega_s - \omega) i_{mq}, \\
 \frac{di_{mq}}{dt} &= \frac{1}{T_r} (i_{sq} - i_{mq}) + (\omega_s - \omega) i_{md}, \\
 M_e &= 1.5z_p(1 - \sigma)L_s(i_{md}i_{sq} - i_{mq}i_{sd}), \\
 \frac{J_T d\omega}{z_p dt} &= M_e - M_s,
 \end{aligned} \tag{1.3}$$

where:  $(i_{sd}, i_{sq})$ ,  $(i_{md}, i_{mq})$ ,  $(u_{sd}, u_{sq})$  are respective stator current, magnetizing current, and stator voltage in dq coordinate;  $\omega_s$ ,  $\omega$ ,  $z_p$ ,  $J_T$ ,  $M_s$  are synchronous speed, rotor speed, pair of poles, total reduced inertia, and reduced moment to the rotor respectively;  $T_s = \frac{L_s}{R_s}$ ,  $T_r = \frac{L_r}{R_r}$ ,  $\sigma = 1 - \frac{L_m^2}{L_s L_r}$ ,  $a = \frac{1}{\sigma L_s}$ ,  $b = \frac{1}{\sigma T_s}$ ,  $c = \frac{1 - \sigma}{\sigma T_r}$ ,  $d = b + c$ ; and  $R_s$ ,  $L_s$ ,  $R_r$ ,  $L_r$  are respective stator resistance, stator inductance, rotor resistance, rotor inductance.

**V-belt, sheaves, and gear reducer.** Power is typically transmitted to the gearbox from the motor through V-belt and sheaves as shown in Fig.1.7. Since, all points on the

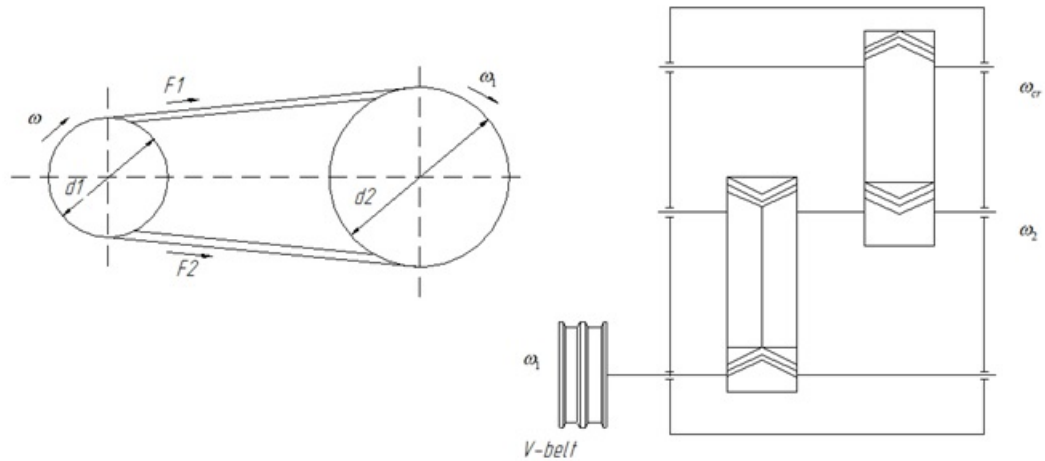


Fig. 1.7 — V-belt, sheaves, and gear box

belt are moving at same velocity, the following relation holds:

$$\omega_1 = \frac{d_1}{z_p d_2} \omega, \quad (1.4)$$

where:  $\omega_1$  is the angular speed at the input of the gear reducer.

Let the gear transformation ratio at the reducer be  $z$ , then the relation between crank speed ( $\omega_{cr}$ ) and rotor speed ( $\omega$ ) can be given by:

$$\omega_{cr} = \frac{\omega_1}{z} = \frac{1}{z} \frac{d_1}{z_p d_2} \omega, \quad (1.5)$$

Now, the overall transformation ratio ( $u_r$ ) of the belt-gear reducer system can be represented by:

$$u_r = \frac{z d_2}{d_1}. \quad (1.6)$$

**Pumping Unit.** The motion law of the polished rod is deduced from the characteristics of the pumping unit which is determined by angular displacement of the crank as given by:

$$\varphi_{cr} = \frac{1}{z_p u_r} \int \omega dt. \quad (1.7)$$

The kinematics of the pumping unit can be expressed referring to Fig.1.8. Let,  $AB = r$ ,  $BC = k$ ,  $CD = l_1$ ,  $DE = l_2$ ,  $OD = n_y$  and  $OA = m_x$ . Then, using the expressions

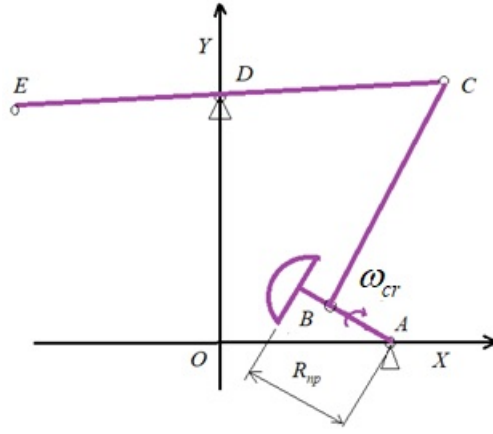


Fig. 1.8 — Schematic diagram of sucker rod pump

presented in Table 2, the coordinate position of points A, B, C, D, and E can be determined at any time where:

$$\begin{aligned}\alpha &= 4((n_y - y_B)^2 + x_B^2), \\ \alpha_1 &= x_B^2 - k^2 + l_1^2 - n_y^2 + y_B^2, \\ \beta &= 4(\alpha_1(n_y - y_B) - 2x_B^2 n_y), \\ \gamma &= \alpha_1^2 - (2x_B l_1)^2 + (2x_B n_y)^2.\end{aligned}$$

Table 2 — Coordinate position of main points

Coordinate point	x	y
A	$m_x$	0
B	$x_B = m_x + r \cos \varphi_{cr}$	$y_B = r \sin \varphi_{cr}$
C	$x_C = \sqrt{l_1^2 - (y_C - n_y)^2}$	$y_C = \frac{-\beta \pm \sqrt{\beta^2 - 4\alpha\gamma}}{2\alpha}$
D	0	$n_y$
E	$x_E = -x_C \frac{l_2}{l_1}$	$y_E = n_y - (y_C - n_y) \frac{l_2}{l_1}$

The angle subtended by segment CD with respect to the horizontal can be given by:

$$aC = \tan^{-1}\left(\frac{y_C - n_y}{x_C}\right). \quad (1.8)$$

Then, the angular velocity of point E is expressed by:

$$\omega_E = -\frac{\Delta aC}{\Delta t}, \quad (1.9)$$

where:  $\Delta t$  is the time interval.

In general, the turning effect of different forces acting on a rigid body can be reduced to any of the shafts based on the expression:

$$M_s = \sum_{i=1}^{i=q} M_{si} u_i + \sum_{j=1}^{j=p} F_{sj} \rho_j, \quad (1.10)$$

where:  $q$  and  $p$  are number of external moment and forces applied to the system,

$u_i$  – the transfer ratio of the  $i^{th}$  element with respect to the reduction shaft,

$\rho_j$  – the imaginary lever arm of the  $j^{th}$  element to the reduction shaft,

$M_{si}$  – the external moment of the  $i^{th}$  element,

$F_{sj}$  – the external load of the  $j^{th}$  element.

Similarly, the total moment of inertia is given on the bases of the general expression:

$$J_T = \sum_{i=1}^{i=n} J_i u_i^2 + \sum_{j=1}^{j=k} m_j \rho_j^2, \quad (1.11)$$

where:  $n$  and  $k$  are the number of moment of inertia and masses performing rotational and translational motion,

$J_i$  – the moment of inertia of the  $i^{th}$  element,

$m_j$  – the mass of the  $j^{th}$  element.

If the reduction is assumed with respect to crank shaft, then:

$$u_i = \frac{\omega_i}{\omega_{cr}}, \quad (1.12)$$

$$\rho_j = \frac{v_j}{\omega_{cr}}, \quad (1.13)$$

where:  $v_j$  – the velocity of the center of mass of the  $j^{th}$  mass.

Analyzing the effect of the load on the polished rod is essential for predicting the gear box torque. The moment due to the polished rod load about the saddle point can be given by:

$$M_{spht} = F_{pht} l_2, \quad (1.14)$$

where:  $F_{pht}$  – the polished rod load.

The same moment about the crank shaft can be written:

$$M_{pht} = F_{pht} l_2 \frac{\omega_E}{\omega_{cr}}. \quad (1.15)$$

The torque at the crank shaft due to the polished rod load can be assumed to be the product of the polished rod load and an imaginary lever arm. This imaginary lever arm is known as torque factor and is defined as:

$$TF(\varphi_{cr}) = l_2 \frac{\omega_E}{\omega_{cr}}. \quad (1.16)$$

The moment due to counterweight about the crank can also be expressed as:

$$M_{cb} = m_1 g R_{np} \cos \varphi_{cr}, \quad (1.17)$$

where:  $m_1$  – mass of the counterweight,

$g$  – gravitational acceleration,

$R_{np}$  – distance between center of mass of counterweight and the axis about which the crank rotates.

Finally, the total moment about the crank is:

$$M_c = M_{pht} + M_{cb}. \quad (1.18)$$

The total inertia about the crank due to the beam, horse head, equalizer, bearing and pitman can be calculated by:

$$J_T = \sum_{j=1}^n m_j \left( \frac{v_j u_r}{\omega} \right)^2. \quad (1.19)$$

The inertial moment due to the different masses can also be written as:

$$M_i = \frac{\omega_{cr}^2}{2} \frac{dJ_T(\varphi_{cr})}{d\varphi_{cr}}. \quad (1.20)$$

Therefore, the net moment about the rotor shaft can be given by:

$$M_s = \frac{1}{u_r} (M_c + M_i). \quad (1.21)$$

### 1.4.3 Subsurface Pump Model

The main elements of the subsurface pump assembly are barrel, plunger, standing valve and travelling valve. The subsurface boundary condition is determined from

(1.22), which is based on equilibrium of the plunger and considers the effects of reservoir condition. The load on the plunger is given by:

$$F_{pl} = A_{pl}(P_d - P) + A_r P_d, \quad (1.22)$$

where:  $F_{pl}$  represents load on the plunger,

$A_{pl}$  represents cross-sectional area of the plunger,

$A_r$  represents cross-sectional area of the rod,

$P_d$  represents discharge pressure,

$P$  represents pump pressure.

Since the discharge pressure remains nearly constant for considerable length of time, the variation of load on the plunger is mainly influenced by the pump pressure. Therefore, a clear understanding of the pump operation is vital to describe the subsurface boundary condition. During normal working state, four phases exist in one cycle of pump operation based on the valve state and movement of the plunger. Table 3 presents summary on the relation between plunger displacement, valve state and corresponding phase.  $\Delta P_s$  represents hydraulic loss of standing valve and  $\Delta P_d$  represents hydraulic loss of travelling valve. During faulty working states, the subsurface boundary condition will be different from the boundary conditions of normal working state because the fault may cause change in fluid flow or/and characteristics of the fluid or other mechanical problems.

Table 3 — Relation between plunger displacement, valve state and phase

<b>Stroke</b>	<b>Travelling valve</b>	<b>Standing valve</b>	<b>Pump pressure</b>	<b>Phase</b>
Upstroke	closed	closed	$P_s < P < P_d$	expansion phase
Upstroke	closed	opened	$P_s - \Delta P_s$	pumping phase
Down stroke	closed	closed	$P_s < P < P_d$	compression phase
Down stroke	opened	closed	$P_d - \Delta P_d$	discharging phase

According to the pump working process, the pump pressure belongs to gas polytropic process with mass change [34]. The operation of the valves depend on the value of pump pressure relative to suction pressure for standing valve and relative to discharge pressure for travelling valve. Based on the transient variation rule of liquid pressure in the pump, the rate of liquid pressure in [29] is described by (1.23) and (1.24) for upstroke and down stroke respectively as:

$$\frac{dP}{dt} = \begin{cases} \frac{(v_{pl}A_{pl} - \frac{\pi D_{pl}\delta^3}{12\mu L_p}(P_d - P))P_d}{V_{og}(-\frac{1}{n})(\frac{P}{P_d})^{-\frac{1}{n}-1}}, & \text{if } P > P_s \\ 0, & \text{if } P = P_s \end{cases} \quad (1.23)$$

$$\frac{dP}{dt} = \begin{cases} \frac{(v_{pl}A_{pl} - \frac{\pi D_{pl}\delta^3}{12\mu L_p}(P_d - P))P_s}{V_g(-\frac{1}{n})(\frac{P}{P_s})^{-\frac{1}{n}-1}}, & \text{if } P < P_d \\ 0, & \text{if } P = P_d \end{cases} \quad (1.24)$$

where:  $D_{pl}$  – diameter of the plunger,

$v_{pl}$  – the velocity of the plunger,

$V_{og}$  – the volume of residual gas of the clearance volume,

$P$  – pump pressure,

$\delta$  – the gap between the pump plunger and barrel,

$\mu$  – kinematic viscosity of liquid,

$n$  – power law coefficient,

$V_g$  – the volume of free gas,

$P_s$  – suction pressure.

#### 1.4.4 Reservoir Model

Information about well's inflow performance relationship plays vital role in examining accurately the performance of sucker rod pump. Several factors such as reservoir properties (rock permeability, pay thickness, etc), fluid properties (viscosity, density, etc), and well completion effects (perforation, well damage) affect the fluid

inflow into the well [3]. However, Darcy's law is universally used for all the quantitative analysis about oil reservoirs. Mathematically, Darcy's law can be given by:

$$\frac{q}{A} = -\frac{k}{\mu} \frac{dp}{dl}, \quad (1.25)$$

where:  $q$  – liquid rate,

$A$  – cross-sectional area,

$k$  – permeability,

$dp/dl$  – pressure gradient.

For considerable length of time, several factors such as effective permeability, pay thickness, liquid viscosity, drainage radius, reservoir pressure can be assumed constant. This assumption results the simplest expression given by:

$$q = PI(P_{rev} - P_{wf}), \quad (1.26)$$

Where:  $PI$  – productivity index,

$P_{rev}$  – reservoir pressure,

$P_{wf}$  – bottom hole pressure.

The expression (1.26) indicates that the inflow performance relationship is a linear function of the bottom hole pressure.

In case, if the pressure in the vicinity of well bore can be below the bubble point pressure, free gas can be liberated. This effect reduces the liquid rate compared to single phase conditions. Such cases are better described by Vogel's inflow performance relationship [35] as given by the expression:

$$\frac{q}{q_{max}} = 1 - 0.2 \frac{P_{wf}}{P_{rev}} - 0.8 \left( \frac{P_{wf}}{P_{rev}} \right)^2, \quad (1.27)$$

where:  $q_{max}$  is the maximum liquid rate.

## 1.5 Simulation Results

The models of induction motor, pumping unit, sucker rod string, subsurface pump and reservoir model are integrated. The integrated simulation model can be described

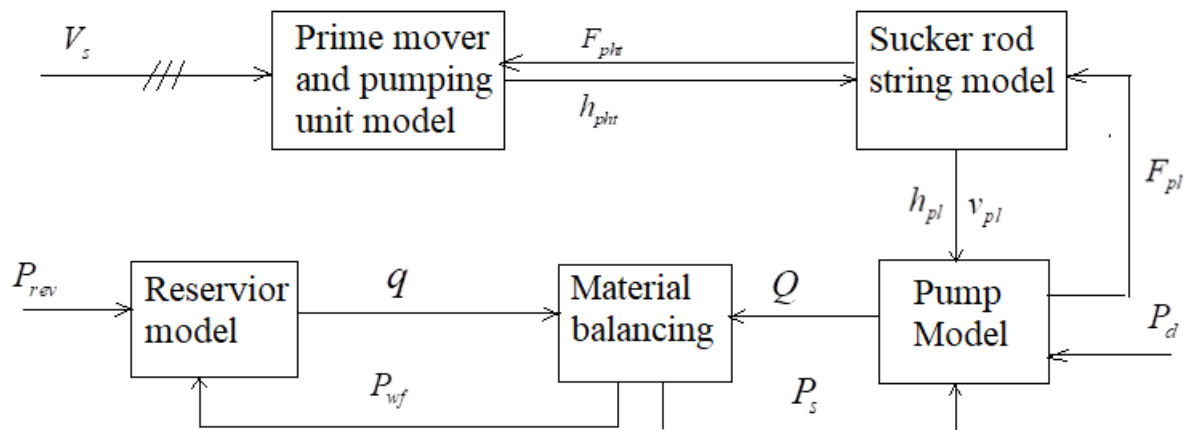


Fig. 1.9 — Sucker rod pump simulation model

$V_s$  – supply voltage;  $F_{pht}$ -polished rod load;  $h_{pht}$ - polished rod displacement;  $h_{pl}$ - plunger displacement;  $v_{pl}$  - plunger velocity;  $F_{pl}$  - load on plunger;  $P_{rev}$ - reservoir pressure;  $P_{wf}$  - bottomhole pressure;  $P_s$  -suction pressure;  $P_d$  - discharge pressure;  $q$  - rate of liquid flow

by the block diagram representation shown in Fig.1.9. The sucker rod string block represents the longitudinal vibration model of sucker rod string. It interacts with the pumping unit model and subsurface pump model to obtain the required boundary conditions. It computes the polished rod load and kinematic parameters of plunger for given surface and subsurface boundary conditions. The prime mover and pumping unit model block simulate the energy conversion process and the kinematics of pumping unit by interacting with the sucker rod string block and provides surface boundary conditions to the sucker rod string model. The pump model simulates the pressure variation in the pump, which is the key parameter in determining the subsurface boundary condition. It interacts with the reservoir model by considering the material balancing. The reservoir model simulates the well's inflow performance relationship.

A pumping unit with a given geometry produces a unique kinematic characteristic on its elements when driven. Since, the inertial torque and the overall gearbox torque are dependent on the pumping unit's kinematic parameters, it is essential to analyze the pumping unit's kinematic characteristics. In this dissertation work, all the results are for the case when the pumping unit is driven clockwise (motoring mode in III quadrant of the mechanical characteristics). Fig. 1.10 shows the polished rod's displacement, velocity and acceleration as well as its normalized load as a function of time for normal

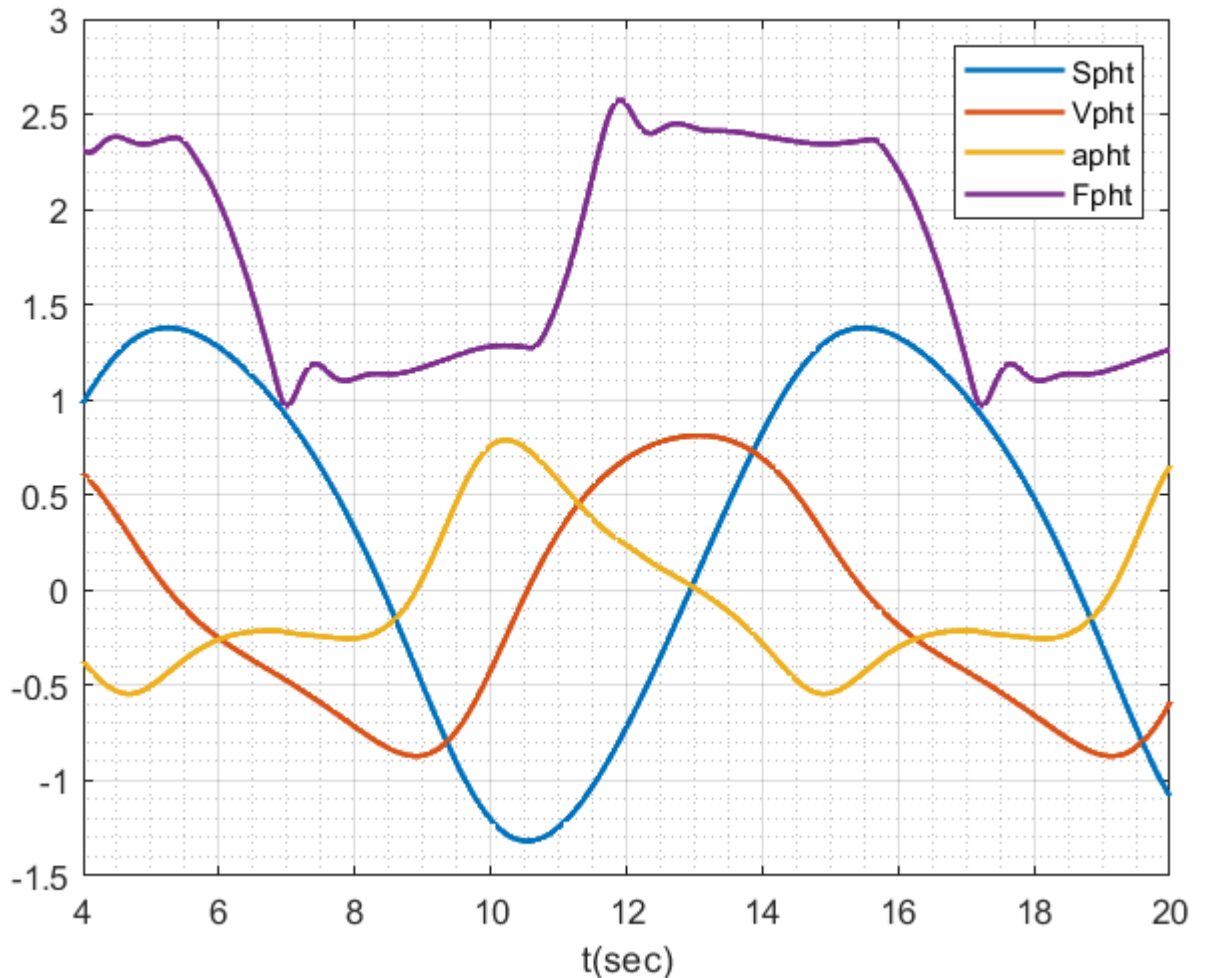


Fig. 1.10 — Polished rod displacement, velocity, acceleration and load

working state. The polished rod displacement changes uniformly like sine function. The polished rod velocity also varies somehow like sine function leading to the curve of the polished rod displacement. Its value is positive during the upstroke while negative during the down stroke. On the other hand, the polished rod acceleration varies in irregular manner. The maximum acceleration occurs at the start of the upstroke while the minimum acceleration occurs at the start of down stroke. A highly variable curve of the polished rod load is an indication of the difference in loading during the upstroke and down stroke. The oscillations at the beginning of each stroke show effects of dynamic loads. The torque factor is the characteristic parameter for a given pumping unit, which is useful in the calculation of net gearbox torque. Fig. 1.11 shows the variation of torque factor with time. Selection of proper pumping unit is based on its kinematic behavior. In ideal case the kinematic behavior of the pumping unit should have a long

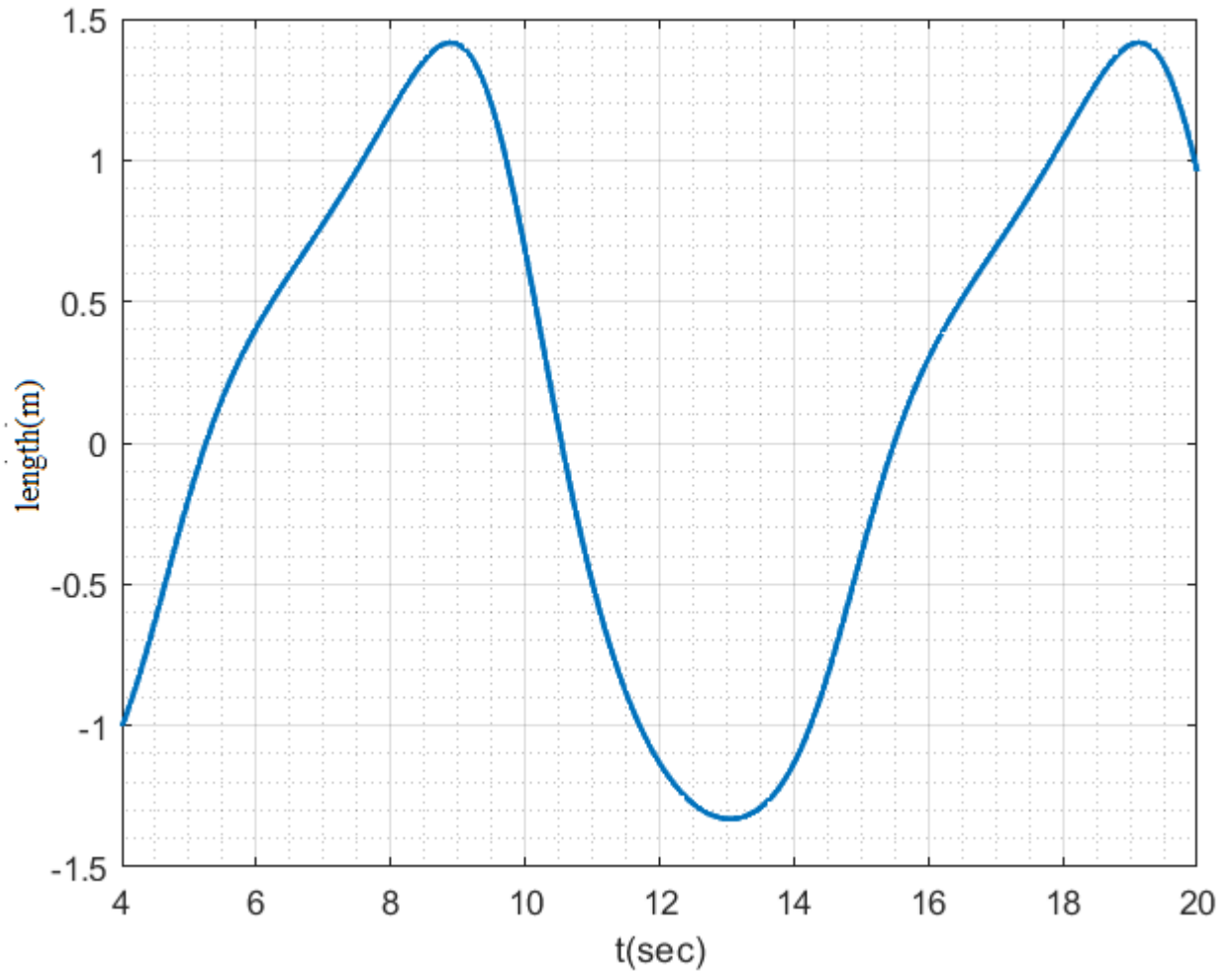


Fig. 1.11 — Torque factor

and slow upstroke, faster and short downstroke, low torque factors on the upstroke, reduced acceleration at the start of the upstroke.

Due to the elastic property of the sucker rod string, the polished rod displacement and the plunger displacement do not coincide in magnitude and time. Fig. 1.12 shows a comparison of polished rod displacement and plunger displacement. As it can be clearly seen, the curve of the polished rod displacement varies uniformly. On the other hand, the plunger does not start to move at the start of the upstroke. Similarly, the plunger remains stationary at the beginning of down stroke. Moreover, it can be seen that the stroke length of the plunger is less than the stroke length of the polished rod.

The net torque loading on the gearbox is the resultant of the torque due to polished rod load, torque due to counterweight and inertial torques. Fig. 1.13 shows torque due to counterweight, polished rod load, and inertia all reduced to the rotor shaft and the net

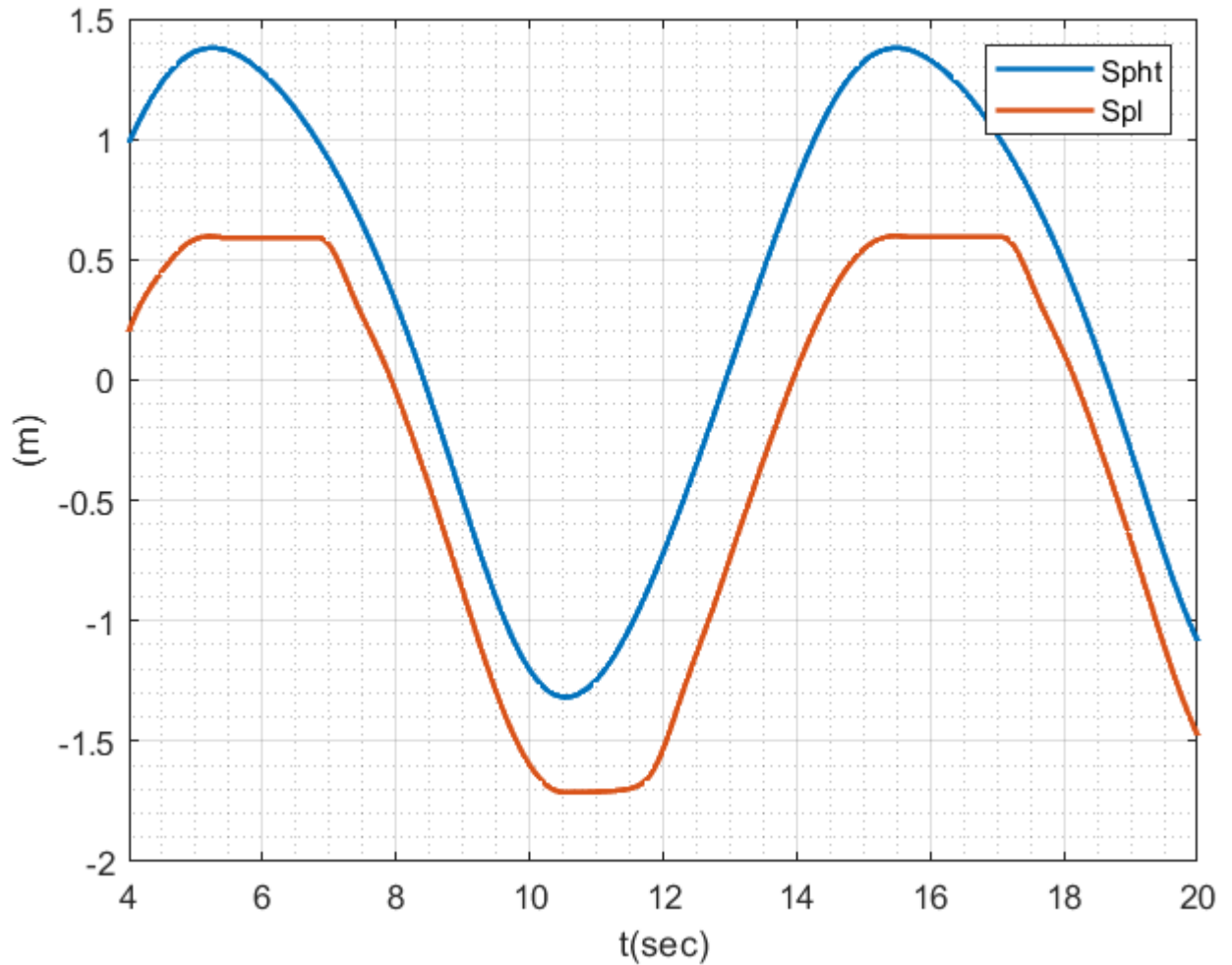


Fig. 1.12 — Polished rod displacement, plunger displacement

motor torque. Inertial torque is very small. Thus, it can be said that the motor develops a torque mainly to resist the resultant of the torque due to polished rod load and counterweight. The torque due to polished rod load and counterweight are nearly out of phase but do not cancel each other. Due to this reason, the net motor torque presents a double-hump characteristics and as a response the rotor speed shows variations as shown in Fig. 1.14.

The dynamometer card, which shows the relation between polished rod displacement and load, is the primary tool in the analysis and diagnosis of the sucker rod pump. It indicates the effects of static and dynamic loads acting on the polished rod. Static loads are caused by the weight of the fluid column, buoyant force and weight of the sucker rod string whereas dynamic loads include inertial and vibrational loads. Moreover, the effects of string deformations can also be seen in the dynamometer

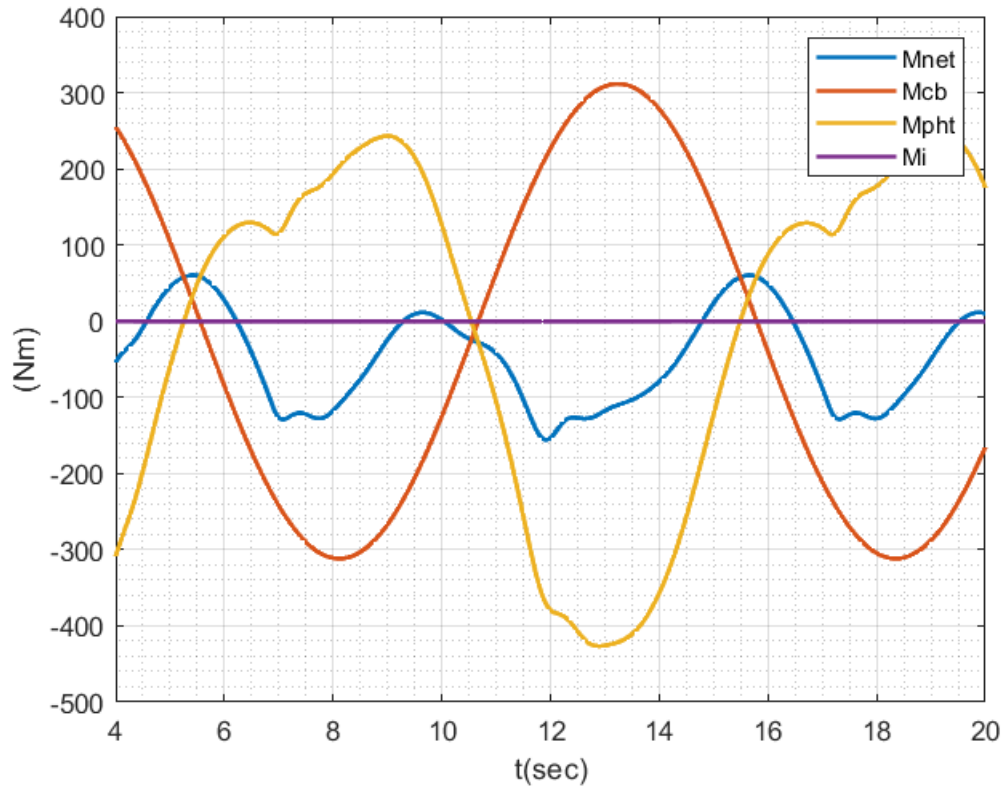


Fig. 1.13 — Gearbox torque components reduced to rotor shaft

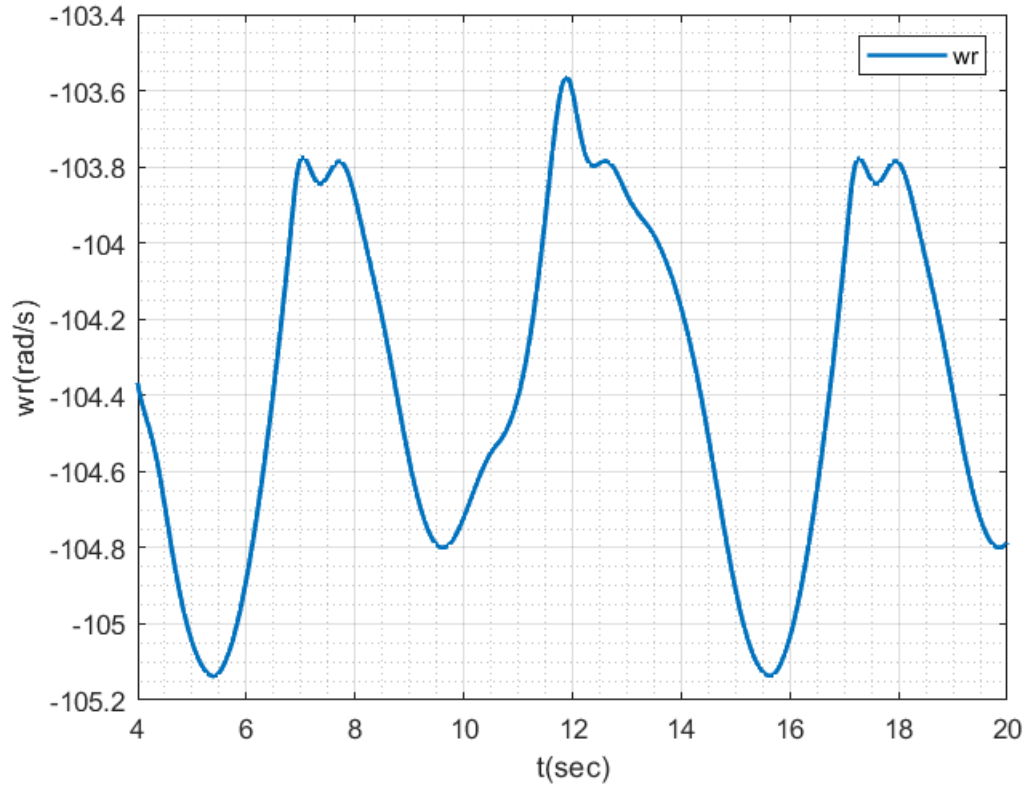


Fig. 1.14 — Rotor speed

card. Fig. 1.15 shows the dynamometer card for normal working state. A higher load along with short duration oscillations at the beginning of the upstroke and a lower load along with short duration oscillation at the beginning of the down stroke indicate the effect of dynamic loads. The dynamometer card is slightly rotated to the right due to the effect of deformation.

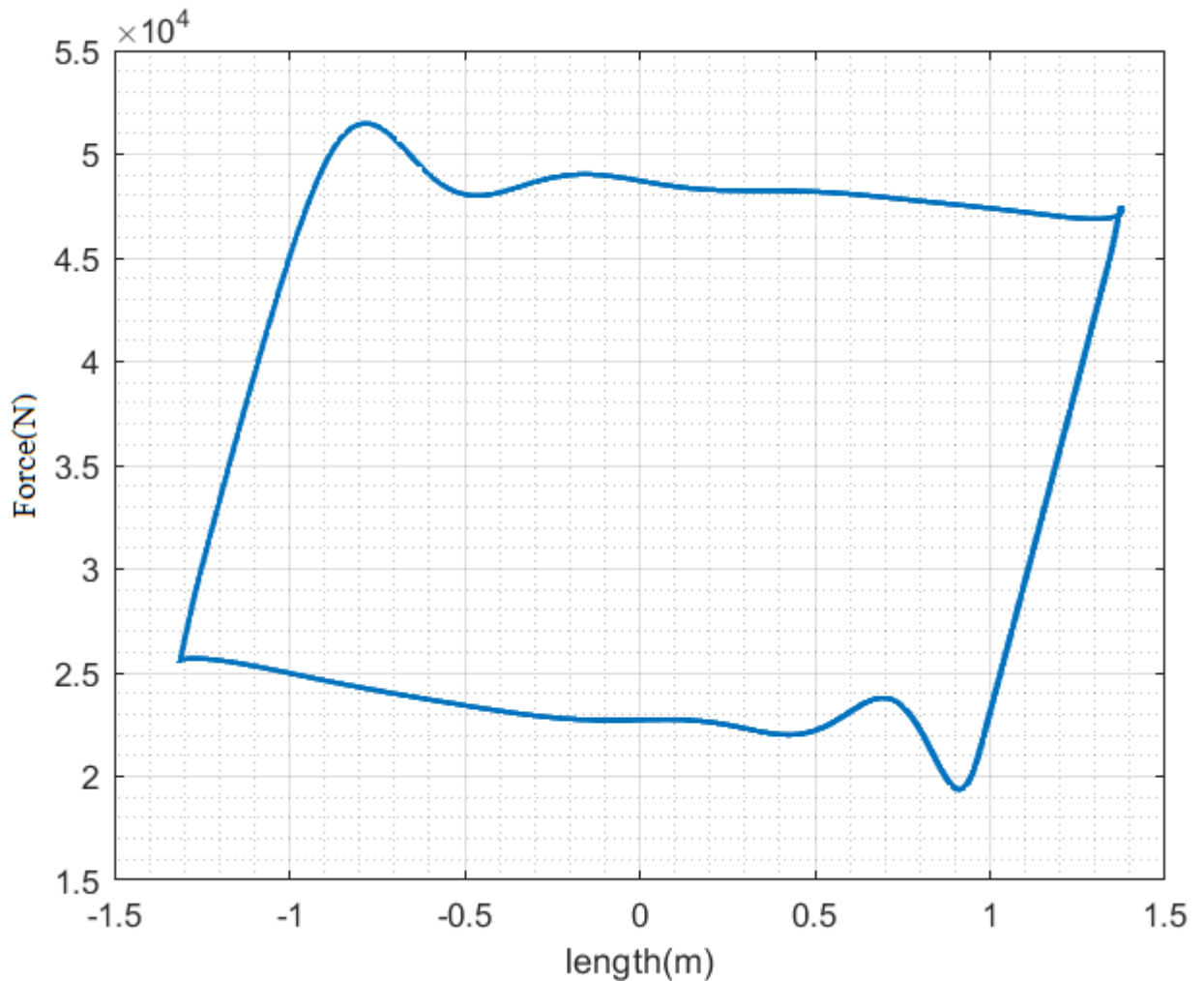


Fig. 1.15 — Dynamometer card

The effect of change in dynamic height on input power and power loss are shown in Fig. 1.16 and Fig. 1.17 respectively. It can be seen that for deeper dynamic height, the input power requirement and power losses are more than for less deeper dynamic heights during the upstroke since the load on the plunger increases with increase in dynamic height.

It is known that different combination of size and position of the counterweight, produce different moment. Consequently, the energy consumption of the prime mover

will be different. Fig. 1.18 shows the energy consumption for duration in upstroke, down stroke and total energy consumption for one cycle of pump operation. As the distance between the center of mass of the counterweight and axis of crank shaft decreases, the energy consumption for upstroke increases whereas for the down stroke decreases. Fig. 1.19 shows the magnified total energy consumption. It can be seen that the optimal radius is about 1.25 meters.

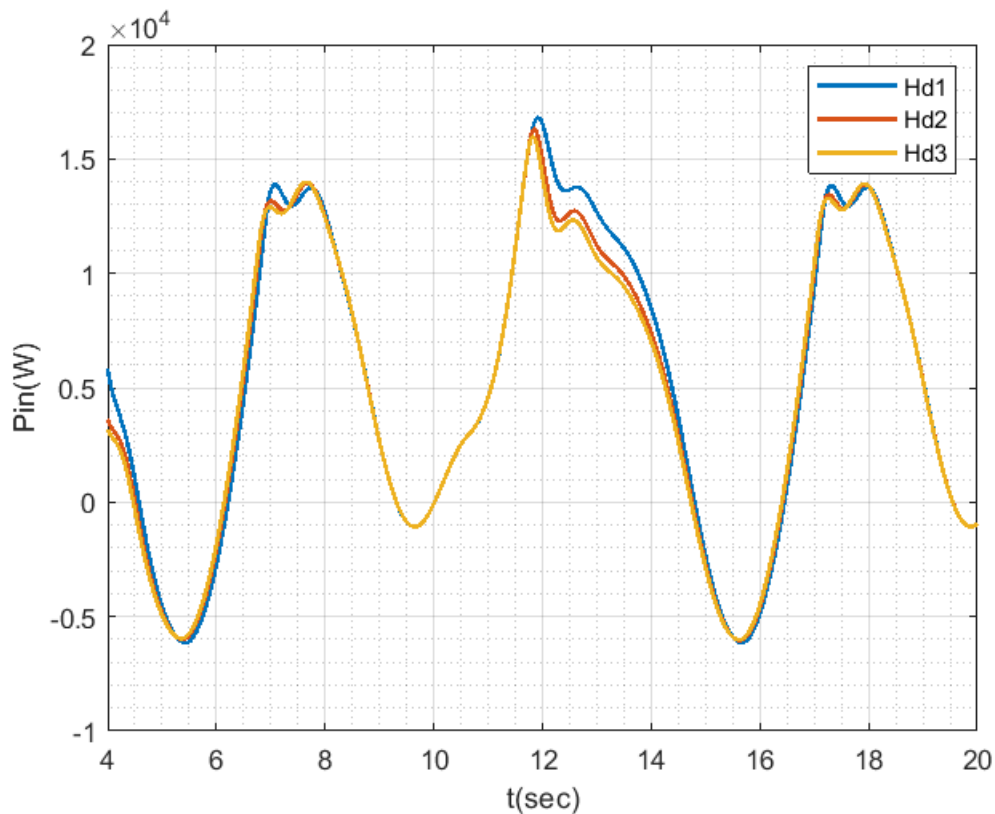


Fig. 1.16 — Input power Hd1=1124m, Hd2=1070m, Hd3=1040m

## 1.6 Summary

The sucker rod pump system consists of complex subsystems. Therefore, certain assumptions are adapted when modeling the different components. The models of the different components of sucker rod pump are integrated to simulate the sucker rod pump operation. The pumping unit's kinematic parameters, different components of gearbox torque, and dynamometer card are presented as results of simulation from the

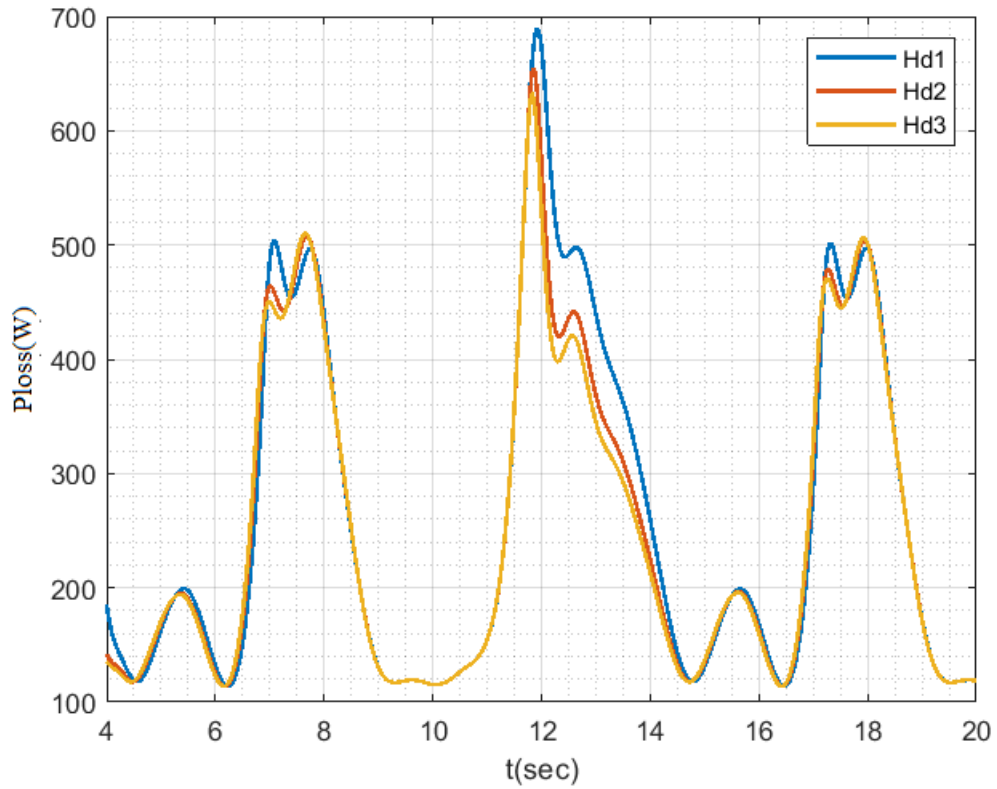


Fig. 1.17 — Power loss Hd1=1124m, Hd2=1000m, Hd3=950m

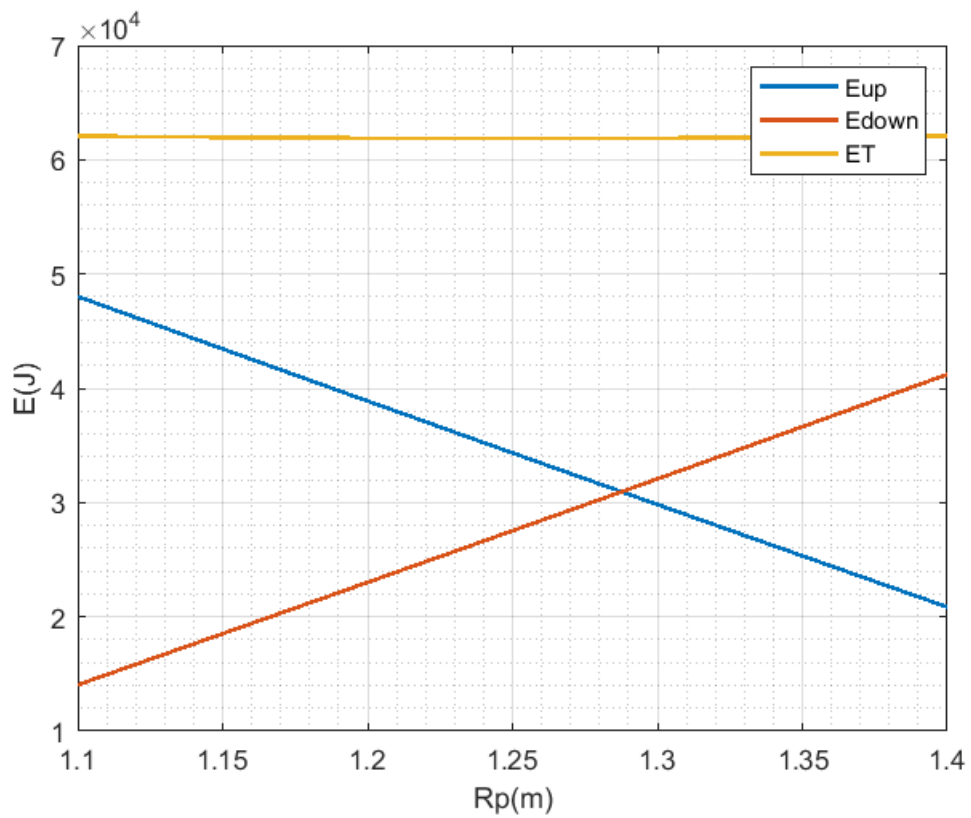


Fig. 1.18 — Effect of radius of counterbalance

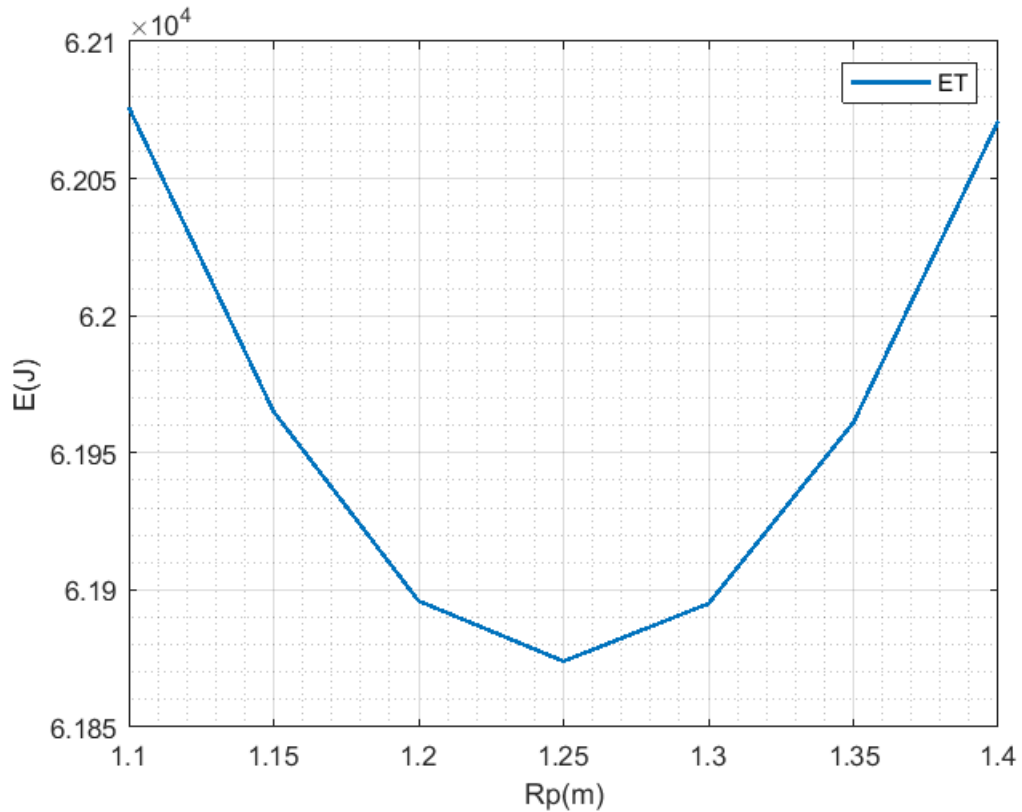


Fig. 1.19 — Effect of radius of counterbalance (magnified)

developed integrated simulation model for normal working state. The results present common characteristics of sucker rod pump. The integrated simulation model can also be set to simulate different sucker rod pump faulty working states. Therefore, it can be used for building a training set. Moreover, the developed model can help to deepen research conducted in design and analysis. For example, research related to the optimal counterbalance adjustment and optimal energy efficiency operation.

## Chapter 2. Sucker Rod Pump Working State Diagnosis

### 2.1 Introduction

The need to develop monitoring and fault diagnosis system is becoming apparent in order to increase the economic benefits obtained from sucker rod pump installations. Operation in faulty working state may lead to equipment damage and production loss. An effective monitoring and diagnosis technology can help to monitor and control the operation of sucker rod pump thereby ensuring safe and optimal production efficiency operation.

The information about sucker rod pump working state is embodied in the polished rod load and motor power curve if driven by electric motor. The information contained in the polished rod load is interpreted with the help of dynamometer card. Each working state is identified by distinctive characteristic shape of dynamometer card, which is easily interpreted by visual inspection but is inefficient. In contrast, the motor power curve cannot be easily interpreted by visual inspection. In recent researches, automatic fault diagnosis system based on advanced methods have been proposed in order to exploit the promising potential of motor power curve. However, the advanced methods require large number of training data, which can be hardly obtained. In the present chapter, the required labeled samples (motor power curve) for training are generated using the developed dynamic simulator for sucker rod pump by considering the possible scenarios in the subsurface. The samples are represented uniquely by a feature vector, which is constructed based on valve working points and energy dissipation. The samples generated by the model are utilized by SVM to produce classifying function.

## 2.2 Sucker Rod Pump Operation Analysis

In the working process of subsurface pump, many coupled variables are involved. As a result, its analysis is complex. In theoretical normal working state, as shown in Fig. 2.1 expansion, pumping, compression and discharging phases occur one after another in one cycle of pump operation. The effect of the four phases can be described by the theoretical dynamometer card as shown in Fig. 2.1 (top). Point  $A'$  corresponds to bottom dead center whereas point  $C'$  corresponds to top dead center. The travelling valve closing point coincides with bottom dead center and the standing valve closing point coincides with top dead center. Although the opening of both valves depends on the amount of free gas in the pump, the assumption for the theoretical normal working state is that the standing valve opens at point  $B'$  and the travelling valve opens at point  $D'$ .

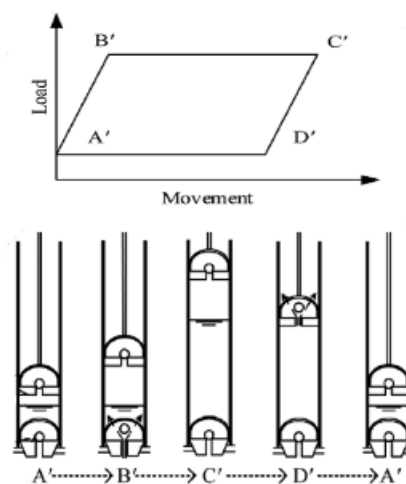


Fig. 2.1 — Four phases of pump operation

Fig. 2.2 shows normalized curves of pump pressure, motor power curve, polished rod displacement, velocity and load for the normal working state. It is known that when the travelling valve is open, the pump pressure nearly equals the discharge pressure. Conversely, when the standing valve is open, the pump pressure nearly equals the suction pressure. The location of valve working points is clear from the curve of pump pressure. This leads to the conclusion that the valve closing point corresponds to the valleys on motor power curve and the valve opening points correspond to the peaks on motor power curve. In addition, the minimum power corresponds to end of upstroke.

Thus, the location of peaks and valleys on the motor power curve are convenient for the analysis of the sucker rod pump working process.

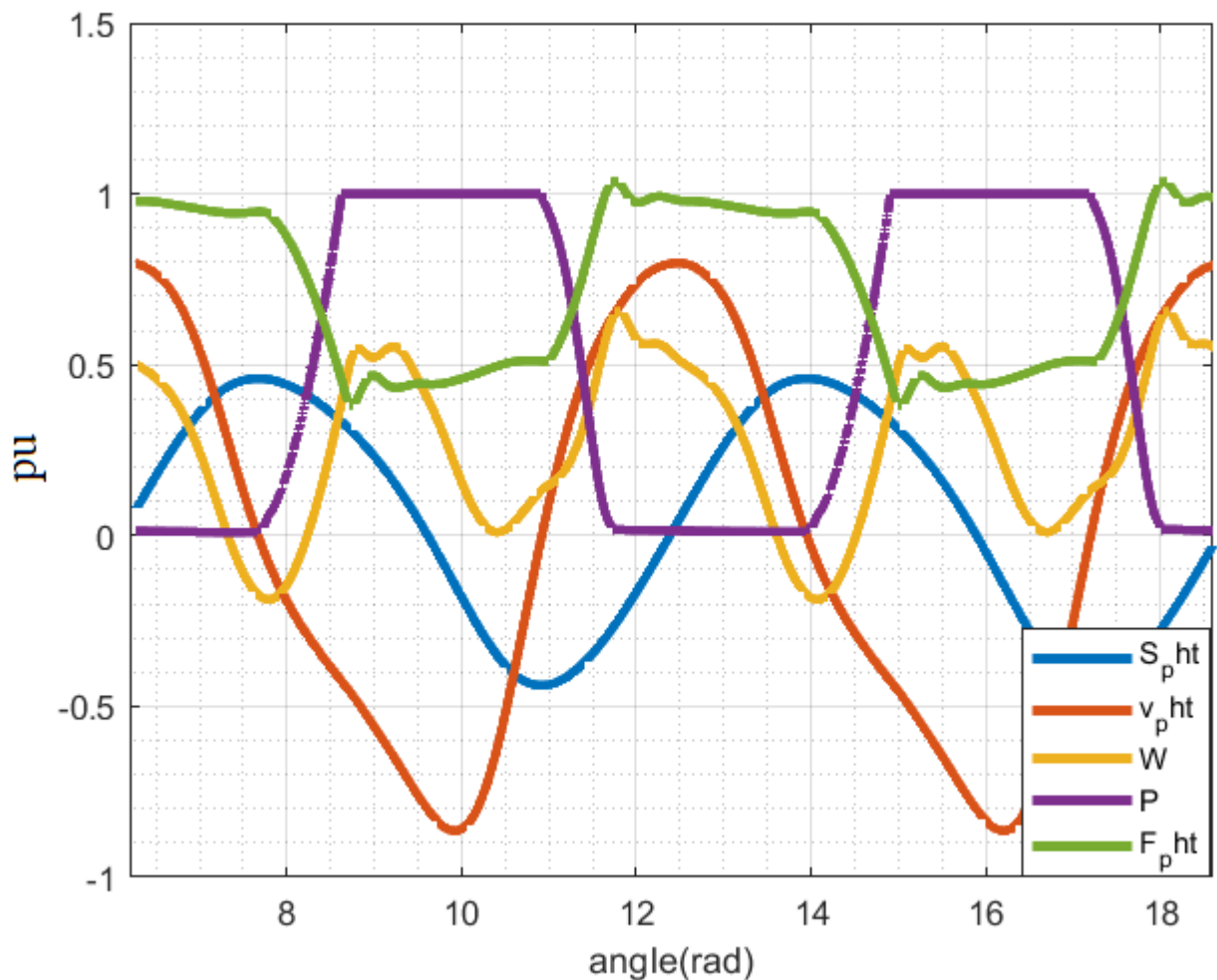


Fig. 2.2 — Mechanism analysis

### 2.3 Sucker Rod Pump Working States and Characteristics

In the study of sucker rod pump, the behavior of sucker rod string is found to be the most influential part. The sucker rod string responds to all changes in the subsurface conditions, where a sophisticated processes is involved. Faults in the underground change the equilibrium points of the state equations that describe the subsurface pump. As a result load on the plunger and polished rod are affected. The effects of a particular

fault are distinguished by the shape of the dynamometer card. In literature, there are more than 20 working state but, in this thesis, the flowing working states are considered.

**Normal Working State.** If there is sufficient inflow from the well at the given pumping speed and the fluid pumped to the pump is incompressible (the amount of free gas is small), the pump can be filled completely as shown in Fig. 2.3a. Under this condition, the travelling valve immediately opens at the start of the down stroke and the standing valve immediately opens at the start of the upstroke.

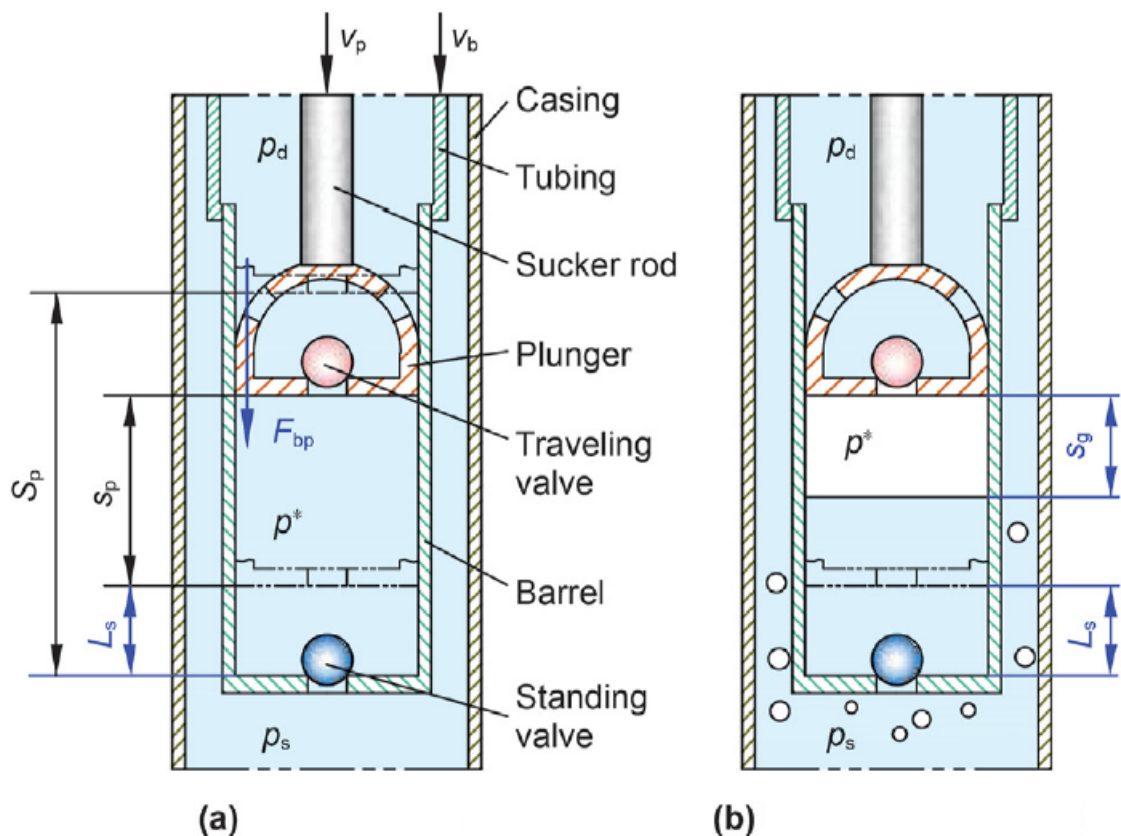


Fig. 2.3 — Subsurface pump conditions [36]: a, normal working state b, gas affected

**Gas Affected.** If the fluid entering the pump is composite, the pump is partially filled. At the end of the upstroke, the length of the free gas becomes larger as indicated in Fig. 2.3b. This means the parameter  $V_g$  in (1.24) becomes larger. Under this condition, during the down stroke, the gas is compressed until the pressure in the pump equals the discharge pressure, where the travelling valve opens. This effect is characterized on the dynamometer card by a slight absence bottom right corner as compared to the normal working state. If the gas content is high such that no valve can open, the state is called gas lock.

**Insufficient Liquid Supply.** Insufficient liquid supply occurs if the pumping speed is faster as compared to the inflow performance from the well. Under this condition, the pump is partially filled and at the end of the upstroke the length of the gas is like as indicated for gas affected. However, the pump pressure at the beginning of down stroke is lower as compared to gas affected. Thus, the travelling valve opens when the plunger is very close to the liquid level in the barrel and the impact of the plunger on the liquid may induce high compression loads in the string [3]. A dynamometer card which lacks the right bottom corner characterizes this effect.

**Travelling Valve Leakage.** Due to some damages after wearing out or dirty cover, the travelling valve cannot be perfectly closed. This causes the liquid to leak through the gap created and increases the pump pressure. A parabolic curve at the left upper portion of the dynamometer card shows the effect of travelling valve leakage.

**Plunger Hitting Top or Bottom Dead Center.** Because of improper spacing of the pump or some deposits in the pump barrel, the plunger could hit top or bottom dead center. During the impact period, the load on the polished rod increases when the plunger hits top dead center but decreases when the plunger hits bottom dead center. During the other durations, the working process is like the normal working state. This effect is seen with a bulge on the dynamometer card at the lower left corner when plunger hits bottom dead center and at the upper right corner when the plunger hits top dead center.

## **2.4 Review on Sucker Rod Pump Monitoring and Diagnosis**

### **2.4.1 Monitoring Sucker Rod Pump Operating Condition**

The sucker rod pump consists of surface and subsurface components. The subsurface pump operates thousands of meters deep in the underground. Most of failures of sucker rod pump are attributed to subsurface pump, sucker rod string and tubing.

Failure in these parts is defined as catastrophic because repairs of such equipment is extremely expensive [37]. Therefore, for satisfactory oil well operation of sucker rod pumps, it is important to single out the problems, record real root cause of each failure, put into effect the appropriate change, and keep future failures from occurring.

Information on the subsurface conditions can be monitored or predicted from direct measurements of well's operational parameters namely well head and annulus pressure, fluid temperature, dynamic fluid level, and mass flow rate. The elastic nature of the sucker rod string also offers another alternative for monitoring or predicting subsurface conditions. Through the reciprocating movement of the sucker rod string, mechanical energy is provided to the fluid and as a response the sucker rod string is exposed to different forces. These effects are transmitted up to the terminals of the prime mover. Hence, these effects are reflected on the polished rod load as well as on the input power of the prime mover.

Fig. 2.4 helps to realize the physical meaning of the well's operational parameters. The changes in well's operational parameters can be monitored by using underground sensors and acoustic measurements. An example of field wide optical sensing deployment has been described in [38] to meet reservoir monitoring objectives. The information obtained from these measurements can be utilized for material balance calculation [39] and by a control system which improves production performance and minimizes maintenance costs[40; 41]. Moreover, the use of thermogram to record the temperature distribution along the wellbore provides several useful information [42]. For example, through such records it is possible to estimate the increase in temperature with increase in depth and inflow profiles, analyze the series of changes taking place in the formation (during thermal impact, pumping cold water), and reserve recovery during watering, keep an eye on the technical condition of the wells and the operation of subsurface equipment. However, the reliability of sensors placed in the subsurface to measure the well's operational parameters is not guaranteed and there is difficulty in associating the parameters with the faulty working states.

The information about dynamic property of fluids, gas, subsurface and surface equipment is present on acoustic records [43]. Conventional or automated devices can

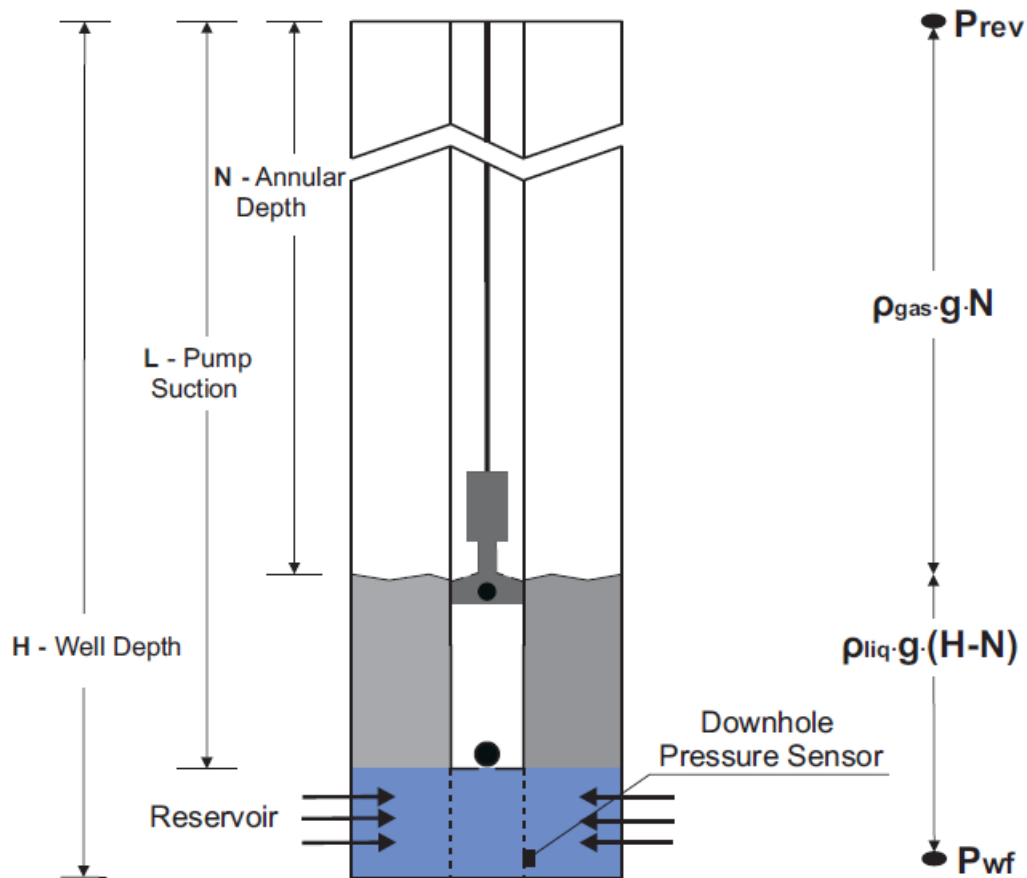


Fig. 2.4 — Production well

be installed at the well head of the sucker rod pump to collect acoustic data. However, advanced processing techniques are required to extract the useful information. Acoustics is a convenient and accurate method for measuring the liquid level in the annulus [15]. The application of acoustic analysis can be extended to sucker rod pump working state diagnosis because there is a possibility to correlate sound feature to dynamometer card [43]. Because surface installed special devices are more reliable than those in the underground, monitoring through acoustic measurement installed at the surface has better advantages than underground sensor-based monitoring. However, noise in the vicinity of wellhead can also be recorded.

The dynamic effects of different forces exerted on the subsurface components can also be observed on curve of the polished rod load. The dynamometer card is the common way to analyze these effects. It can be produced from synchronized measurement of polished rod load and displacement. Different types of sensors are available for measuring the polished rod load and displacement. However, during

selection higher consideration is given to their durability and accuracy. Moreover, polished rod load and displacement can be obtained from motor measurements.

### 2.4.2 Sensor Based Measurements

**Measurement of Load.** Polished rod load can be obtained by installing strain gauge in the beam, load cell on the carrier bar beneath the polished rod clamp or can be inferred from motor measurements [44].

Beam mounted strain gauge measures the changes in the tension of the walking beam, which is assumed to be equivalent to polished rod load. However, this is less accurate because the polished rod load and pitman load have parallel load in addition to the load which causes turning moment. Another drawback of this method is that temperature influences the measured strain.

Load cell directly measures the polished rod load. To compensate the effects of temperature, load cell employs full bridge strain gauge configuration. However, slight imbalance occurs due to manufacturing tolerances.

The polished rod load can be calculated if the net gearbox torque, crank speed, parameters of the pumping unit are known. The net gearbox torque and crank speed can be obtained from motor measurements assuming the overall transmission ratio of V-belt and gear reducer is known.

Table 4 gives comparative analysis of the three methods of polished rod measurement. The most needed advantages can be obtained by inferring the polished rod load from motor measurements.

**Position measurement.** The position of the polished rod can be measured by using position switch, inclinometer or hall-effect transducer [44].

In the simplest method, the rod pump controller, which calculates the polished rod displacement, assumes that the displacement of the polished rod is sinusoidal and predicts the polished rod displacement using a reference signal generated from position

Table 4 — Comparison of methods used for obtaining polished rod load

<b>Sensor type</b>	<b>Ease of installation</b>	<b>Reliability</b>	<b>Accuracy</b>
Beam mounted strain gauge	easy	high	less
Load cell	difficult	less	high
Motor measurements	easy	high	high

switch, which is made from stationary stainless steel wand and magnet attached to the crank. The position switch generates a reference signal when stainless steel wand, and a magnet attached to the crank are face to face. Since the actual displacement of polished rod is not sinusoidal, the measured displacement is not accurate.

In another method, the crank and rotor revolutions are measured using hall-effect transducers and fed to rod pump controller. The transducer which measures the crank revolutions serves as a reference signal while each rotor revolution indicates incremental change in crank angle. In this method the calculation of polished rod displacement is based on pumping unit's geometry but requires proper phase adjustment. This method has an improved accuracy compared to the position switch method.

The polished rod displacement can also be measured directly using an inclinometer. Inclinometer utilizes accelerometer to measure the angle of the beam as it varies throughout the stroke [44].

Table 5 gives comparative analysis of different polished rod displacement measurement methods. Each sensor type has its own advantages and disadvantages. This demands another alternative.

Table 5 — Comparison of polished rod displacement measurement methods

Sensor type	Ease of installation	Accuracy	Requirement
Position switch	simple	low	calibration
Hall effect transducer	simple	medium	proper configuration and Phase adjustment, calibration
Inclinometer	difficult	high	careful installation

### 2.4.3 Inferring Polished Rod Load and Displacement from Estimated Rotor Speed and Torque

Operation analysis or diagnosis based on motor measurement offers more advantages. It can eliminate the use of sensors and improves the reliability of a diagnostic system. In addition, monitoring based on motor measurements is more informative because it can give complete information about operation of the subsurface equipment and the state of the ground equipment. For example, rotor defects, static and dynamic eccentricities and bearing defects can be identified from spectral density of the power curve [42].

Polished rod load could also be inferred from motor torque and speed measurements provided that the dimensions of the pumping unit and overall transmission ratio of the surface transmission system are known. In [45], mathematical bases have been developed to infer polished rod load from induction motor torque using kinematic analysis. This article uses the rotor slot harmonics, which are present in the line current of an induction motor, to obtain slip and then the shaft torque. Modern frequency converters provide estimates of motor parameters. In [46], torque and rotor speed estimates from the frequency converter and the identified correspondence between rotor angle and polished rod displacement as well as no load torque are used to infer the polished rod load.

The above discussion aims to obtain dynamometer card and through it sucker rod pump analysis and diagnosis can be made. However, the effect of load variations along

their corresponding times is contained on the motor power curve. The motor power curve is periodic, with period equal to the period of one pumping cycle. Thus, in place of dynamometer card, the motor power curve can be used as source of information to diagnostic system. In some literatures, the motor power curve is also named as wattmeterogram. Wattmetering is the process of obtaining a wattmeterogram showing the relationship between the power consumed by the pump motor and the angle of rotation of the crankshaft, or the dependence of the power consumed by the installation from time [42]. Some conditions of sucker rod pump can be diagnosed visually from the motor power curve. For example, by visual inspection of the consecutive peaks on the motor power curve, coefficient of unbalance can be determined. Moreover, signs of break in sucker rod string are indicated by an increase in the peak on the motor power curve during the down stroke and no half-period of power increase during the upstroke. Similarly, a leaky travelling valve is indicated on the motor power curve by significant reduction in the power consumed by the prime mover during the upstroke. From the spectrum of motor power curve, it is possible to diagnose defects in the gearbox gearing, bearings, pumping unit elements, low oil level [47]. However, for better utilization the motor power curve must be processed to extract the useful features.

## **2.5 Computer Aided Diagnostic System**

The traditional diagnosis method of sucker rod pump has been found inefficient for the obvious reasons. Therefore, it is essential to replace the traditional diagnosis method by computer aided techniques to improve fault detecting means. To employ computer aided techniques, three main issues need to be addressed.

The first issue deals with feature extraction. That is data analysis process to represent each sample by a feature vector. The data analysis process varies depending on the source of data (dynamometer card, motor power curve). Fourier descriptor, curve moment, gray level matrix statistics, area, freeman chain code, etc are the

bases for feature extraction algorithms found in literature if the source data are dynamometer card. The characteristics of the selected extraction feature is required to be invariant to translation, rotation, scale, and starting point [48]. Memory requirement and computation speed are also important factors especially for online diagnosis. Fourier descriptor, geometric curve moment, and grey level matrix statistics were compared in [49] in terms of computing speed and memory requirement. The results indicate that Fourier descriptor is the fastest but requires more memory space with possible loss of information; curve moment is more time consuming and less memory consuming; while gray level matrix statistics provides good performance of speed and space. On the other hand, if the source of data is motor power curve, the authors in [50] noted that only the frequency feature is not enough to describe sucker rod pump working process hence they recommended to use some specific features that consider measures of data distribution and relate to some definite physical meaning.

The second issue relates to classification problem. This problem deals with a diagnostic model development that can maps an input feature vector to one of  $K$  working states. It is divided into inference problem and decision problem [51]. The inference problem deals in obtaining a model of posterior probabilities from a given training data. On the other hand, decision problem concerns in making optimal decision using posterior probabilities. The overall problem can be solved by solving first the inference problem and then the decision problem or by solving both problems together to find a discriminant function that maps inputs directly into decisions. For solving the inference problem or for finding a discriminant function, machine learning methods such Artificial Neural Network (ANN), Hidden Markov Model (HMM), SVM, Extreme Learning Machine (ELM), etc. are widely employed. When using SVM, ANN and ELM, the nature of training samples can be treated as independent and identically distributed. However, for many applications this assumption is far from reality. The sequential aspects of set of data can be treated using HMM, which is a time series model. For sucker rod pumps fault diagnosis purpose, SVM in [52–54]; ELM in [7; 55]; ANN in [56; 57] and HMM in [34; 50] were employed.

The third issue concerns on how to obtain sufficient training samples for all kinds of working states. There is a great challenge to gather required number of samples for various types of faults because only few working states occur form a given well in its life. An attempt to fill the requirement from different wells is not also effective because the wells have different properties. Furthermore, similar to other processes, the occurrences of the sucker rod pump working states have sequential nature. Therefore, the training set constructed with this approach contains reduced information about the given well. In addition to the challenges present for collecting samples, labeling for all samples takes larger workloads if manual classification (supervised learning method) is used. To reduce the workloads imposed by supervised learning method, semi-supervised learning method in [53] and unsupervised learning methods [58] have been used.

### 2.5.1 Feature Extraction

Feature extraction is an essential process in the development of computer aided diagnostic model. The valve working points are essential points for describing the operation of sucker rod pump. Fig. 2.5 shows a sample of motor power curve. On the motor power curve, the valleys correspond to the valve closing points and the peaks correspond to the valve opening points. When a change in working state occurs, the distance between the valve working points changes as well as the energy consumption at different parts of the cycle change. Thus, the following seven features can be defined:

- work coefficient of the four parts of a cycle are:

$$w_1 = \frac{1}{w} \int_{t_0}^{t_1} p(t) dt, \quad (2.1)$$

$$w_2 = \frac{1}{w} \int_{t_1}^{t_2} p(t) dt, \quad (2.2)$$

$$w_3 = \frac{1}{w} \int_{t_2}^{t_3} p(t) dt, \quad (2.3)$$

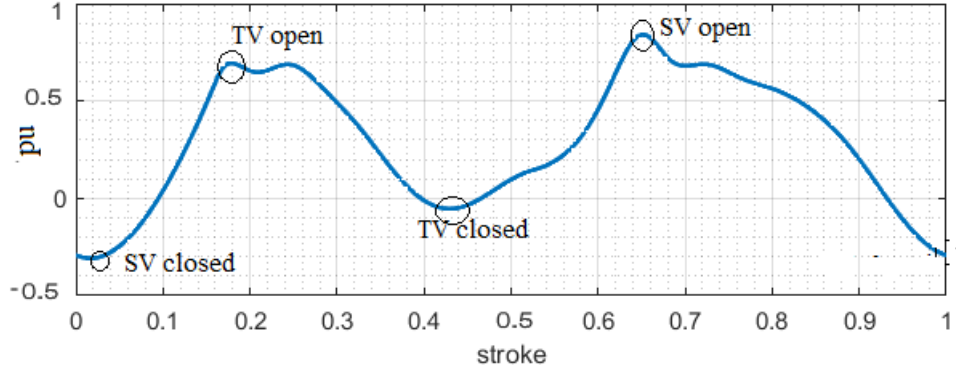


Fig. 2.5 — Valve working points on motor power curve

$$w_4 = \frac{1}{w} \int_{t_3}^{t_4} p(t) dt, \quad (2.4)$$

where:  $t_0 - t_1$  is the duration of first part of down stroke,  $t_1 - t_2$  is the duration of second part of down stroke,  $t_2 - t_3$  is the duration of first part of upstroke,  $t_3 - t_4$  is the duration of second part of upstroke,  $p$  is input power,

$$w = \int_{t_0}^{t_4} p(t) dt; \quad (2.5)$$

– the distance between SV open ( $x_{SV,o}, y_{SV,o}$ ) and TV open ( $x_{TV,o}, y_{TV,o}$ ):

$$L_a = \sqrt{(x_{SV,o} - x_{TV,o})^2 + (y_{SV,o} - y_{TV,o})^2}; \quad (2.6)$$

– the distance between SV closed ( $x_{SV,c}, y_{SV,c}$ ) and SV open ( $x_{SV,o}, y_{SV,o}$ ):

$$L_b = \sqrt{(x_{SV,c} - x_{SV,o})^2 + (y_{SV,c} - y_{SV,o})^2}; \quad (2.7)$$

– the distance between TV closed ( $x_{TV,c}, y_{TV,c}$ ) and TV open ( $x_{TV,o}, y_{TV,o}$ ):

$$L_c = \sqrt{(x_{TV,c} - x_{TV,o})^2 + (y_{TV,c} - y_{TV,o})^2}. \quad (2.8)$$

### 2.5.2 SVM Based Diagnostic Model

SVM is an artificial machine that can make judgment. It combines the inference and decision stages to simply learn a discriminant function that maps an input feature

vector directly into a class label. The property of SVM mattering much is that model parameters are results of the solution of a convex optimization problem, so that any local optimum is also a global optimum [51]. SVM also requires less computation time than other machine learning methods during training.

In order to understand how the SVM algorithm solves the classification problem, let's start with the two-class classification problem as shown in Fig. 2.6. Assume the training set is defined as  $\{x_n, t_n\}_{n=1}^N$  and the decision function is defined by:

$$y(x) = w^T \varphi(x) + b, \quad (2.9)$$

where:  $x_n \in R^n$  – inputs,

$t_n \in \{-1, 1\}$  – class label such that  $t_n = 1$  and  $t_n = -1$  represent class 1 and class 2 respectively,

$\varphi(x)$  - fixed feature space transformation,

$b$  – the bias parameter,

$w$  – normal to the hyperplane.

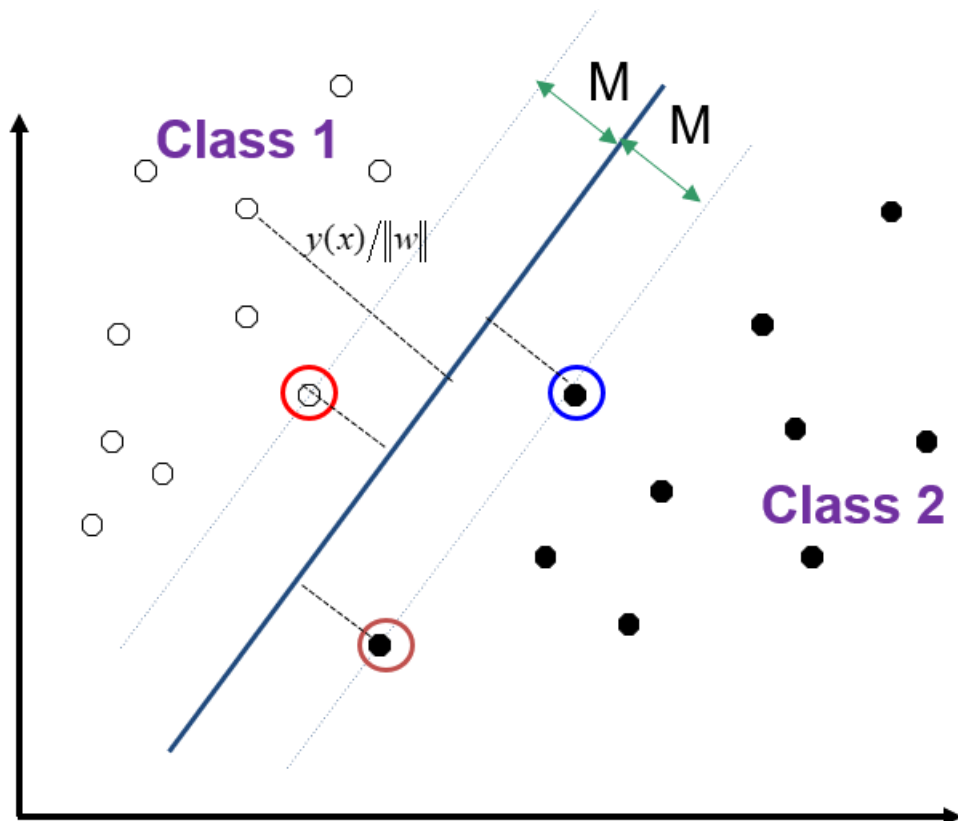


Fig. 2.6 — Linear decision boundary

For a given new data  $x$ , the class label can be predicted using the sign of decision function. If  $y(x) > 0$ ,  $x$  is associated to class 1 otherwise to class 2. If the decision function is a linear function of the input vector  $x$ , then class 1 and class 2 are said to be linearly separable. For any point  $x$  in either class 1 or 2, its shortest distance from the decision boundary is:

$$\frac{t_n y(x_n)}{\|w\|} \geq M, \quad (2.10)$$

where:  $M$  is the maximum margin.

Learning by SVM algorithm is intended to search parameters  $w$  and  $b$  that maximize  $M$ . The optimal parameters  $(w, b)$  can be obtained by solving (2.11):

$$\arg \max_{w,b} \left\{ \frac{1}{\|w\|} \min_n [t_n y(x)] \right\}. \quad (2.11)$$

Recognizing that rescaling the parameters  $w$  and  $b$  does not produce any effect on the value of  $\frac{t_n y(x_n)}{\|w\|}$ , the constraint equation can be set freely as:

$$t_n y(x_n) \geq 1, \quad (2.12)$$

then, the problem in (2.11) will be equivalent to maximizing  $\frac{1}{\|w\|}$  or minimizing  $\|w\|^2$ . Therefore, the optimization problem (2.11) is replaced by:

$$\arg \min_{w,b} \frac{1}{2} \|w\|^2, \quad (2.13)$$

$$s.t \quad t_n y(x_n) \geq 1.$$

The method of Lagrange multipliers is convenient in solving a constrained optimization problems. If for each constraint  $a_n \geq 0$  is introduced as a Lagrange multiplier, then the above problem can be transformed to (2.14).

$$L(w,b,a) = \frac{1}{2} \|w\|^2 - \sum_{n=1}^N a_n (t_n y(x_n) - 1) \quad (2.14)$$

The results of the derivative of with respect to  $w$  and  $b$  are given in (2.15) and (2.16) respectively.

$$w = \sum_{n=1}^N a_n t_n \varphi(x_n) \quad (2.15)$$

$$0 = \sum_{n=1}^N a_n t_n \quad (2.16)$$

Using (2.15) and (2.16), (2.14) is further reduced to quadratic programming problem as given by:

$$L(a) = \sum_{n=1}^N a_n - \frac{1}{2} \sum_{n=1}^N \sum_{m=1}^N a_n a_m t_n t_m K(x_n, x_m), \quad (2.17)$$

$$\begin{aligned} \text{s.t. } a_n &\geq 0, \\ \sum_{n=1}^N a_n t_n &= 0, \end{aligned}$$

where:  $K(x_n, x_m) = \varphi(x_n)\varphi(x_m)$  is kernel function.

Using (2.9) and the kernel function, the discriminant function can be rewritten as:

$$y(x) = \sum_{n=1}^N a_n t_n K(x_n, x_m). \quad (2.18)$$

An interesting property of the optimization problem in (2.17) is that for any data point, the following holds:

$$a_n = 0 \quad \text{or} \quad t_n y(x_n) = 1.$$

Those points which satisfy  $t_n y(x_n) = 1$  are called support vectors. Therefore, only support vectors are used to construct the decision function. The bias parameter can be determined by averaging for all support vectors as given below:

$$b = \frac{1}{N_s} \sum_{n \in S} (t_n - \sum_{m \in S} a_m t_m K(x_n, x_m)), \quad (2.19)$$

where:  $N_s$  is the total number of support vectors.

The assumption that class 1 and class 2 are linearly separable can be relaxed by introducing a slack variable  $\xi_n \geq 0$  for each training data point, which modifies the constraint equation as given in (2.20) in order to modify SVM.

$$t_n y(x_n) \geq (1 - \xi_n) \quad (2.20)$$

Then, learning by the SVM algorithm will be to minimize:

$$C \sum_{n=1}^N \xi_n + \frac{1}{2} \|w\|^2, \quad (2.21)$$

where:  $C > 0$  is control parameter.

Introducing Lagrange multiplier  $a_n \geq 0$  and  $\mu_n > 0$ , the corresponding Lagrangian can be written as:

$$L(w, b, a) = \frac{1}{2} \|w\|^2 + C \sum_{n=1}^N \xi_n - \sum_{n=1}^N a_n (t_n y(x_n) - 1 + \xi_n) - \sum_{n=1}^N \mu_n \xi_n. \quad (2.22)$$

Taking the derivative of  $L(w, b, a)$  with respect to  $w$ ,  $b$ , and  $\xi_n$ , (2.22) is reduced to (2.23).

$$L(a) = \sum_{n=1}^N a_n - \frac{1}{2} \sum_{n=1}^N \sum_{m=1}^N a_n a_m t_n t_m K(x_n, x_m) \quad (2.23)$$

s.t

$$0 \leq a_n \leq C$$

$$\sum_{m=1}^N a_n t_n = 0$$

Based on Karush-Kuhn-Tucker conditions, the decision making process can be summarized as given in Table 6.

Table 6 — Illustration of slack variable

Value of $a_n$	Value of $a_n$ compared to $C$	Value of slack variable	Role of data point	Decision
$a_n = 0$			no effect	
$a_n > 0$	$a_n < C$	$\xi_n = 0$	support vector	correctly classified
$a_n > 0$	$a_n = C$	$\xi_n \leq 1$	lie inside margin	correctly classified
$a_n > 0$	$a_n = C$	$\xi_n > 1$	lie inside margin	misclassified

For all support vectors for which  $0 < a_n < C$  and  $\xi_n = 0$ , the following is satisfied:

$$t_n \left( \sum_{m \in S} a_m t_m K(x_n, x_m) + b \right) = 1, \quad (2.24)$$

and the bias parameter can be obtained by averaging them.

A  $K$  class discriminant functions can be constructed by extending the two-class discriminant using one-versus-the-rest classifier or one-versus-one classifier. The one-versus-the-rest leaves ambiguous regions in the feature space because in this approach

the multiclass problem is reduced into two class problem. On the other hand, one-versus-one classifier builds  $K(K - 1)/2$  binary classifiers to distinguish only two classes.

## 2.6 Simulation Results

### 2.6.1 Training Data Generation

The need of computer aided diagnostic techniques are becoming important for sucker rod pump installations. To develop computer aided diagnostic techniques, large number of training data that represent the different working states is required [34]. However, there is difficulty in obtaining required amount of training data. This difficulty can be addressed using a sucker rod pump simulation model as shown in Fig. 1.9.

By assuming different combinations of dynamic height and pumping speed, it is possible to produce a number of samples that represent normal working state. A number of samples for fault working states can also be produced by assuming variations in the most influencing parameter of the desired fault. Since, most common faults are due to problems created in the subsurface pump, the effect of such problems can be simulated by changing inflow parameters in the reservoir model, liquid properties, or assuming mechanical problems. In this way, 72 labeled dynamometer card and motor power curve have been generated to construct a training set. In this simulation, the training set consists of samples representing normal working state, insufficient liquid supply, traveling valve leakage, gas affected, plunger hitting top dead center and plunger hitting bottom dead center. In this research only the labeled motor power curve is used as a source of data in the development of the diagnostic model. For each sample, the required features are extracted to construct a feature vector using the proposed method. Table 7 presents the average value of the feature extraction vectors for of all samples with the same label. For a given sucker rod pump, it can be said that the feature vectors

representing samples with the same label are similar and different from the other labeled samples.

Table 7 — Average values of extracted feature

State	$L_a$	$L_b$	$L_c$	$w_1$	$w_2$	$w_3$	$w_4$
Nor.	0.425	0.797	0.453	0.397	0.217	0.202	0.184
Lik.	0.477	0.729	0.462	0.355	0.217	0.241	0.187
Gaf.	0.416	0.799	0.503	0.488	0.247	0.102	0.204
Ins.	0.398	0.793	0.450	0.486	0.257	0.054	0.203
Bpb	0.422	0.711	0.437	0.185	0.183	0.409	0.222
Bpt	0.436	0.702	0.434	0.204	0.187	0.388	0.222

*Nor.* — normal working state;

*Lik.* — standing valve leakage;

*Gaf.* — gas affected;

*Ins.* — insufficient liquid supply;

*Bpb.* — the condition when hits bottom dead center;

*Tpb.* — the condition when the plunger hitstop dead center.

Fig. 2.7 to Fig. 2.12 present dynamometer card and motor power curve for a representative sample of each working state. Fig. 2.7 shows the dynamometer card and motor power curve for normal working state. The dynamometer card looks like a parallelogram slightly rotated to the right. This shape is a characteristic feature of normal working state. The motor power curve shows two comparable peaks, which obviously correspond to the horizontal positions of the crank. As compared to the dynamometer card for normal working state, the dynamometer card in Fig. 2.8 has slight absence in the right bottom corner. This is typical characteristic of gas affected condition. The dynamometer card shown in Fig. 2.9 has parabolic curve at left upper portion, which characterize the effect traveling valve leakage. In Fig. 2.10, the dynamometer card lacks the right bottom corner, which characterize the effect of insufficient liquid supply. Fig. 2.11 has a bulge at the left bottom corner, which indicates the effect of plunger hitting bottom dead center. Similarly, Fig. 2.12 has a bulge at the right top corner, which indicates the effect of plunger hitting top dead center. From the curves in Fig. 2.7 to Fig. 2.12, it is not easy to diagnose sucker rod pump visually from motor power curve.

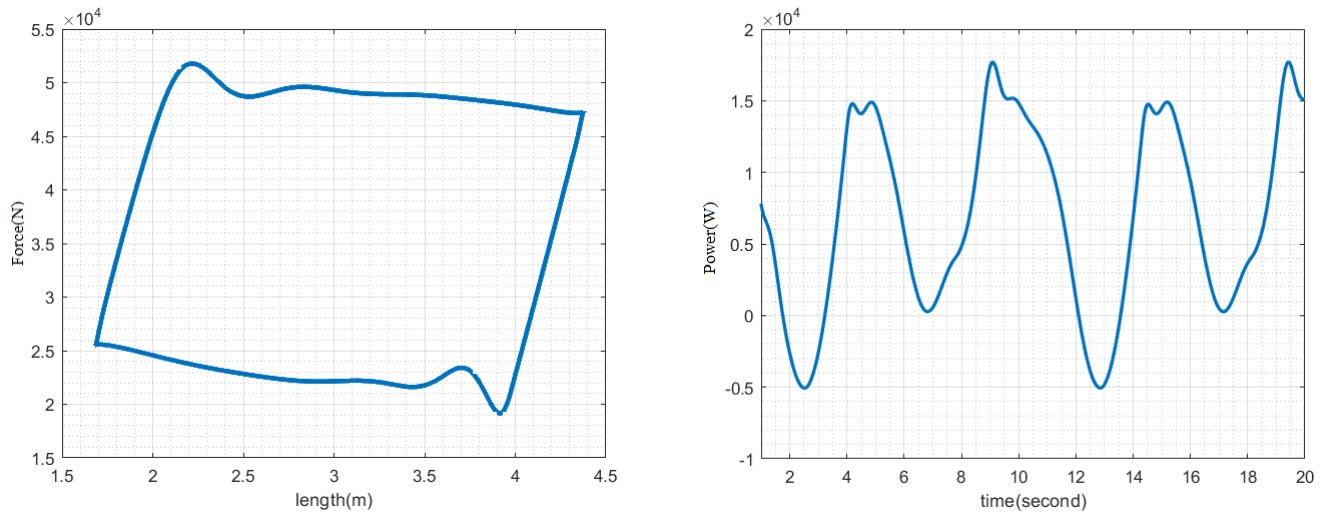


Fig. 2.7 — Normal working state

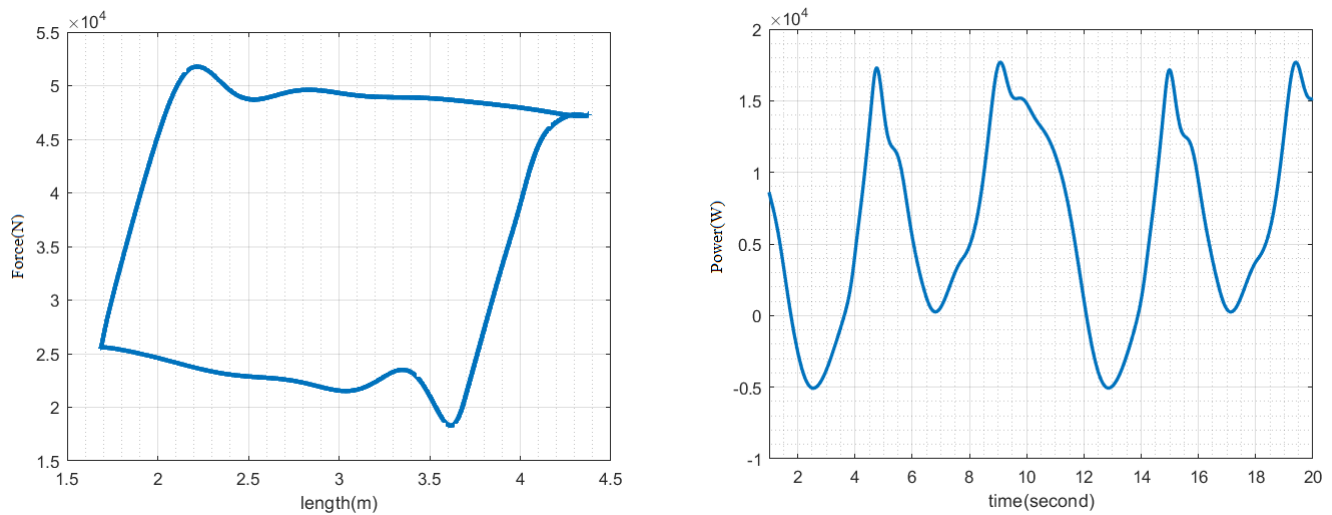


Fig. 2.8 — Gas affected

However, each sample can be represented by a feature vector. And then using computer aided techniques the diagnosis process can be performed.

### 2.6.2 Diagnosis

The overall classification process of sucker rod pump is divided into training and diagnosis as shown in Fig. 2.13. The training process is performed offline while the diagnosis process can be performed in real time. In offline, large number of labeled samples of motor power curves are collected. For each sample required features are

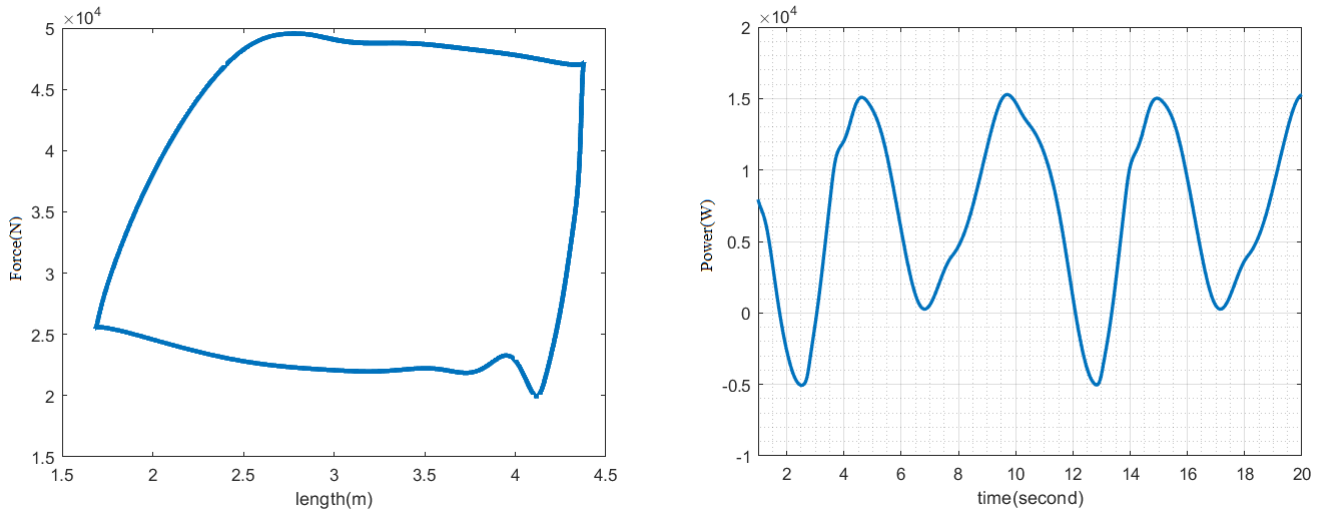


Fig. 2.9 — Travelling valve leakage

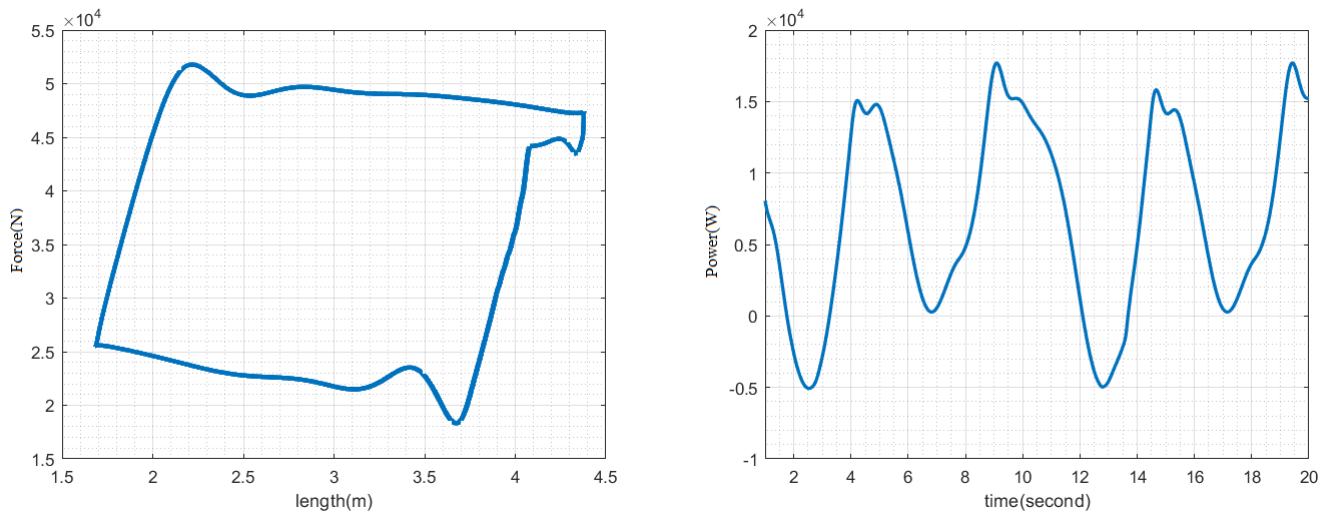


Fig. 2.10 — Insufficient liquid supply

extracted to build a training set. Then, the SVM algorithm uses the training set to produce SVM parameters which are used to construct decision functions. In real time, motor power curve is processed to produce a feature vector. Then, the classifier uses the produced feature vector and SVM parameters to detect the working state. The diagnosis results are presented in Table 8. It can be seen that all the samples for normal, travelling valve leakage, gas affected working states are correctly classified. However, three samples of insufficient liquid supply are incorrectly classified as gas affected and two samples are as normal.

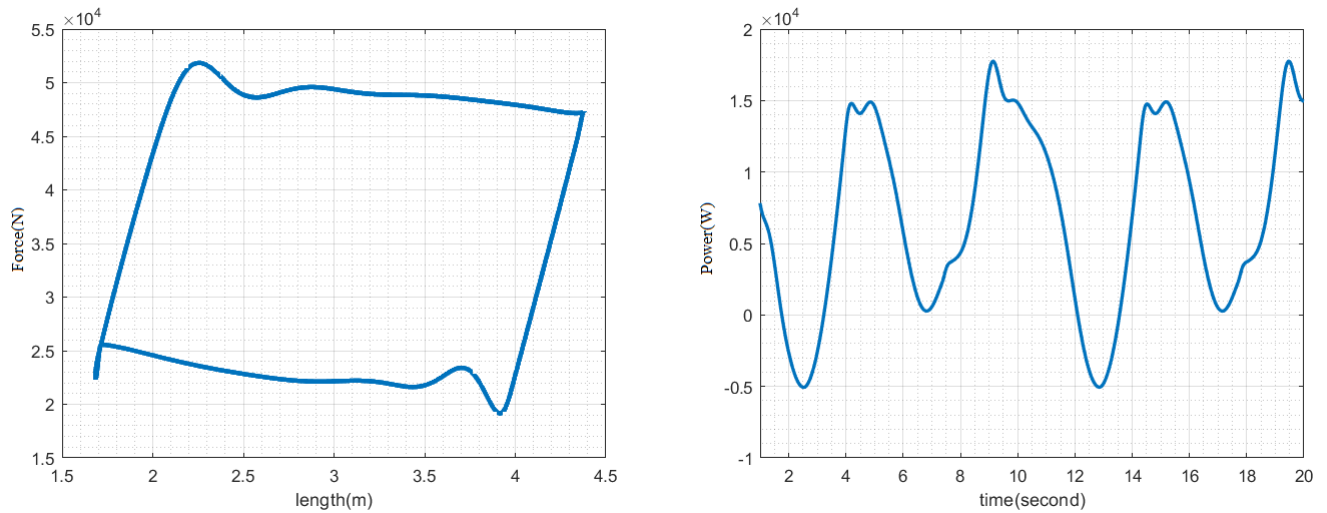


Fig. 2.11 — Plunger hitting bottom dead center

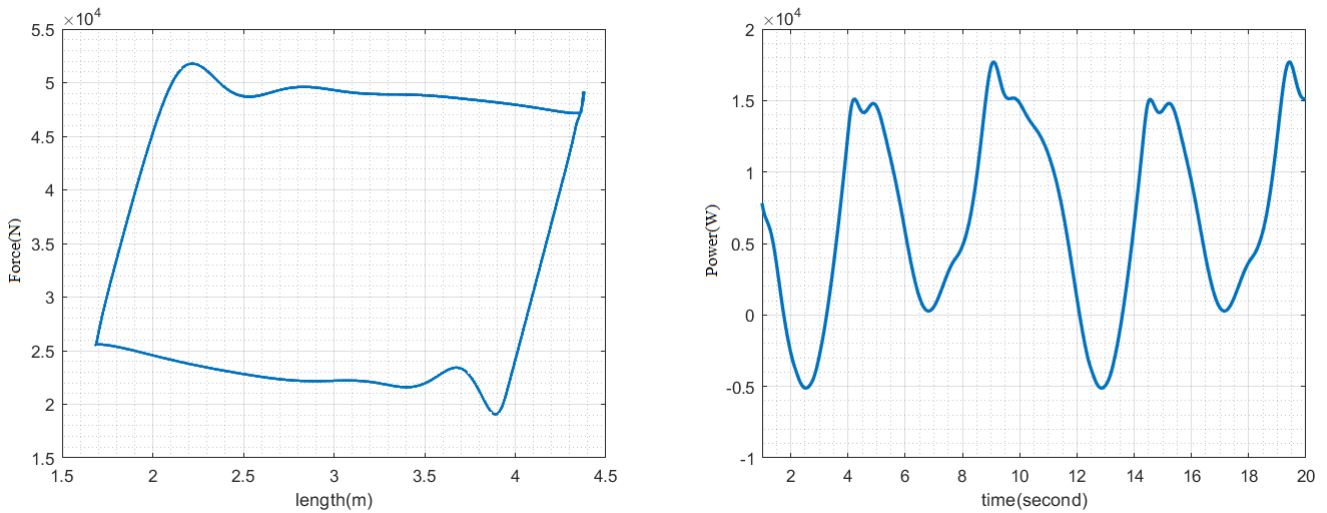


Fig. 2.12 — Plunger hitting top dead center

Table 8 — Confusion matrix

State	Nor.	Lik.	Gaf.	Ins
Nor.	12	0	0	0
Lik.	0	12	0	0
Gaf.	0	0	12	0
Ins.	2	0	3	7

## 2.7 Summary

Most common faults are attributed to abnormal changes in subsurface conditions or defects of downhole components such as subsurface pump, sucker rod string, valves and tubing. Knowledge of the subsurface condition is important for monitoring the

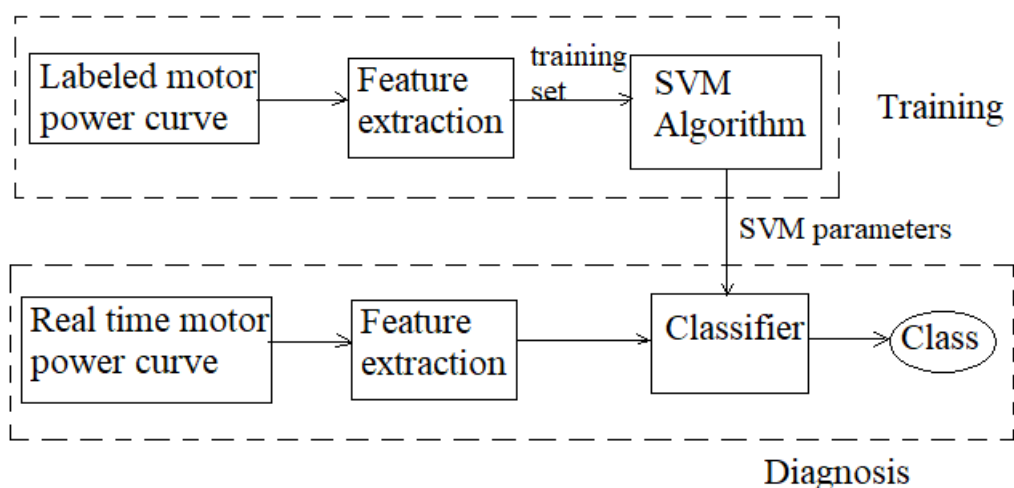


Fig. 2.13 — Diagnostic model

performance of sucker rod pump. Generally, the source of information about the subsurface condition can be grouped into three. The first source is from measurements of the well's operational parameters using various types of sensors. The second source is dynamometer card, which is constructed from sensor based measurements of polished rod load and displacement. The third source is the motor power curve, which is obtained from voltage and current measurements.

Traditionally, the different working states of sucker rod pump are uniquely identified from the dynamometer card. Therefore, the information obtained from the well's operational parameters and motor power has to be correlated with the dynamometer card. It was found difficult to correlate the information obtained from the well's operational parameters to the dynamometer card. In addition, this source is based on various sensors, which have low reliability. Therefore, its application is limited. On the other hand, dynamometer card can be easily derived from motor power curve. There is also possibility to directly diagnose the sucker rod pump working state from motor power curve. However, computer aided technique is vital in order to employ motor power curve for diagnosis. Three issues have been identified that challenge for successful implementation of computer aided techniques. The first issue, which deals with feature extraction, have been addressed by representing each sample by a feature vector constructed based on distance between valve working points and energy dissipation in the four parts of the pumping cycle. The second issue, which deals with

classification problem, have been solved by using SVM. The third issue, which deals in building an album of training set, has been addressed using a simulation model. The proposed solution have been tested in simulation and results indicate satisfactory accuracy of the SVM classifier. The SVM algorithm, the program for classification and feature extraction processes have been developed in MATLAB programming environment but they can also be rewritten in other programming environments. Moreover, the program for classification and feature extraction processes can be prepared to run on simple device, which can be used for onsite applications, with the training process performed in a centralized unit.

## **Chapter 3. Optimal Energy Efficiency Operation of Sucker Rod Pump**

### **3.1 Introduction**

There are nearly 920,000 oil producing wells worldwide and approximately 71% of these wells use sucker rod pumping system [59]. Most sucker rod pumps are driven by an asynchronous motor and require large amounts of energy to lift oil to the surface. If by means of energy saving techniques, the power consumption for a single unit can be reduced by small amount, the resulting economic benefit can be significant.

In this chapter, an integrated model consisting the models of AC-DC-AC converter, induction motor, sucker rod pump is developed to study the energy consumption of sucker rod pump installations. Best efficiency operation is obtained by finding an optimal magnetizing current trajectory for one cycle of pump operation. The optimal magnetizing current trajectory is obtained by examining the energy consumption of all possible flux producing current trajectories in offline. Then, it can be uploaded to the controller and be used until there is change in load torque trajectory.

### **3.2 Sucker Rod Pump Drive's Power Requirement**

The power input to the sucker rod pump drive is used to lift fluid and overcome all types of losses in the prime mover, surface and subsurface transmissions. Fig. 3.1 shows the power flow in sucker rod pump system.

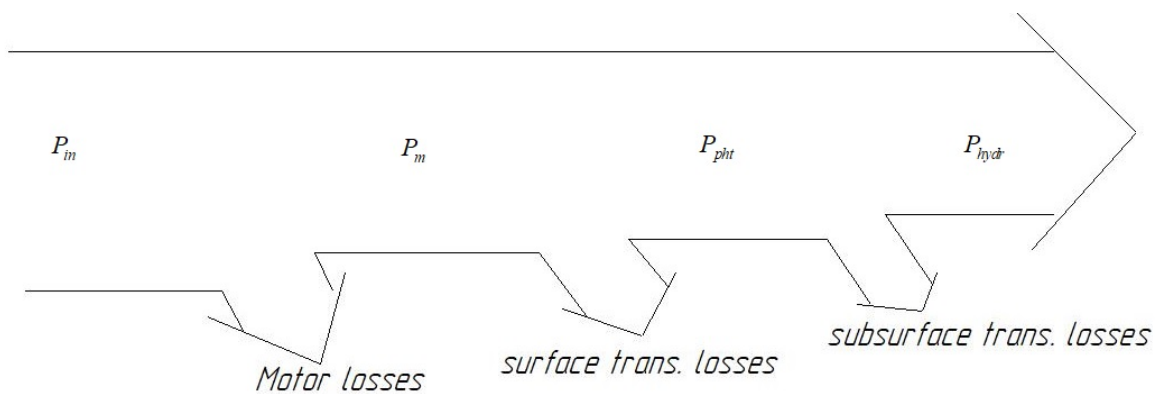


Fig. 3.1 — Power flow in sucker rod pump

### 3.2.1 Subsurface Energy Losses

The subsurface energy losses occur due to different causes. In the subsurface pump, there are inevitable frictional and hydraulic losses in addition to that due to leakage. The up and down movement of the sucker rod string also causes frictional losses in case it rubs the tubing. Moreover, the produced liquids may pass on damping force on the sucker rod string and cause other hydraulic losses. Thus, the mechanical power input at the polished rod equals the useful hydraulic power by the pump plus all the subsurface losses. The quotient of the useful hydraulic power to the power required at the polished rod is termed as lifting efficiency [60] and given by:

$$\eta_{lift} = \frac{P_{hydr}}{P_{pht}}, \quad (3.1)$$

where,  $P_{hydr}$  – useful hydraulic power,

$P_{pht}$  – the power input at the polished rod.

The lifting efficiency is highly dependent on the pumping mode (combination of plunger size, stroke length, pumping speed) [4]. Thus, in order to achieve maximum possible lifting efficiency, the sucker rod pump must be operated at optimal pumping mode.

The effective work done to lift the fluid depends on the polished rod load. The useful work done at the polished rod can be given by:

$$W_{pht} = F_{pht} v_{pht} (\theta_{cr}) dt, \quad (3.2)$$

where:  $F_{pht}$  is polished rod load,

$v_{pht}$  is velocity of polished rod.

Equation (3.2) indicates that any technique which is capable to reduce the polished rod load can help to save some energy. Moreover, such technique can also help to maintain the polished rod load within permissible range, thereby ensuring safe pump operation [61].

The polished rod load is the sum of static loads (sucker rod and fluid weight) and dynamic loads (inertial load, vibration load, friction load and elastic force). Obviously, a lighter load material will effectively reduce the polished rod load. Thus, the use of fiber glass, which has good structural strength and lower density compared to steel, produces a reduced polished rod load. Dynamic loads also account a considerable part of the polished rod load. In [62; 63], shock absorber has been used to reduce dynamic loads on the pumping unit and the intensity of applying loads to the sucker rod string. Other subsurface pump designs such as the use of small pump diameters and side flow pump [64] also help to reduce the liquid pressure load, thereby reducing the polished rod load. The load reducer [61], which is installed at certain depth, is also another technique used to reduce the polished rod load by producing counteractive force. However, the use of these techniques may cause certain problems which limit their promotion for wide application. Of all techniques, the load reducer is still the most effective because short service life for shock absorbers, increased resistance on the plunger for side flow pumps, reduced production rate for small pump diameters, incompatibility of fiber glass in certain conditions such as high temperature, heavy oil and deviated wells limit their use [65].

### 3.2.2 The Surface Transmission Energy Losses

The surface transmission loss is associated with frictional losses that arise in the surface components such as in the stuffing box, gear reducer, pumping unit's structural

bearing and V-belt. The efficiency of the surface transmission system, as reported in [66] is relatively high and nearly constant for a wide range of load rate. However, if large load fluctuation and variable equivalent inertia are considered, the rotating vibrational loss increases [59]. This assumption complicates the analysis because surface model, which is currently based on one degree of freedom need to be replaced by surface model based on two degrees of freedom. In [65], correlation functions presented in Table 9 are used to approximate for the transmission efficiency of prime mover, v-belt, gear reducer and four-bar linkage mechanism. Since, the variation of transmission efficiency is small with change in load, there is no need to improve transmission efficiency.

Table 9 — Correlation function of transmission efficiency [65]

<b>Content</b>	<b>Correlation function</b>
Prime mover	$-95e^{\frac{-P}{2.75}} - 0.175 + 95$
Belt	$0.98 - 0.98e^{\frac{-P}{5.5}} - 0.00001P^2$
Gearbox	$0.97 - 0.97e^{\frac{-P}{2.9}} - 0.00004P^2$
Four bar leakage	$0.94 - 0.94e^{\frac{-P}{2.9}} - 0.00003P^2$

### 3.2.3 Optimal Counterbalance

Due to the inherent characteristics of the pumping unit, sucker rod pump has poor balance effect, bigger fluctuation of gearbox torque, existence of negative torque, lower work efficiency and bigger consumption of energy. To overcome these issues, a counterweight is placed at the crank or at rear end of walking beam. As a result, net torque can be smoothed and a relatively uniform loading on the prime mover can be ensured. As reported in [67], the use of proper counterbalance has the following beneficial effects:

- torque rating of gear reducer can significantly be decreased compared to unbalanced condition;

- the size of the required prime mover is also smaller with an associated lower energy demand for pumping;
- the smoother operation of a properly balanced speed reducer lowers maintenance costs and increases equipment life.

There is no standard approach adapted for determining the optimal counterbalance [68]. However, optimal counterbalance condition is characterized by equal peaks of net torque during up and down stroke, equal energy consumption for upstroke and down stroke, minimum cyclic load factor (CLF) based on the net load torque. CLF is defined as the ratio of the root mean square to the average net gearbox torques over the pumping cycle:

$$CLF = \frac{\int_0^{2\pi} \sqrt{[M_s(\varphi_{cr})]^2} d\varphi_{cr}}{2\pi} \cdot \frac{\int_0^{2\pi} [M_s(\varphi_{cr})] d\varphi_{cr}}{2\pi}. \quad (3.3)$$

The energy consumed over the pumping cycle ( $W_m$ ) can also be calculated by:

$$W_m = \int_0^T p dt, \quad (3.4)$$

where:  $p$  – motor input power,

$T$  – the period of one pumping cycle.

Since, there is a linear relation between the torque and current in electric motors, the peak currents in the up and down stroke can indicate the degree of balance [8]. The balance coefficient can be defined as:

$$K_{ub} = \frac{I_{mu} - I_{md}}{I_{mu} + I_{md}}, \quad (3.5)$$

where:  $I_{mu}$  – the maximum current during the upstroke,

$I_{md}$  – the maximum current during the down stroke.

Proper balance is characterized by nearly equal peak currents during up and down stroke. Hence, small absolute value of  $K_{ub}$  indicates better balance condition. However, diagnosis for balance condition through current measurements is not always trusted because ammeters cannot distinguish between motor or generator operation. The report in [67] associates the optimal counterbalance with the condition that produces minimum

CLF. In the report [68], the optimal counterbalance is associated with the condition that produces minimum energy.

A counterweight attached to the crank is the most common arrangement used to balance the pumping unit. The torque due to this counterweight opposes the rod torque in direction and can easily be expressed as:

$$M_{cb} = -M_{cbmax} \sin(\varphi_{cr} + \tau'), \quad (3.6)$$

where:  $\tau'$  – offset angle.

Optimal balance is achieved if the size and position of counterweight are correctly selected. The size of the counterweight can be determined simply using the fact that the crank angles where the net gearbox torque attains maximum value during the up and down stroke are the same whatever degree of balance may be. Thus, if the offset angle is zero and inertial torques are neglected, the optimal maximum counterbalance torque can be calculated by Gibb's proposal [69]:

$$M_{cbmax} = \frac{M_{pht}(\varphi_{cru}) - M_{pht}(\varphi_{crd})}{\sin \varphi_{cru} - \sin \varphi_{crd}}, \quad (3.7)$$

where:  $M_{pht}$  – polished rod torque,

$\varphi_{cru}$  – the crank angle at which the net gearbox torque reaches maximum value during up stroke,

$\varphi_{crd}$  – the crank angle at which the net gearbox torque reaches maximum value during the down stroke.

Alternate approach is presented in [70] to estimate optimal size of counterweight that results minimum root mean square using adaptive torque and rotor speed observers. This approach enables to examine the balance condition based on electrical measurements and can avoid the need for sensors.

Traditionally, the arrangement is such that counterweight's combined center of gravity falls on the center line of the crank. With this assumption, the counterbalance torque can be changed by changing the size of the counterweight and position of the counterweight. However, it seriously reduces the possible number of counterbalance arrangements [8]. Better balance can be achieved with other arrangements like structure of lower barbell pumping units with compound balance [71].

### 3.2.4 Reducing Inertial Torque

The nature of the crank speed depends on type of the prime mover used. Low slip electric motors drive the crank at constant speed whereas high slip electric motors or multicylinder engine drive the crank at varying speed [72]. However, the angular speed of the walking beam varies whatever the crank speed may be. This causes the structural parts of the pumping unit to store and release energy. Consequently, inertial torque known as articulating torque is produced. If the crank speed is not constant, the acceleration/deceleration coupled with heavy masses also produces rotary inertial torque. The inertia of each element can be determined as presented in chapter 1.

The nature of crank speed curve determines the distribution of inertial torques. The reports in [73; 74] proposed motor speed control to redistribute inertial torque and reduce load variation. However, a simple way is required to formulate the optimal speed curve. Open and closed loop control schemes are used to minimize the fluctuations in the motor output [75]. Although the articulating torque exists even if the crank speed is constant, it has negligible effect on the net torque. In addition, the effect of rotary torque is also small. For example, a 15% speed variation over the average speed introduces less than 10% error in the net torque if inertial torques are neglected [76].

### 3.2.5 Sucker Rod Pump Prime Movers

Sucker rod pump systems use either internal combustion engine or electric motors to generate the required mechanical energy. Several factor such as initial cost, service life and operational cost are considered when making a choice between internal combustion engine and electric motor.

Internal combustion engines are available with operational speed that ranges from 200 to 2000 rpm. Slow speed engines ensure correct operation under cyclic loads

because the variation of the developed torque over a large range of speeds is small. Similarly, electric motors are also available with different operational characteristics, some of which are especially designed to suite sucker rod pumping services [67].

Fig. 3.2 shows the relative torque-speed characteristics of National Electrical Manufacturers Association (NEMA) design A, B, C, D and E motors [77]. NEMA design B characteristic is commonly adapted for designing industry standard motors. Class B motors are characterized by normal locked rotor torque, normal locked rotor current, normal slip, and a higher breakdown torque. However, the normal design parameters of design B does not meet the torque-speed characteristic demanded by some applications such as sucker rod pump systems. For sucker rod pump installations, design D motors are the most favored. The most important characteristic of this design is a high locked rotor torque which is sufficient to start the pumping unit. In addition, design D motors have high slip characteristic. Therefore, a small variation in torque is reflected by a larger speed change.

Most sucker rod pump installations are driven by induction motor. In induction motor, the forms of energy losses are the stator cooper losses, iron losses, rotor cooper losses, windage and frictional losses. Due to these losses, the mechanical power output is less than the electrical power input. Moreover, the load on the motor shaft fluctuates even if the pumping unit is optimally balanced. This kind of load demands a significantly overrated motor as the sizing need to consider the peak load. Fig. 3.3 shows the effect of load variation on the motor performance curves. The efficiency is lower when an overrated motor is used. The study conducted by [78] on oil producing well in one of the fields in Western Siberia is a good example.

The overall efficiency for sucker rod pump installations is the product of lifting, surface transmission, and motor efficiencies. The lifting efficiency can be improved by selecting the optimal pumping mode. The surface transmission efficiency is nearly constant with change in load if proper maintenance is done. The effect of the counterbalance torque and inertial torque on the mechanical efficiency is negligible since the average power due to the counterbalance and inertial torque is zero. The

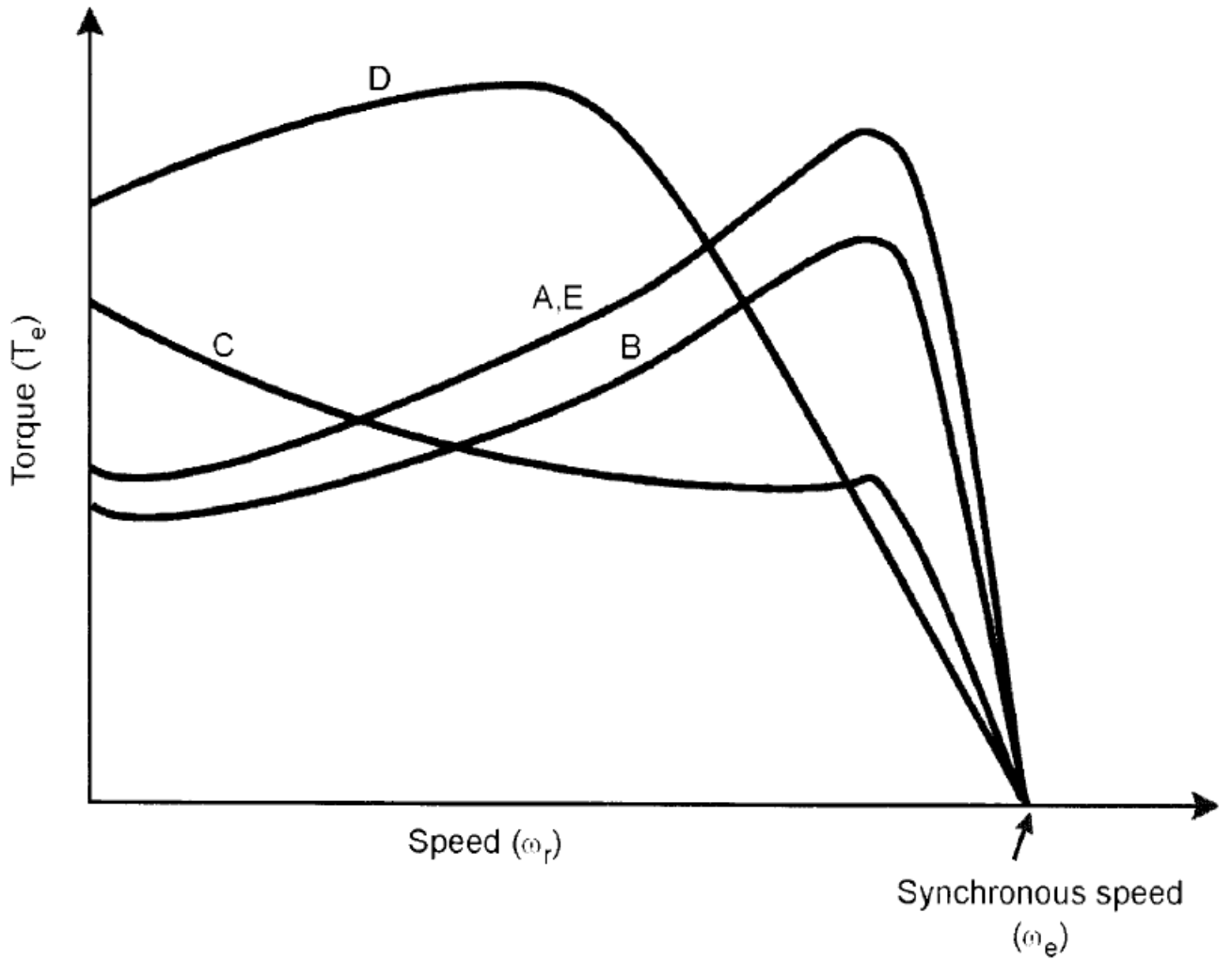


Fig. 3.2 — Torque vs speed characteristics of NEMA motors [77]

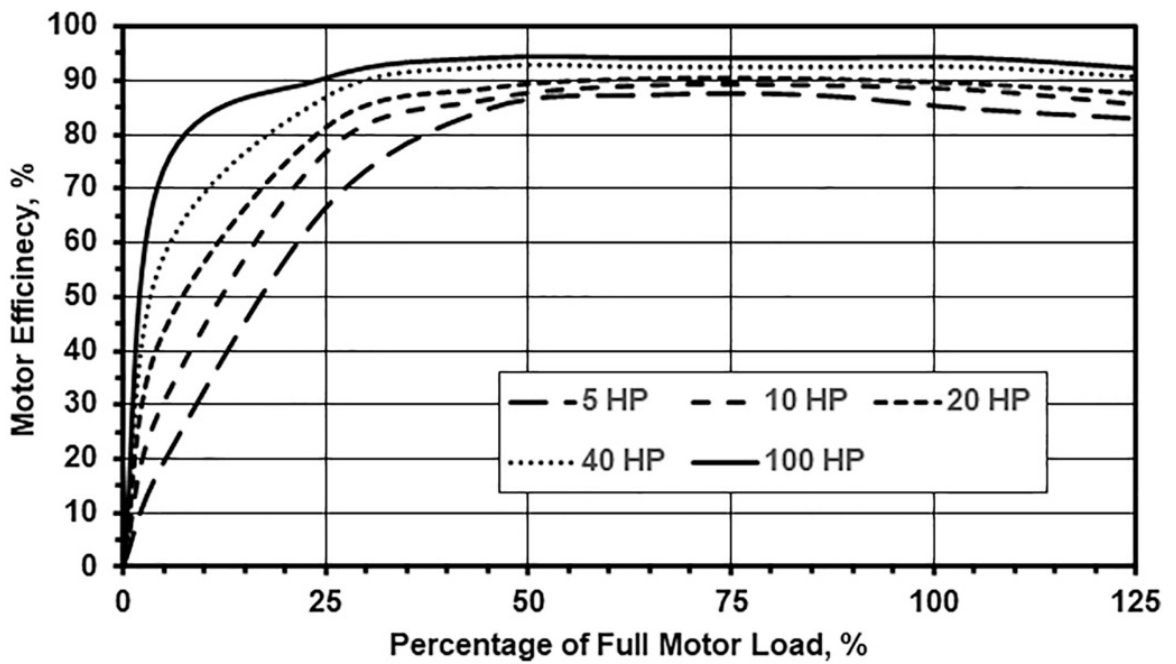


Fig. 3.3 — Average efficiencies of different vendors' electric motor [79]

motor efficiency can be improved by minimizing the controllable losses. The following reviews efficiency optimization methods for induction motor.

### **3.3 Review of Efficiency Optimization Methods for Induction Motor**

World wide, the energy consumed by electric motors is high. It reaches about 70% of the total energy consumption but must be noted that three phase induction motors in the power range 0.75KW to 750KW consume close to 90% of the total share [80]. Induction motor is without doubt the workhorse of electric power industry [77]. It is the source of motive power in most common applications such as pump, lift, exhaust fans, hoist drives etc. Its simple, strong and effective construction, good efficiency, and low cost are the main factors that encouraged its use in wide applications. However, most induction motors are operated at low efficiency because in most industries the use of the same type of motor is widely adapted for reasons of standardization practices and maintenance costs [81]. In order to meet the energy efficiency targets and standards, there is demand to operate induction motor at optimal efficiency by control means. But, this is more difficult because induction motor is represented by a nonlinear system with a coupled multi-input multi-output system.

For any desired application, an improved electric motor performance can be achieved by adapting suitable design forms. In today's market, different types and design categories of electric motor are available. For example, cage-type induction motor can be found in design A, B, C, D and E according to NEMA classification, which is based on the torque-speed characteristics. The most significant machine parameter in this classification is the actual rotor resistance [77]. The difference in the torque-speed characteristics among the different designs is wide. Therefore, familiarity with the different designs and their characteristics is essential in order to select suitable induction motor design for a particular application. Design B and C are most commonly used designs [82]. Design B motors are often used for applications that operate at nearly

constant speed. They are characterized by steep characteristics of speed-torque, speed-current and speed-efficiency close to the nominal operational speed [15]. Therefore, a small change in the speed causes large changes in the efficiency and stator current. This means, the use of this type of motors is not recommended in applications such as sucker rod pump which apply a variable load. Induction motors with design D have better characteristic under cyclic loading and are the most preferred for these types of applications. Design D induction motors are characterized by high starting torque, low starting current and high operating slip [83].

An improved electric motor performance can also be achieved by controlling the drive to operate at optimal operating point. To determine the optimal operating point, it is essential to develop optimization model. Optimization models for different types of electric drives are presented in [84]. These optimization models include electromechanical and energy models with a freely variable vector for control actions at the input, vector which determines the conditions of the technological problem and a vector quality indicator at its output. For an induction motor, slip or rotor flux can be varied freely without affecting the technological problem and hence either of them can be chosen as a control variable for optimization. On the other hand, power loss, stator current, power factor, etc., could be selected as quality indicators.

The input power to induction motor drive is used to perform the required useful work and overcome all types of losses in the motor and converter. At nominal operating condition, the efficiencies of converters can reach 98% and the efficiencies of medium and high rating motors are over 95% whereas, at partial loads the efficiency declines considerably [33]. Power loss in converter appears in the form of conduction and commutation losses. It does not need any pay attention in efficiency optimal control if small drives are considered [85; 86]. Power loss in the motor include copper, iron and mechanical losses. Since, copper and iron losses are controllable, it is possible to operate the drive at optimal efficiency by control means. However, the design of control system requires comprehensive loss model development of the drive system. The comprehensive loss model can be derived from representative equivalent circuit. The stator and rotor copper losses produce heating effect, which can be represented

by using resistors in the equivalent circuit. Mechanical losses are dependent on the rotor speed but are free from the influence of stator and rotor currents. Their effect can be included into the mechanical equation using viscous friction coefficient and dry friction torque because they appear in form of frictional and the aerodynamic losses. In contrast, iron losses have magnetic nature and their effect can be realized either using an equivalent torque in the mechanical equation [87] or an equivalent resistor [33; 85–89] in the equivalent circuit.

In a vector-controlled induction motor drive, if the rotor flux vector is fixed to the real axis of the coordinate system, the estimated torque is proportional to the product of torque producing current and rotor flux. The required torque producing current is provided by the speed controller but the rotor flux can be set based on optimal energy efficiency targets. Since with decrease in rotor flux the copper losses increase whereas iron losses decrease, operation at optimal efficiency can be achieved by acting on the reference flux. Based on this principle, several researches [90–101] have already been conducted aiming to force the induction motor drive to operate at optimal efficiency. Generally, the strategies that deal with efficiency optimization of induction motor drive can be grouped into simple control, model-based control, search control, hybrid method (combination of model-based control and search control).

The simple state control is the easiest strategy that is based on either slip frequency or power factor control because there are facts connected to optimal efficiency operation. At optimal efficiency operation of induction motor drive, it was observed in [86] that the power factor almost maintains a constant value. Like the power factor, it has been demonstrated in [95; 96; 99] that the slip can be determined only from motor parameters and is constant at optimal efficiency operation of induction motor drive. The implementation of this strategy is simple but its accuracy is limited to a narrow set of conditions. In addition, there could be parameter variation, which could cause a shift of optimal operating point. Model-based control adjusts the rotor flux based on optimal rotor flux calculated from a derived loss model of an induction motor drive. It is the fastest approach but analytical derivation of loss model might be very difficult and its accuracy is sensitive to parameter variation. The search control

looks the optimal operating point for a given output by simply changing stator current or rotor flux in steps. In the search process knowledge of motor or converter parameters is not required. However, this method slowly converges to the optimal operating point and has poor dynamic performance due to torque pulsations. The hybrid method takes the good characteristics of the model-based control and search control. Hence, it gives fast convergence to operating point with minimum power losses and shows good dynamic performance and no sensitivity to parameter changes [100].

When an induction motor drives a cyclic load, optimization problem formulation must fully involve the nature of the closed cycle operation. For such a problem, the possibility of obtaining optimal solution has been shown in [91; 101] using dynamic programming. In [91] a steady state loss minimization has also been extended to dynamic operation and results loss saving comparable to the optimal dynamic programming method.

### **3.4 Modeling Adjustable Speed Drive Based on Induction Motor**

For many applications driven by an induction motor, it is important to precisely control their torque, speed, and position in order to increase their energy efficiency or to meet users demand with respect to flexibility [92]. Most proposed control strategies for an IM can be conveniently realized using frequency converters, which are present in many different topologies. A PWM voltage source converter with diode front-end rectifier is the most widely applied topology in modern variable speed ac drives [93]. In this topology electric power occasionally drawn from induction motor fed by voltage source converter is wasted in braking resistor connected in series with an electronic switch. If the diode rectifier is replaced with PWM boost rectifier as shown in Fig.3.4, an ideal four quadrant operation becomes possible. In addition, with PWM rectifier, the dc bus voltage can be controlled, and the power quality can be improved. Most well-known global companies such as ABB, SIMENS, etc., employ this type of configuration. When

AC-DC-AC converter is used to drive an induction motor, the overall system will behave as a nonlinear load as seen by the AC supply line [102]. Therefore, the control objective includes current harmonic reduction in addition to achieving the required motor performance.

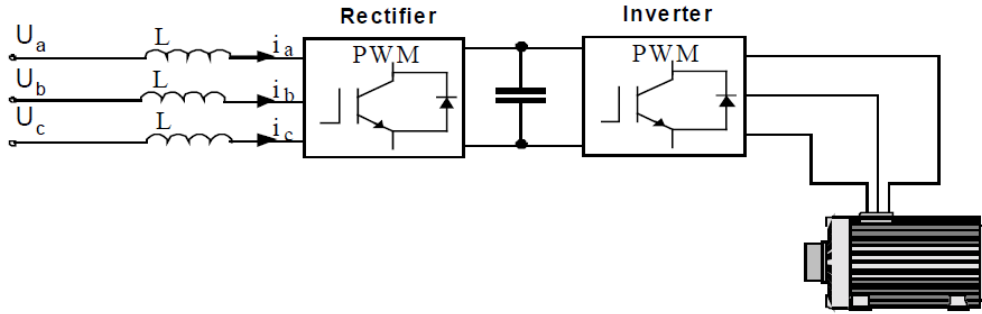


Fig. 3.4 — AC/DC/AC converter

### 3.4.1 Switching Network

The switching network shown in Fig. 3.5 is common in all basic converters. The state of the three upper switches can describe all the possible configurations of the switching network.

The operation of a switching network can be described by a model derived using the switching function. For the network shown in Fig. 3.5, a switching function can be defined as (3.8) where  $j = a, b, c$ .

$$S_j = \begin{cases} 1, & \text{if } sw_{jp} \text{ is closed} \\ 0, & \text{if } sw_{jp} \text{ is opened} \end{cases} \quad (3.8)$$

Using the switching function, the relation between the dc port current ( $i_{dc}$ ) and ac terminal current can be described by (3.9). Similarly, the relation between ac line voltage and dc voltage can be written by (3.10) where  $u_{dc}$  is the voltage across the dc terminals.

$$i_{dc} = S_a i_a + S_b i_b + S_c i_c \quad (3.9)$$

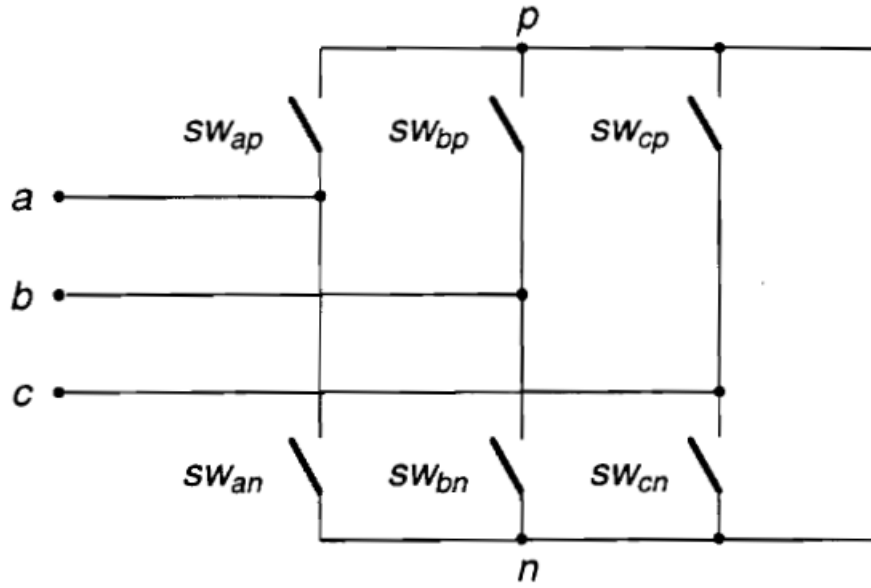


Fig. 3.5 — Switching network

$$\begin{aligned}
 u_{sab} &= (S_a - S_b)u_{dc} \\
 u_{sbc} &= (S_b - S_c)u_{dc} \\
 u_{sca} &= (S_c - S_a)u_{dc}
 \end{aligned} \tag{3.10}$$

The phase voltages at the input of the PWM rectifier can also be given by:

$$\begin{aligned}
 u_{sa} &= f_a u_{dc}, \\
 u_{sb} &= f_b u_{dc}, \\
 u_{sc} &= f_c u_{dc},
 \end{aligned} \tag{3.11}$$

where:

$$f_a = \frac{2S_a - (S_b + S_c)}{3}, f_b = \frac{2S_b - (S_a + S_c)}{3}, f_c = \frac{2S_c - (S_b + S_a)}{3}.$$

The same switching network model can be used to describe the boost rectifier and voltage source inverter (VSI).

### 3.4.2 PWM Boost Rectifier Modeling

Fig. 3.6a and b depict the basic diagram and single-phase representation of three phase boost converter respectively. The voltage equation for the circuit shown in Fig. 3.6b can be written as:

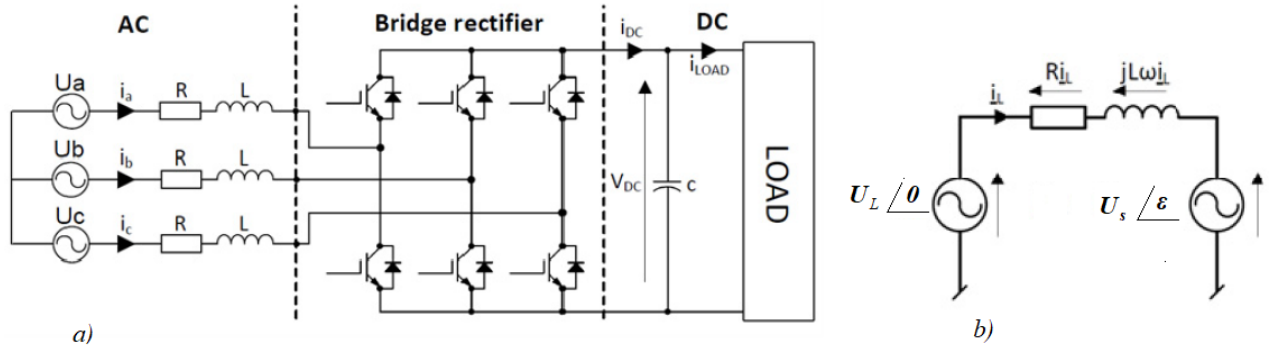


Fig. 3.6 — Rectifier schematics [103]

$$U_L = U_I + U_s, \quad (3.12)$$

where:  $U_I = RI_L + j\omega LI_L$ ,

$U_L$  – the source voltage,

$U_s$  – the bridge converter voltage controllable from the dc side,

$I_L$  – line current.

By controlling the amplitude and phase of the converter  $U_s$ , we can control the phase and amplitude of the line current. This effect can be seen in Fig. 3.7, where the phasor diagram for: rectifier operation at a power factor less than unity (a), rectifier operation at unity power factor (b), and inverter operation at unity power factor (c) are shown.

The mesh equation in the ac side of the boost rectifier can be written by:

$$u_j = Ri_j + L \frac{di_j}{dt} + u_{sj}, \quad (3.13)$$

where:  $j = a, b, c$ .

In the dc side of the boost rectifier, the Kirchhoff's current law can be written:

$$C \frac{du_{dc}}{dt} = S_a i_a + S_b i_b + S_c i_c - i_{load}, \quad (3.14)$$

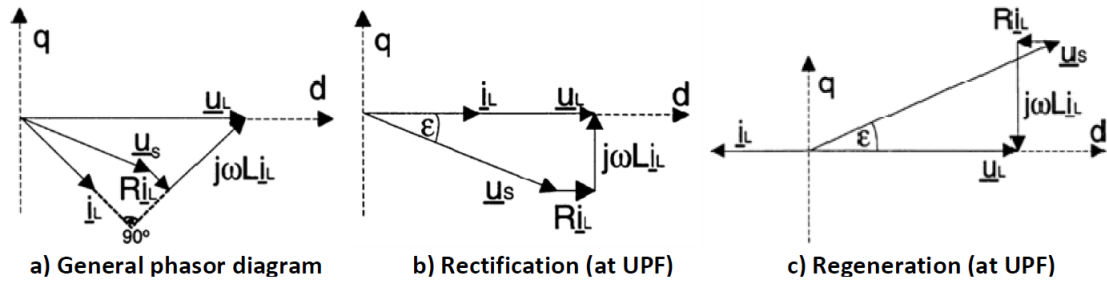


Fig. 3.7 — Phasor diagram

where:  $i_{load}$  – the load current.

Equations (3.13) and (3.14) describe the model of three phase boost converter. The active and reactive power supplied by the source to the boost converter can be expressed as in (3.15).

$$\begin{aligned} p &= u_a i_a + u_b i_b + u_c i_c \\ q &= \frac{1}{\sqrt{3}}(u_{bc} i_a + u_{ca} i_b + u_{ab} i_c) \end{aligned} \quad (3.15)$$

Let the phase voltage and the fundamental line current be defined as:

$$\begin{aligned} u_a &= E_m \cos \omega_s t \\ u_b &= E_m \cos\left(\omega_s t + \frac{2\pi}{3}\right) , \\ u_c &= E_m \cos\left(\omega_s t - \frac{2\pi}{3}\right) \end{aligned} \quad (3.16)$$

$$\begin{aligned} i_a &= I_m \cos(\omega_s t + \varphi) \\ i_b &= I_m \cos\left(\omega_s t + \frac{2\pi}{3} + \varphi\right) , \\ i_c &= I_m \cos\left(\omega_s t - \frac{2\pi}{3} + \varphi\right) \end{aligned} \quad (3.17)$$

where:  $E_m$  – the amplitude of the phase voltage,

$I_m$  – the amplitude of the line current,

$\omega_s$  – the angular frequency,

$\varphi$  – the phase shift,

then, the model of three phase boost rectifier in synchronous reference frame can be described by (3.18) and (3.19).

$$\begin{aligned} u_d &= R i_d + L \frac{di_d}{dt} - \omega_s L i_q + u_{sd} \\ u_q &= R i_q + L \frac{di_q}{dt} + \omega_s L i_d + u_{sq} \end{aligned} \quad (3.18)$$

$$C \frac{u_{dc}}{dt} = \frac{3}{2} (S_d i_d + S_q i_q) - i_{load} \quad (3.19)$$

Thus, the active and reactive power supplied by the source to this converter in synchronous reference frame can be expressed as in (3.20).

$$\begin{aligned} p &= u_{Ld} i_{Ld} + u_{Lq} i_{Lq} \\ q &= u_{Lq} i_{Ld} - u_{Ld} i_{Lq} \end{aligned} \quad (3.20)$$

### 3.4.3 Control Strategies for Boost Rectifier

The control strategies for PWM rectifier are classified based on their principle as shown in Fig. 3.8. However, the most used control strategies for PWM boost rectifier are voltage-oriented control (VOC) and Direct power control (DPC). VOC employs current control loop, which influence its configuration and performance whereas DPC is without current control loop and PWM modulator because the converter switching states are selected by switching table based on instantaneous error between commanded and estimated values of active and reactive power [93].

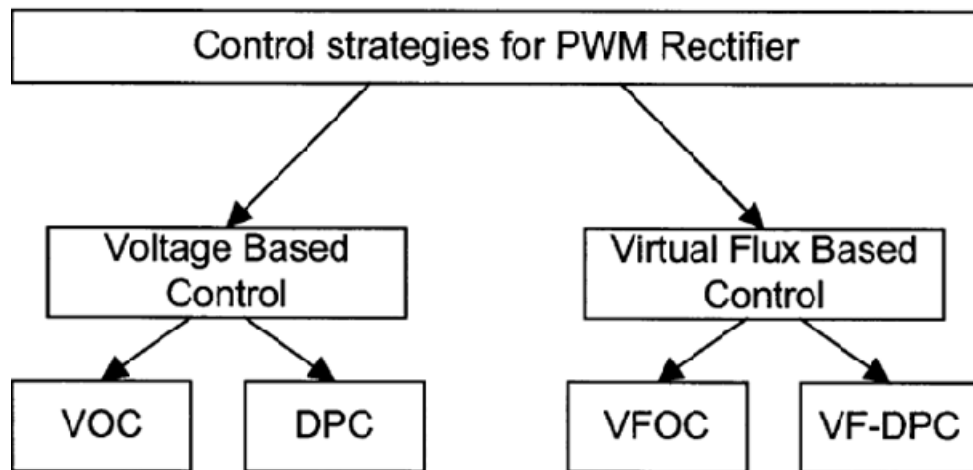


Fig. 3.8 — Classification of control methods for PWM rectifier [93]

The control scheme for voltage-oriented control is shown in Fig. 3.9. It involves transformation of three phase measured current and voltage into dq-coordinate system.

The controller uses the line currents in the dq coordinates and dc link voltage to generate reference voltage to the PWM block.

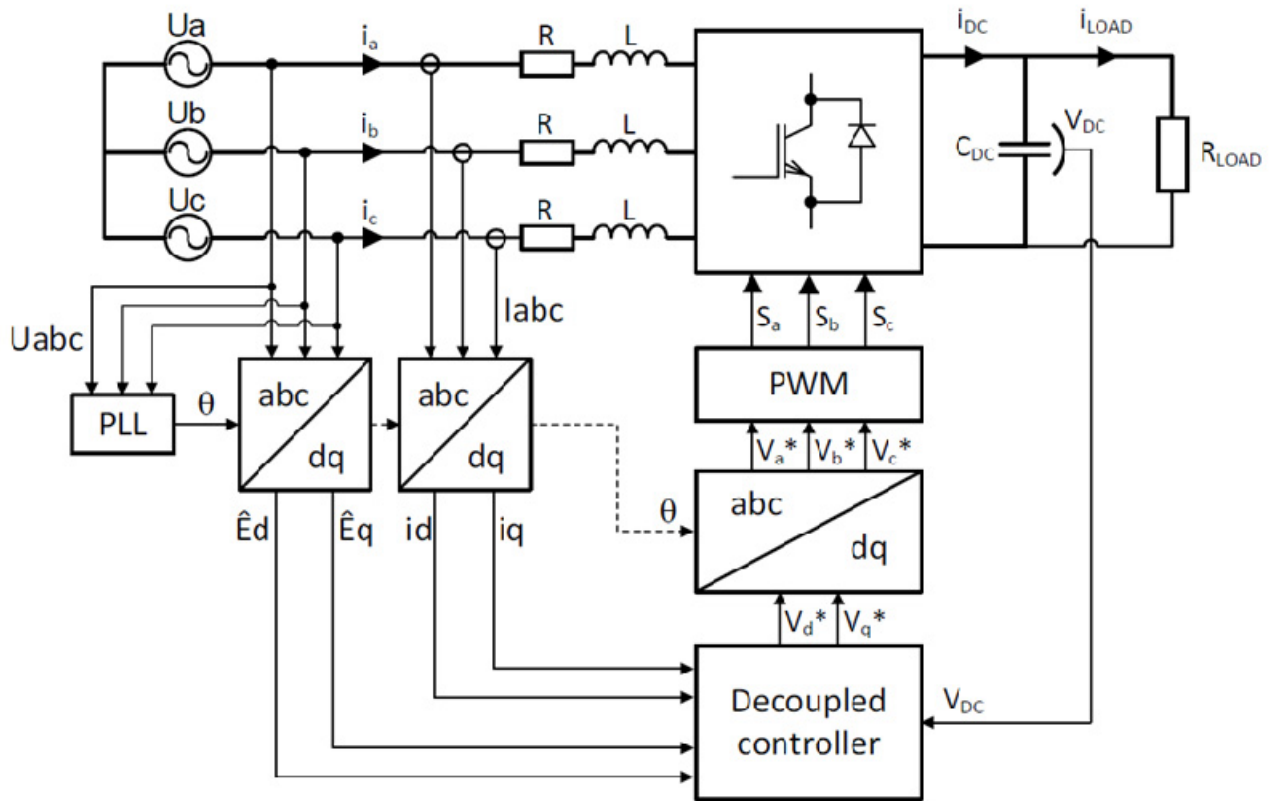


Fig. 3.9 — Schematic of VOC [104]

If the d-axis of the rotating reference frame chosen is aligned with the line voltage vector, the active and reactive power can be controlled independently. The q-axis current controls the reactive power and the d-axis current controls the active power. Equations (3.18) can be written as in (3.21).

$$\begin{aligned} E_m &= u_d = Ri_d + L \frac{di_d}{dt} - \omega_s Li_q + u_{sd} \\ 0 &= u_q = Ri_q + L \frac{di_q}{dt} + \omega_s Li_d + u_{sq} \end{aligned} \quad (3.21)$$

For unity power factor control, the q-axis current is set to zero and the dc link voltage controller sets the reference d-axis current. Fig. 3.10 shows decoupled current control of PWM rectifier for unity power factor control.

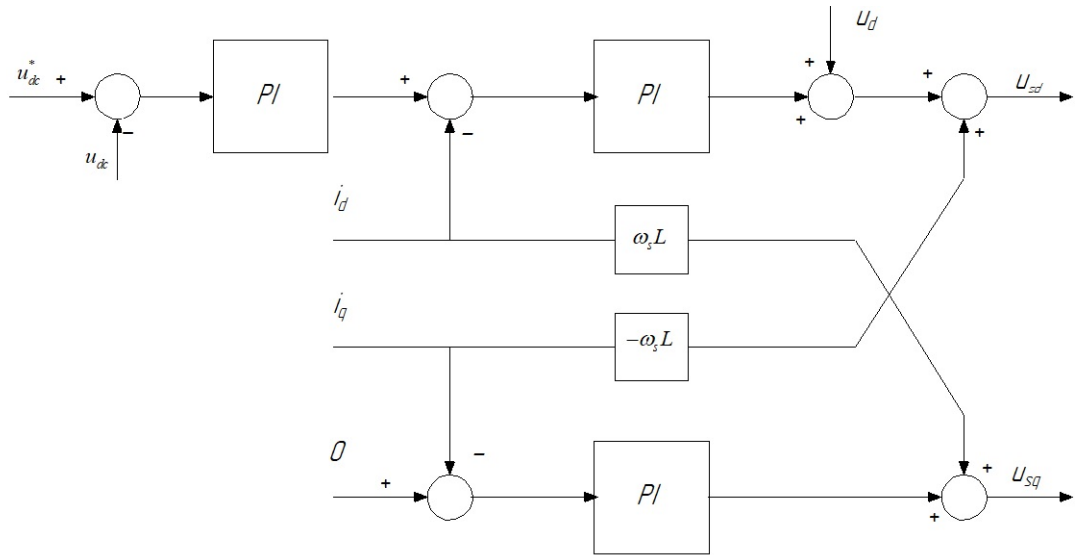


Fig. 3.10 — Decoupled controller

### 3.4.4 Modeling Voltage Source Inverter Fed Induction Motor

For a voltage source inverter, the phase voltages ( $u_{sa}, u_{sb}, u_{sc}$ ) at the terminals of the induction motor are determined from the dc voltage. In 3 phase AC machines, electromagnetic process can be clearly described with the help of equivalent circuits. Induction motor model developed in a two phase reference frame is the most convenient representation with which equivalent circuit can be constructed. The stator mesh, rotor mesh, and flux linkage equations in an arbitrary two-phase reference frame for squirrel cage type can be written:

$$\begin{aligned} \mathbf{u}_s &= R_s \mathbf{i}_s + \frac{d\psi_s}{dt} + \omega_s \mathbf{B} \psi_s, \\ \mathbf{0} &= R_r \mathbf{i}_r + \frac{d\psi_r}{dt} + (\omega_s - \omega) \mathbf{B} \psi_r, \end{aligned} \quad (3.22)$$

$$\begin{aligned} \psi_s &= L_s \mathbf{i}_s + L_m \mathbf{i}_r, \\ \psi_r &= L_m \mathbf{i}_s + L_r \mathbf{i}_r, \end{aligned} \quad (3.23)$$

where:  $R_s$  is stator resistance,  $R_r$  is rotor resistance,  $L_s$  is stator inductance,  $L_r$  is rotor inductance,  $L_m$  is mutual inductance,  $\omega$  is rotor angular speed,  $\omega_s$  is the angular speed of the right angled coordinate system,  $\psi_s$  is stator flux,  $\psi_r$  is rotor flux,  $\mathbf{u}_s = [u_{sd} \ u_{sq}]^T$ ,  $\mathbf{i}_s = [i_{sd} \ i_{sq}]^T$ ,  $\psi_s = [\psi_{sd} \ \psi_{sq}]^T$ ,  $\mathbf{i}_r = [i_{rd} \ i_{rq}]^T$ ,  $\psi_r = [\psi_{rd} \ \psi_{rq}]^T$ ,  $\mathbf{B} = \begin{bmatrix} 0 & -1 \\ 1 & 0 \end{bmatrix}$ .

By introducing the linkage inductances, magnetizing current, and magnetizing flux defined by the following expressions:

$$L_{s\sigma} = L_s - L_m, \quad (3.24)$$

$$L_{r\sigma} = L_r - L_m,$$

$$\mathbf{i}_\mu = \mathbf{i}_s + \mathbf{i}_r, \quad (3.25)$$

$$\psi_\mu = L_m \mathbf{i}_\mu, \quad (3.26)$$

where:  $\mathbf{i}_\mu = [i_{\mu d} \ i_{\mu q}]^T$ ,  $\psi_\mu = [\psi_{\mu d} \ \psi_{\mu q}]^T$ ;

the stator and rotor flux linkage can be rewritten as in (3.27).

$$\psi_s = L_{s\sigma} \mathbf{i}_s + \psi_\mu \quad (3.27)$$

$$\psi_r = L_{r\sigma} \mathbf{i}_r + \psi_\mu$$

The above definitions give another alternative form of stator and rotor mesh equations as given by in (3.28).

$$\begin{aligned} \mathbf{u}_s &= R_s \mathbf{i}_s + \frac{d(L_{s\sigma} \mathbf{i}_s)}{dt} + \frac{d\psi_\mu}{dt} + \omega_s L_{s\sigma} \mathbf{B} \mathbf{i}_s + \omega_s \mathbf{B} \psi_\mu \\ 0 &= R_r \mathbf{i}_r + \frac{d(L_{r\sigma} \mathbf{i}_r)}{dt} + \frac{d\psi_\mu}{dt} + \omega_s L_{r\sigma} \mathbf{B} \mathbf{i}_r + \omega_s \mathbf{B} \psi_\mu - \omega \mathbf{B} \psi_r \end{aligned} \quad (3.28)$$

From (3.28), the T equivalent circuit of an induction machine in an arbitrary reference frame as shown in Fig. 3.11 is derived. The T equivalent circuit is the basic and most realistic representation for analysis of the steady state conditions. In the T equivalent circuit, stator and rotor leakage inductances represent the magnetic flux leakage. However, these partial leakages are not completely identifiable by measuring stator quantities. Therefore, it is advisable to use equivalent circuit with reduced parameters.

If a new cross current  $i_m$  is introduced as defined by:

$$\mathbf{i}_m = \frac{\psi_r}{L_m} = \mathbf{i}_s + \frac{L_r}{L_m} \mathbf{i}_r, \quad (3.29)$$

where:  $\mathbf{i}_m = [i_{m d} \ i_{m q}]^T$ ; then the stator mesh and rotor mesh can be again rewritten as in (3.30) where  $\sigma = 1 - \frac{L_m^2}{L_s L_r}$ .

$$\begin{aligned} \mathbf{u}_s &= R_s \mathbf{i}_s + \sigma L_s \frac{d\mathbf{i}_s}{dt} + \omega_s \sigma L_s \mathbf{B} \mathbf{i}_s + (1 - \sigma) L_s \frac{d\mathbf{i}_m}{dt} + \omega_s (1 - \sigma) L_s \mathbf{B} \mathbf{i}_s \\ 0 &= \left(\frac{L_m}{L_r}\right)^2 R_r \left(\frac{L_r}{L_m} \mathbf{i}_r\right) + (1 - \sigma) L_s \frac{d\mathbf{i}_m}{dt} + (\omega_s - \omega) (1 - \sigma) L_s \mathbf{B} \mathbf{i}_m \end{aligned} \quad (3.30)$$

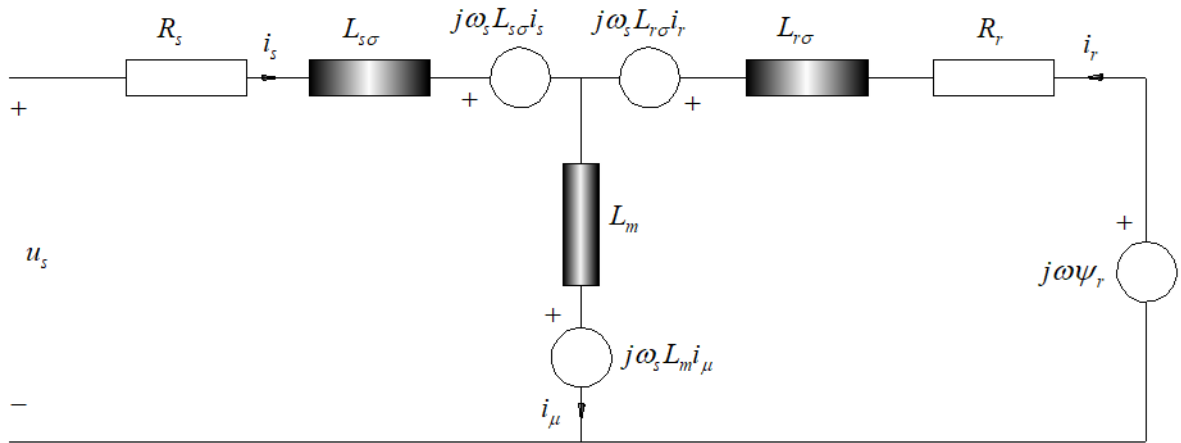
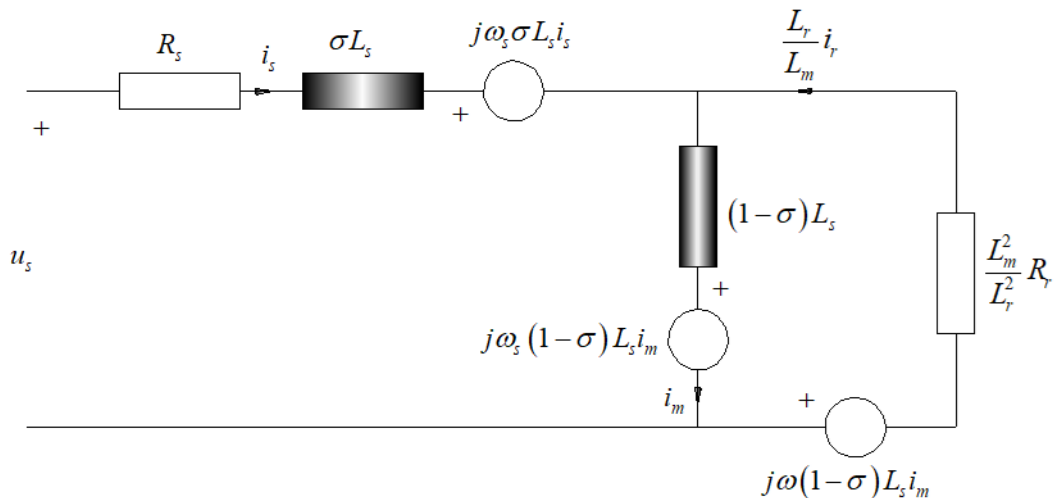


Fig. 3.11 — T equivalent circuit

From the above mesh equations, the inverse  $\Gamma$  equivalent circuit (Fig. 3.12), which is commonly used during design of controllers, is derived. The inverse  $\Gamma$  equivalent circuit contains four parameters with the total leakage inductance in the stator mesh and all the parameters that describe the model of induction motor can be determined by standard tests.

Fig. 3.12 — Inverse  $\Gamma$  equivalent circuit

Besides the steady state condition, it is essential to examine the induction motor performance at different conditions. The objective is to adapt a dynamic model which can simulate the real motor performance as close as possible. A dynamic model contains a set of equations for describing the relationship between electrical, magnetic, and mechanical quantities. In the past, many papers have been published that represent the dynamic model of induction motor. However, not all developed models consider all the existing phenomena. The classical dynamic model [77; 105] is based on a rough

approximation. It assumes the machine parameters: stator inductance, stator resistance, rotor inductance and rotor resistance, as constant and independent of the state. This model is simple and has yielded good engineering results for both steady state and most transient states. However, when changes in flux level or inrush current occur which could be encountered in situations like online starting or in flux weakening operating conditions, they don't give full satisfaction [106].

In practice, the flux linkage produced due to currents flowing in the stator and rotor circuits could use magnetic paths such as the end winding leakage paths, cores, the slot leakage paths, the stator and rotor teeth and the airgap. The inductance representing the stator and rotor cores, magnetizing branch (stator and rotor teeth) are saturable. In the presence of magnetic saturation, the relation between the magnetizing current and amplitude of main flux becomes non-linear. A saturation model as shown in Fig. 3.13 developed in [107] significantly improved the accuracy of prediction during transient conditions. However, the difficulties faced in determining machine parameters limit its use. Since the stator and rotor flux linkages are small compared to main flux linkage, an acceptable result for many applications can be obtained if the effect of saturation can be included in the rotor mesh. With this assumption, the rotor mesh can be rewritten as:

$$0 = R_r(\mathbf{i}_m - \mathbf{i}_s) + \frac{d(L_s \mathbf{i}_m)}{dt} + (\omega_s - \omega)L_s \mathbf{B} \mathbf{i}_m. \quad (3.31)$$

After breakdown the derivative, the rotor mesh reduces to (3.32) where  $L_m = \psi_\mu / i_\mu$

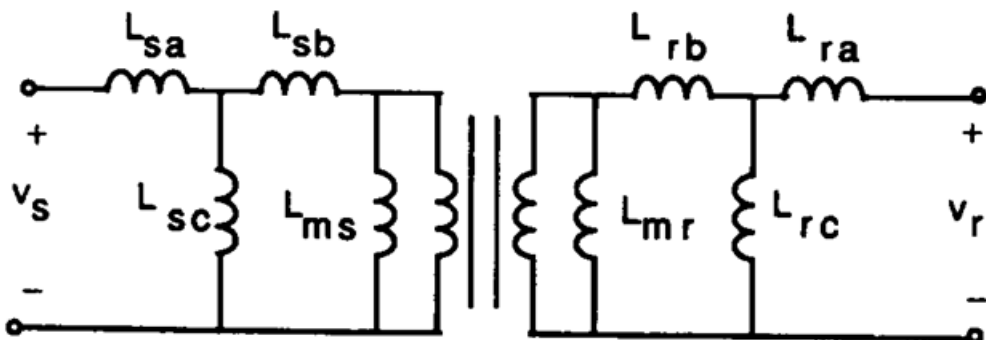


Fig. 3.13 — Equivalent circuit of IM [107]

and  $L'_m = d\psi_\mu/di_\mu$ .

$$0 = \mathbf{i}_m - \mathbf{i}_s + \frac{L'_m + L_\sigma}{R_r} \frac{d\mathbf{i}_m}{dt} + (\omega_s - \omega) \frac{L_m + L_\sigma}{R_r} \mathbf{B}\mathbf{i}_m \quad (3.32)$$

Similarly, the stator mesh can be expressed by:

$$\begin{aligned} \mathbf{u}_s = & R_s \mathbf{i}_s + \sigma L_s \frac{d\mathbf{i}_s}{dt} + \omega_s \sigma L_s \mathbf{B}\mathbf{i}_s + (1 - \sigma)(L'_m + L_\sigma) \frac{d\mathbf{i}_m}{dt} \\ & + \omega_s (1 - \sigma)(L_m + L_\sigma) \mathbf{B}\mathbf{i}_m, \end{aligned} \quad (3.33)$$

then

$$|i_\mu| = \sqrt{\left(\frac{L_r \sigma}{L_r} i_{sd} + \frac{L_m}{L_r} i_{md}\right)^2 + \left(\frac{L_r \sigma}{L_r} i_{sq}\right)^2}. \quad (3.34)$$

Electrical machines are made of high permeable ferromagnetic material, which helps to increase the machines' efficiency. However, the time and space variation of the magnetic flux induces iron losses [108], which have a considerable effect on accuracy of the model used. For a time-dependent applied magnetic field, the total iron loss comprises hysteresis, classical eddy current loss and excess losses [109].

Assuming sinusoidal flux pattern is given by:

$$\psi(t) = dB_p \sin(2\pi ft), \quad (3.35)$$

where:  $d$ – thickness of the sheet,

$B_p$ – peak value of flux density,

$f$  – the frequency;

the total iron loss is calculated as reported in [109] by:

$$P_{fe} = K_H B_p^\alpha f + K_E B_p^2 f^2 + K_{ex} B_p f (\sqrt{1 + e B_p f} - 1), \quad (3.36)$$

where:  $\alpha$ ,  $K_H$ ,  $K_E$ ,  $K_{ex}$ , and  $e$  are material related parameters fitted based on the loss measurements under sinusoidal flux condition.

The effect of iron loss can be represented by an equivalent resistance. However, since the iron loss expressed by (3.36) is a function of magnetic field and frequency, a fixed equivalent resistor cannot represent the effect of iron loss in the dynamic model. The equivalent resistor could be placed in series or in parallel to the magnetizing

inductance. In both approaches, the no load test and locked rotor test can be used to determine the value of the equivalent resistance. Fig. 3.14 represents the steady state model of an induction motor including core loss with the leakage inductance in the stator mesh. Using Kirchhoff's voltage and current laws, the following equations can be written:

$$\mathbf{u}_s = R_s \mathbf{i}_s + \sigma L_s \frac{d\mathbf{i}_s}{dt} + \omega_s \sigma L_s \mathbf{B} \mathbf{i}_s + (1 - \sigma) L_s \frac{d\mathbf{i}_m}{dt} + \omega (1 - \sigma) L_s \mathbf{B} \mathbf{i}_m, \quad (3.37)$$

$$\begin{aligned} \mathbf{i}_s = & \mathbf{i}_m + (1 - \sigma) L_s \left( \frac{1}{R_f} + \frac{T_r}{(1 - \sigma) L_s} \right) \frac{d\mathbf{i}_m}{dt} + \\ & (1 - \sigma) L_s \left( \frac{\omega_s}{R_f} + \frac{(\omega_s - \omega) T_r}{(1 - \sigma) L_s} \right) \mathbf{B} \mathbf{i}_m, \end{aligned} \quad (3.38)$$

$$R_f i_f = (1 - \sigma) L_s \frac{d\mathbf{i}_m}{dt} + (1 - \sigma) L_s \omega_s \mathbf{B} \mathbf{i}_m. \quad (3.39)$$

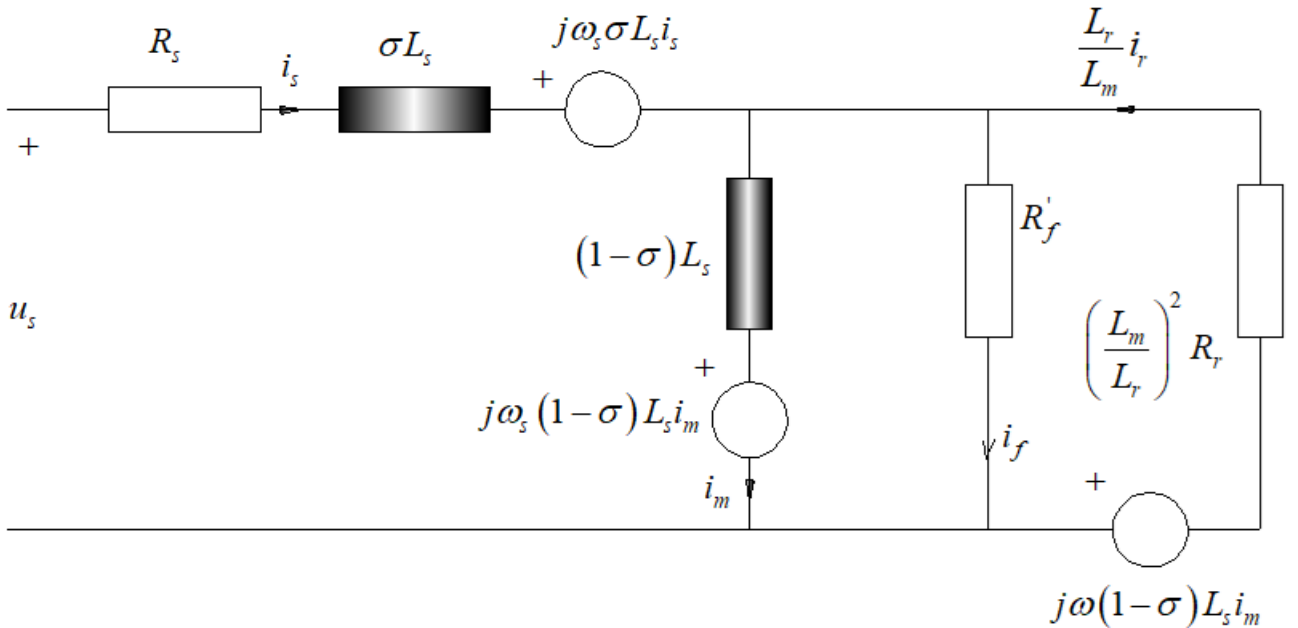


Fig. 3.14 — Equivalent circuit of IM including core loss

From equations (3.37)-(3.39), the model of an induction motor including iron loss in state space form can be expressed as:

$$\begin{aligned} \frac{d\mathbf{i}_s}{dt} &= -\frac{1}{T_\sigma} \mathbf{i}_s - \omega_s \mathbf{B} \mathbf{i}_s + c_{fe} \mathbf{i}_m - c_{fe} T_r \omega \mathbf{B} \mathbf{i}_m + \frac{\mathbf{u}_s}{\sigma L_s}, \\ \frac{d\mathbf{i}_m}{dt} &= -\frac{1}{T_{rfe}} \mathbf{i}_m + \frac{1}{T_{rfe}} \mathbf{i}_s - \left( \omega_s - \frac{T_r}{T_{rfe}} \omega \right) \mathbf{B} \mathbf{i}_m, \\ \frac{d\omega}{dt} &= \frac{z_p}{J} (M_e - M_L), \\ M_e &= 1.5 z_p (1 - \sigma) L_s (i_{md} i'_{rq} - i_{mq} i'_{rq}), \end{aligned} \quad (3.40)$$

where:  $M_L$ ,  $z_p$ , and  $J$  are load torque, pair of poles and equivalent moment of inertia respectively and the rest of the terms are defined as follows:

$$T_r = \frac{L_r}{R_r}, T_{rfe} = T_r + \frac{(1-\sigma)L_s}{R_{fe}}, \frac{1}{T_\sigma} = \frac{R_s}{\sigma L_s} + \frac{1-\sigma}{\sigma T_{rfe}}, c_{fe} = \frac{1-\sigma}{\sigma T_{rfe}}, i_r' = \frac{L_r}{L_m} i_r.$$

### 3.5 Loss Model and Optimal Magnetizing Current Generation

#### 3.5.1 Derivation of Loss Equation

Converter losses has little influence on the drive loss and can be neglected when designing a control algorithm [86]. Therefore, the minimization criterion can only consider motor loss. The main constituents of motor losses are stator copper loss, rotor copper loss, iron losses and mechanical losses. Mechanical losses are independent of the stator current, but they depend on the speed.

The expression for stator copper losses is given by:

$$P_{cus} = R_s(i_{sd}^2 + i_{sq}^2), \quad (3.41)$$

the expression for rotor copper losses is written as:

$$P_{cur} = R_r(i_{rd}^2 + i_{rq}^2), \quad (3.42)$$

and the expression for iron losses is given by:

$$P_{fe} = R_{fe}(i_{fd}^2 + i_{fq}^2). \quad (3.43)$$

Thus, the total losses will be:

$$P_{loss} = P_{cus} + P_{cur} + P_{fe}. \quad (3.44)$$

### 3.5.2 Optimal Magnetizing Current Generation in Steady State

Thanks to vector control, induction motor can have DC machine like performance. The stator voltage space vector can be oriented with respect to space vector of either rotor flux, airgap flux or stator flux. Applying rotor-flux-oriented constraints, we get:

$$\begin{aligned}\psi_{rq} &= (1 - \sigma)L_s i_{mq} = 0, \\ i_{sd} &= i_{md} + T_{rfe} \frac{di_{md}}{dt}, \\ \omega_{sl} &= \frac{1}{T_{rfe}} \left( \frac{i_{sq}}{i_{md}} - (T_{rfe} - T_r)\omega \right), \\ M_e &= K_t i_{sd} i_{sq},\end{aligned}\tag{3.45}$$

where:  $K_t = 1.5z_p(1 - \sigma)L_s$ .

In steady state:  $i_{mq} = 0$ ,  $i'_{rd} = 0$ ,  $i_{fd} = 0$ ,  $i_{sd} = i_{md}$ ,  $i_{fe} = i_{fq}$ ,  $i'_r = i'_{rq}$ ,  $i_{sq} = i'_r + i_{fe}$ , and applying KVL to the rotor circuit,  $i'_r$  can be written as:

$$i'_r = \frac{R_f}{R_f + R'_r} i_{sq} - \omega \frac{(1 - \sigma)L_s}{R_f + R'_r} i_{sd}.\tag{3.46}$$

Therefore, the total power loss can be written as:

$$P_{loss} = R_d i_{sd}^2 + R_q i_{sq}^2,\tag{3.47}$$

where:  $R_d = R_s + \frac{(1-\sigma)^2 L_s^2}{R_f + R'_r} \omega^2$ ,  $R_q = R_s + \frac{R_f R'_r}{R_f + R'_r}$ ,  $R'_r = \left(\frac{L_m}{L_r}\right)^2 R_r$ .

Obviously, both direct and quadrature components of the controlled current have effect on the total power loss. So, for a given torque producing current ( $i_{sq}$ ), there exists an optimal flux producing current ( $i_{sd}$ ) which minimizes the electric motor losses.

The power loss can also be given in terms of operating condition:

$$P_{loss} = R_d i_{sd}^2 + R_q \frac{M_e^2}{K_t^2 i_{sd}^2}.\tag{3.48}$$

For constant torque, the optimal flux producing current ( $i_{sd}$ ) or optimal magnetizing current can be calculated as follows:

$$i_{md}^{opt} = i_{sd}^{opt} = \left(\frac{\gamma}{\alpha}\right)^{0.25},\tag{3.49}$$

where:  $\gamma = R_q \frac{M_e^2}{K_t^2}$ ,  $\alpha = R_d$ .

Then, optimal rotor flux can be determined by:

$$\psi_r^{opt} = L_m i_{sd}^{opt}. \quad (3.50)$$

The optimal rotor flux is a function of speed and torque. Using (3.50) for each possible torque-speed operating point, the optimal rotor flux can be computed. The result of the calculation is shown in Fig. 3.15. In the calculation only one active constraint (torque) is considered. However, in practice there are voltage and current constraints which reduce the range of values to be searched.

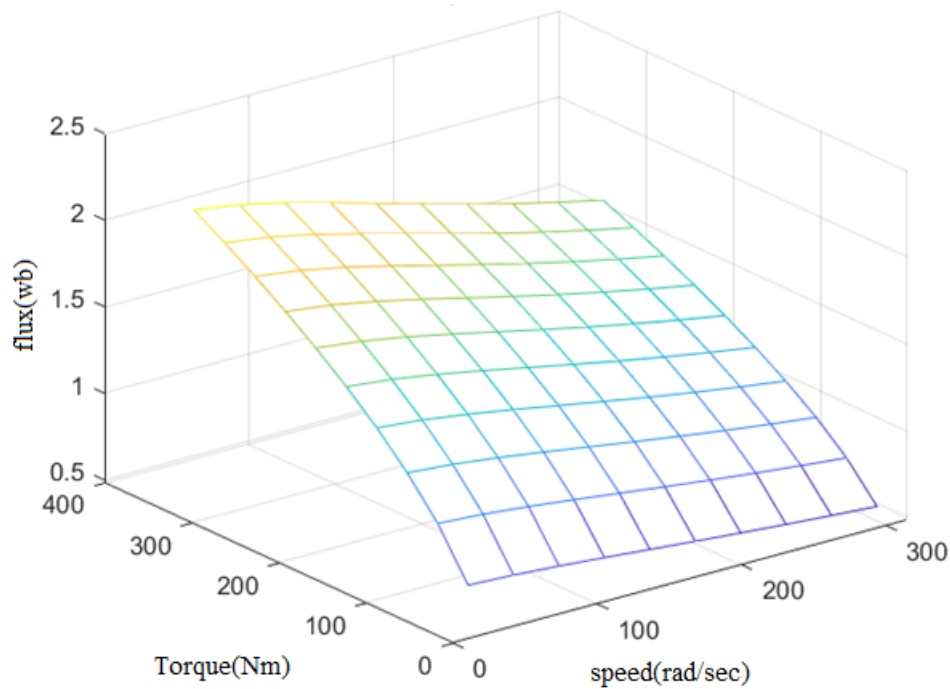


Fig. 3.15 — Optimal flux vs torque speed

### 3.5.3 Optimal Magnetizing Current Generation under Voltage and Current Constraints

The problem of efficiency optimized control of induction motor drive aims to minimize energy consumption under voltage and current constraints. To avoid magnetic

saturation, the rotor flux is further limited to its rated value. Furthermore, to maintain controllability and limit peak currents, the rotor flux is not reduced below an arbitrarily minimum level. Therefore, no optimization can be recommended in the region shaded by red in Fig. 3.16. Consequently, the reference flux is set equal to rated value. As shown in Fig. 3.16 the rotor flux can be optimized for torque load less than 149Nm at base speed and less than 40 at 10% of base speed.

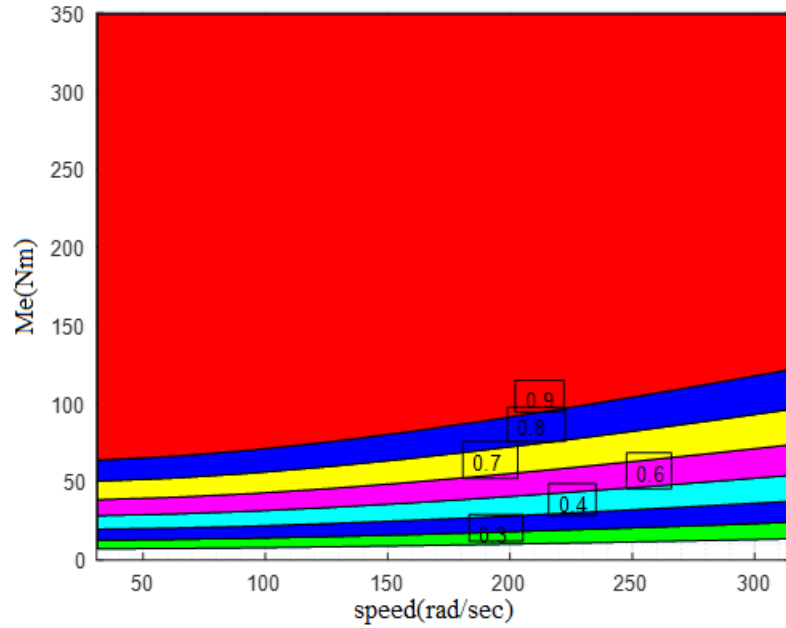


Fig. 3.16 — Optimal rotor flux

In steady state for field-oriented coordinate system, the stator voltage equations can be written as in (3.51).

$$\begin{aligned} v_{sd} &= R_s i_{sd} - \omega_s \sigma L_s i_{sq} \\ v_{sq} &= R_s i_{sq} + \omega_s \sigma L_s i_{sd} + \omega_s (1 - \sigma) L_s i_{md} \end{aligned} \quad (3.51)$$

If the voltage drop due to stator resistance is neglected, the voltage constraint can be stated as:

$$(\omega_s \sigma L_s i_{sq})^2 + (\omega_s L_s i_{sd})^2 \leq v_{max}^2. \quad (3.52)$$

Including the constraints mentioned above, the objective function can be formulated as:

$$\min\{P_{loss}(i_{sd}, i_{sq})\}, \quad (3.53)$$

subject to:  $M_e = K_t i_{sd} i_{sq}$ ,

$$i_{sd}^2 + i_{sq}^2 - I_{max}^2 \leq 0,$$

$$i_{sd} \leq i_{sdn},$$

$$i_{sd} \geq i_{sdmin},$$

$$0 \leq v_{sd}^2 + v_{sq}^2 \leq v_{max}^2,$$

where:  $i_{sdmin}$ — minimum flux producing current,

$i_{sdn}$ — rated flux producing current,

$i_{max}$ — maximum stator current,

$v_{max}$ — maximum voltage.

In the basic speed range, the voltage limitation is not effective. Fig. 3.17 shows the relation between the optimal flux producing current and torque producing current in the basic speed range. If the optimal flux producing current calculated under only torque constraint is less than  $i_{sdn}$ , the following relation holds between torque and optimal flux producing currents:

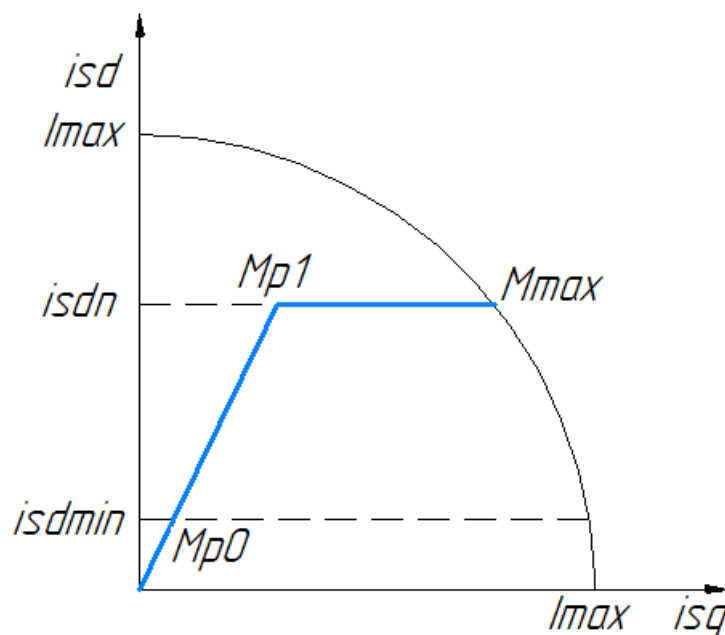


Fig. 3.17 — Relation between optimal flux and torque producing currents in base speed range

$$i_{sq} = \left( \frac{R_d}{R_q} \right)^{0.5} i_{sd}. \quad (3.54)$$

The lower limit of flux producing current defines the torque  $M_{p0}$ :

$$M_{p0} = K_t \left( \frac{R_d}{R_q} \right)^{0.5} i_{sdmin}^2. \quad (3.55)$$

The upper limit of the flux producing current defines the torque  $M_{p1}$  given by (3.56), above which no reduction of rotor flux can be proposed.

$$M_{p1} = K_t \left( \frac{R_d}{R_q} \right)^{0.5} i_{sdn}^2 \quad (3.56)$$

The maximum torque ( $M_{max}$ ) is determined using the maximum flux producing current and maximum stator current as:

$$M_{max} = K_t i_{sdn} (I_{max}^2 - i_{sdn}^2)^{0.5}. \quad (3.57)$$

For a load torque greater than  $M_{p1}$  and less than the maximum torque ( $M_{max}$ ), the following relation holds:

$$i_{sd} = i_{sdn}; \quad \left( \frac{R_d}{R_q} \right)^{0.5} i_{sdn} \leq i_{sq} \leq (I_{max}^2 - i_{sdn}^2)^{0.5}. \quad (3.58)$$

### 3.5.4 Optimal Magnetizing Current Generation for Sucker Rod Pump Applications

Since induction motor driving sucker rod pump operates under cyclic load, the objective of efficiency optimal control strategy must deal to minimize the total energy loss in a cycle under given constraints. Consequently, the objective function in (3.53) is replaced by:

$$\min \left\{ \int_0^T P_{loss}(i_{sd}, i_{sq}) dt \right\}, \quad (3.59)$$

where:  $T$ – time taken for one cycle of pump operation.

The objective function in (3.59) can be satisfied by searching an optimal magnetizing current trajectory for given torque and speed trajectories. In the search

process, the energy loss for one cycle of pump operation is examined for all possible magnetizing current trajectories. This process can take considerable time. Thus, in offline, for a given torque and speed trajectories, energy losses are calculated for all possible magnetizing current trajectories. Then, the optimal trajectory corresponding to minimum energy loss for one operational cycle can be stored and uploaded to the controller. Since, for a given sucker rod pump installations, operating condition change slowly and the rotor speed is regulated and can be assumed to remain constant, a new search for optimal magnetizing current trajectory can be activated when change in torque trajectory occurs.

It is known that if the magnetizing current is reduced for the parts of the cycle where the sucker rod pump drive is lightly loaded, some energy can be saved. In rotor flux oriented reference frame, the optimal magnetizing current trajectory is the same as the flux producing current trajectory. A flux producing current trajectory can be defined based on steady state electromagnetic torque ( $M_p$ ).  $M_p$  is selected based on the absolute value of a given load torque trajectory as shown Fig. 3.18. It has to be in the range  $M_{p0} \leq M_p \leq M_{p1}$ . For parts of trajectory on the given load torque above  $M_p$ , the flux producing current is set to  $i_{sdn}$ , otherwise to the optimal value corresponding to  $M_p$ . For each defined flux producing current trajectory, the torque producing current trajectory and the energy loss are calculated for one cycle of pump operation. The results of energy loss for all possible steady state electromagnetic torques are examined and the optimal flux producing current trajectory is selected. The minimum time interval for constant flux operation, which depends on the existing delay in the forming of rotor flux, is considered when selecting steady state electromagnetic torque. A simple numerical algorithm to find optimal magnetizing current trajectory can be outlined as follows:

- calculate the steady state electromagnetic torque corresponding to lower limit of optimal flux producing current ( $M_{p0}$ ) and upper limit of the optimal flux producing current ( $M_{p1}$ );
- list constant torque ( $M_p$ ) operations in the range  $M_{p0} \leq M_p \leq M_{p1}$ .

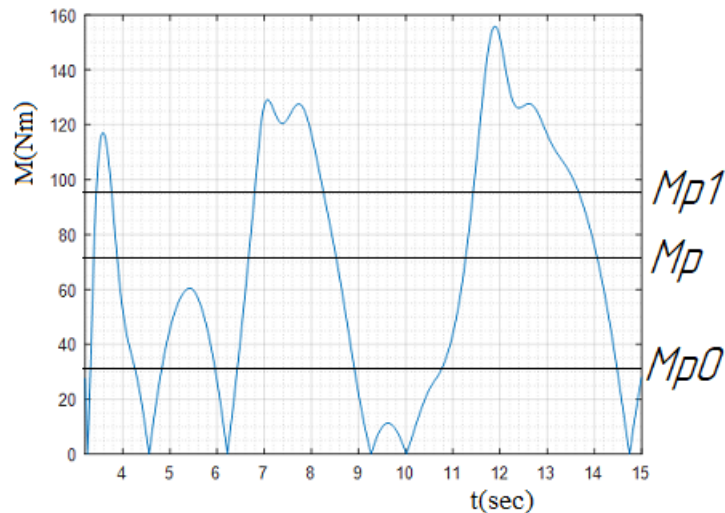


Fig. 3.18 — Absolute value of given load torque trajectory.

- select the steady state electromagnetic torques ( $M_p$ ) which divides the absolute value of the torque trajectory into time intervals greater than the minimum time interval for constant flux operation;
- for each selected steady state electromagnetic torque, define flux producing current trajectory;
- for each defined flux producing current, calculate the energy loss for one complete cycle of operation;
- the flux producing current trajectory with minimum energy loss is selected as an optimal magnetizing current trajectory.

Operation at optimal efficiency of induction motor drive can be achieved with the help of control system. Fig. 3.19 shows block diagram for closed loop vector control scheme proposed for sucker rod pump drive. The established control system can help to operate the sucker rod pump based on the optimal magnetizing current trajectory. In steady state, the speed regulator helps the measured speed to follow reference speed. The block PC LMA uses speed and torque trajectories and based on the above loss minimization strategy, it calculates and stores optimal magnetizing current trajectory until the torque trajectory shows change. This block provides the stored optimal magnetizing current trajectory as a reference. If the torque trajectory shows some change, a new optimal magnetizing current trajectory is calculated to consider the effect of the changes.  $T_\varphi$  is the time constant of a low pass filter. It presents a certain

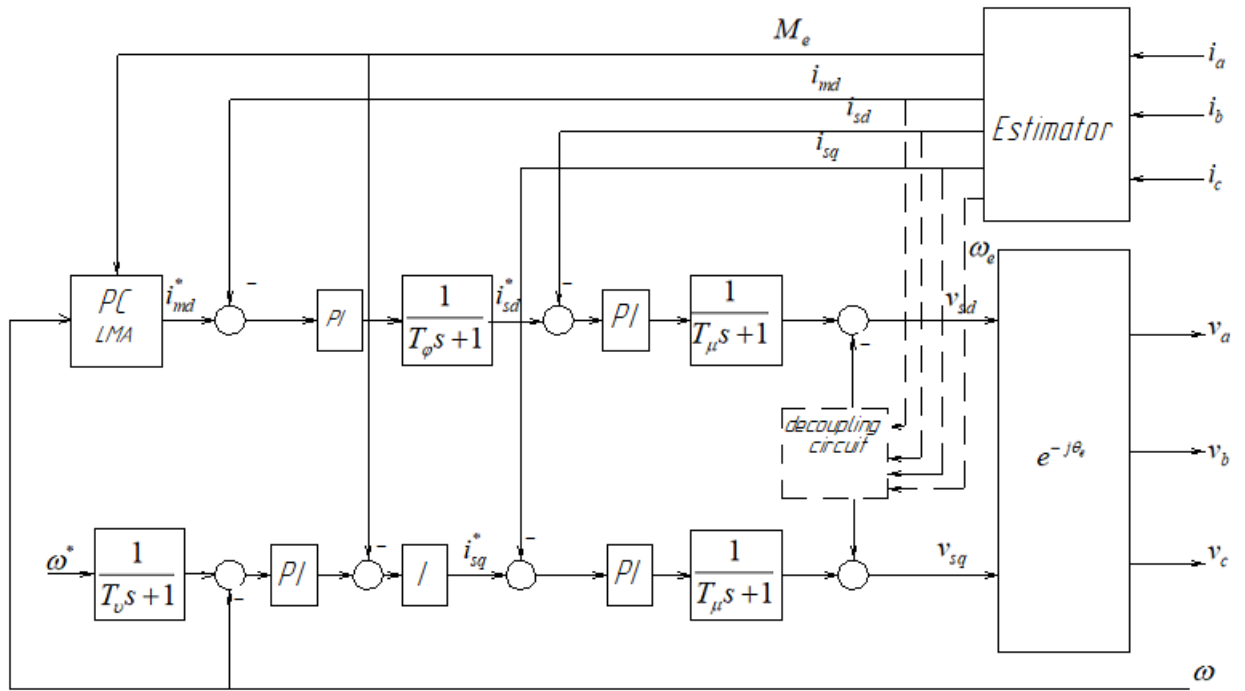


Fig. 3.19 — Block diagram of proposed loss minimization strategy

time delay in the forming of the rotor flux, which ensures a dynamic decoupling flux control and torque control.

### 3.6 Simulation Results

To examine the proposed power loss minimization strategy for induction motor based sucker rod pump drive, a numerical simulation has been carried in MATLAB software. In the simulation, the following parameters are used:  $R_s = 0.1815 \text{ ohm}$ ,  $R_r = 0.0868 \text{ ohm}$ ,  $L_s = 0.048 \text{ H}$ ,  $L_r = 0.0481 \text{ H}$ ,  $L_m = 0.0465 \text{ H}$ ,  $R_{fe} = 400 \text{ ohm}$ ,  $f = 50 \text{ Hz}$ . Two cases were considered: operation at rated flux and operation based on optimal magnetizing current trajectory. The results of the input power for the two cases are compared in Fig. 3.20 (top) and for clarity their difference is shown in Fig. 3.20 (bottom). From this result one can observe that the input power requirement at light loads is considerably reduced when the drive is operated based on optimal magnetizing current trajectory.

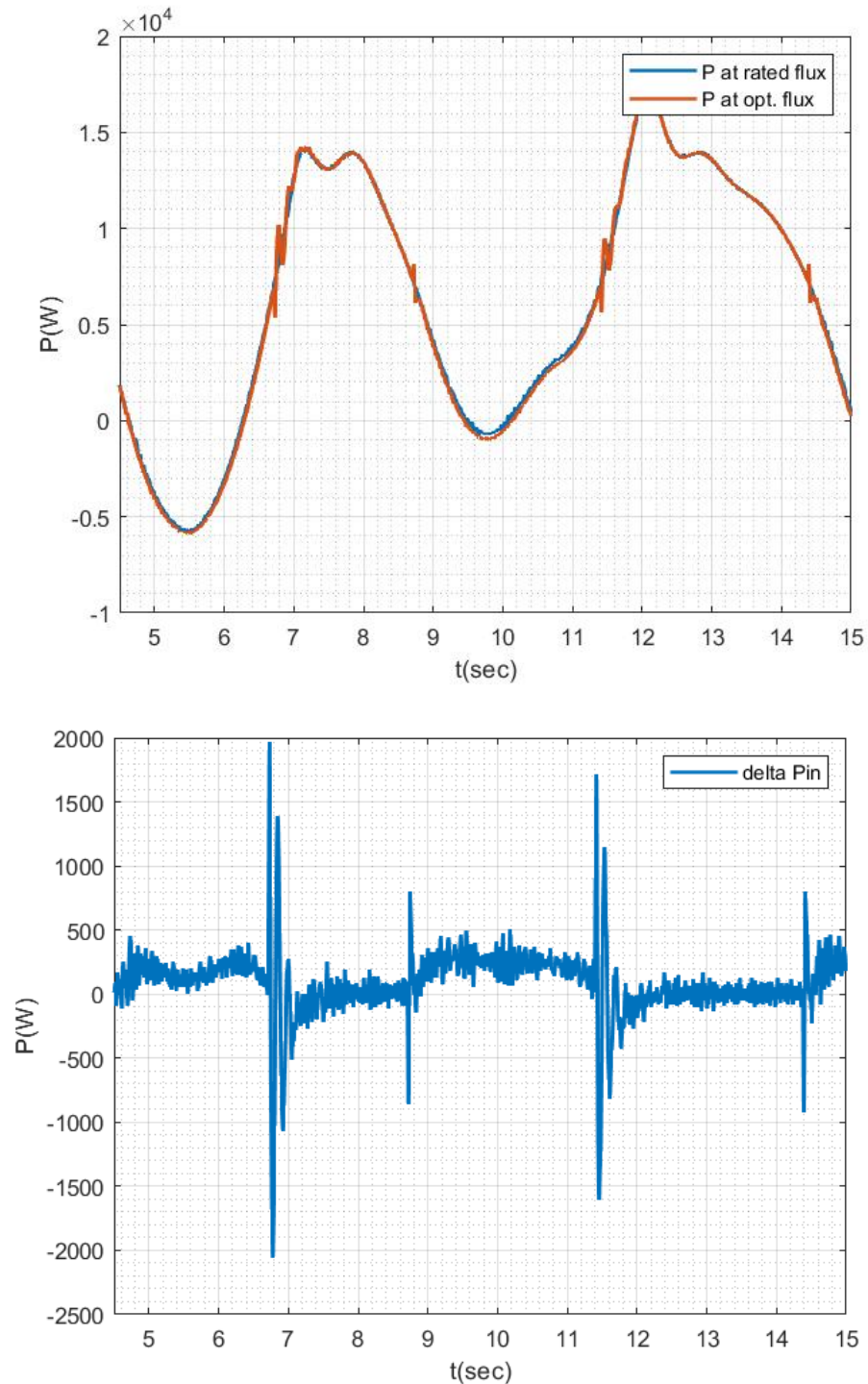


Fig. 3.20 — Top: input power (blue – with rated flux red- with optimal flux  
bottom: Difference between power input at rated flux and input power operation at optimal flux

As shown in Table 10 the energy consumed in one cycle of pump operation is lower when the efficiency optimized control strategy is applied than the operation at rated flux. About 1.6 % of the required energy can be saved if the drive is run based on optimal magnetizing current trajectory than just running at constant rated magnetizing

Table 10 — Comparison of energy consumption for one cycle of pump operation

Case	Energy consumed in one cycle of pump operation (Joules)	Fluid produced by downhole pump ( $m^3$ )	Volumetric efficiency ( $KWh/m^3$ )
Operation at rated flux	65078	0.0575	0.314
Operation at optimal flux	64123	0.0575	0.309

current. Since sucker rod pumps work for several hours per day, a small improvement in efficiency generates significant revenues. Fig. 3.21 - Fig. 3.23 show the response of actual magnetizing current, flux producing stator current, rotor speed respectively, when the efficiency optimization strategy is activated. The role of the delay introduced in the d axis is apparent from the response of flux producing current.

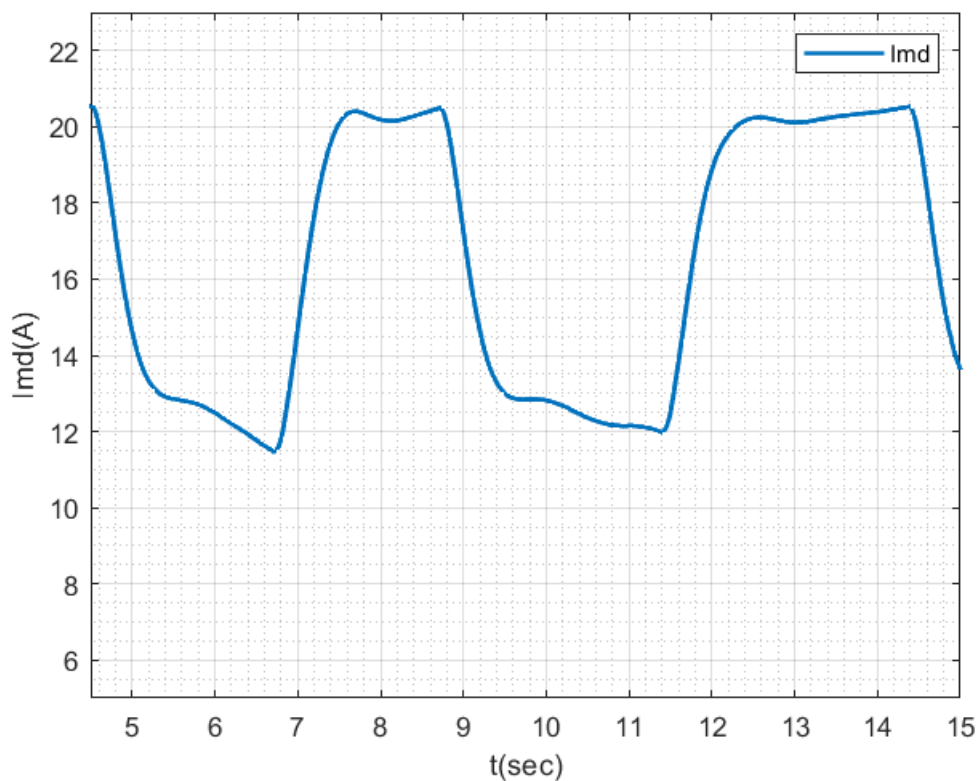


Fig. 3.21 — Magnetizing current

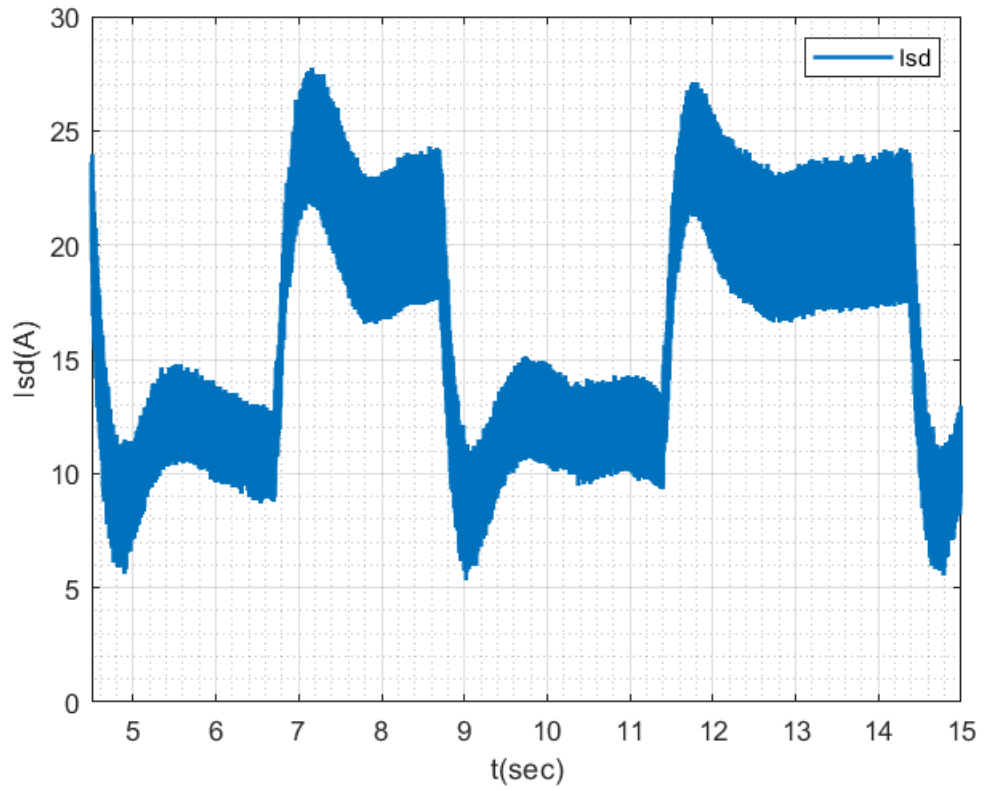


Fig. 3.22 — Flux producing stator current

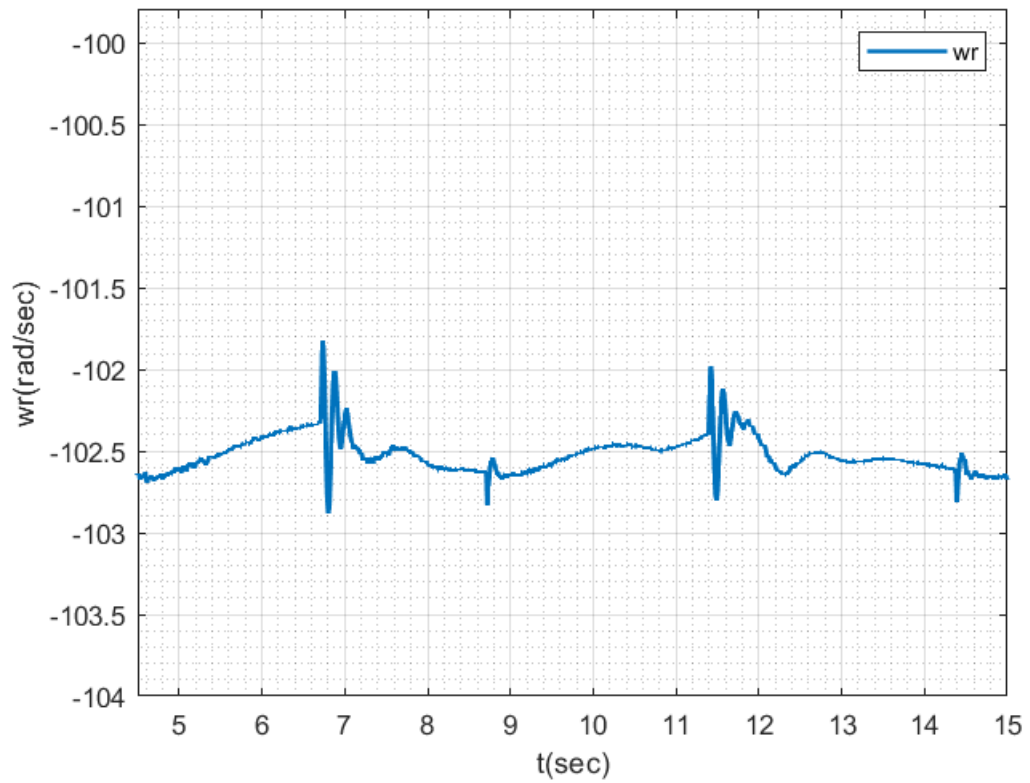


Fig. 3.23 — Rotor speed

### 3.7 Summary

An integrated model consisting models of AC-DC-AC converter, induction motor including iron loss, and sucker rod pump was developed to study energy efficiency optimization of sucker rod pump installations. A control structure based on magnetizing current control is used to fulfill the optimal energy efficiency requirement. Using the absolute value of load torque trajectory, a list of steady state electromagnetic torque is prepared. A flux producing current trajectory for one pumping cycle is defined based on the selected steady state electromagnetic torque. For each defined flux producing current trajectory, the energy loss for one complete cycle of pump operation is calculated. The results of energy loss for all possible steady state electromagnetic torques are examined and the flux producing current trajectory corresponding to the minimum energy loss is selected as optimal magnetizing current trajectory. Since the operating conditions for sucker rod pump change slowly, the search for optimal magnetizing current can be conducted off line on a PC. For a given torque trajectory, the optimal magnetizing current trajectory generated as a result of the search process is uploaded to the controller. If there is a change in torque trajectory, a new search process is conducted.

## Chapter 4. Emulating Sucker Rod Pump Dynamics

### 4.1 Introduction

There have been several improvements on the sucker rod pump technology since its invention. However, still there are demands for research and development for finding new ways that can improve its performance. For the purpose of research and development, an experimental platform, which provides convenience and facilitates experimentation and validation process, is required.

In the present chapter, an experimental electromechanical test bench and a load machine control strategy for emulating the sucker rod pump dynamics in reduced scale are developed. The sucker rod pump dynamics for different working states are emulated and the obtained experimental results are presented. Each working state can be identified by the shape of the produced dynamometer card.

### 4.2 Motivation for Sucker Rod Pump Emulation

Fig. 4.1 shows the steps in product development process. Generally, the product development process is divided into experimentation phase and production phase. However, it is a long and expensive process that contains a series of steps. First, the process starts with validation of basic conceptions using software simulations (like MATLAB, PSCAD), then proceeds with more and more deepened representation of circuit details and control functions [110]. Software simulations provide convenience in restructuring and assessing the actual processes taking place in the system, but thorough testing of the hardware under different conditions is required [111].

Due to financial and space reasons, it is impractical to keep in laboratory all kinds of mechanical loads and machines for testing, research and development purposes

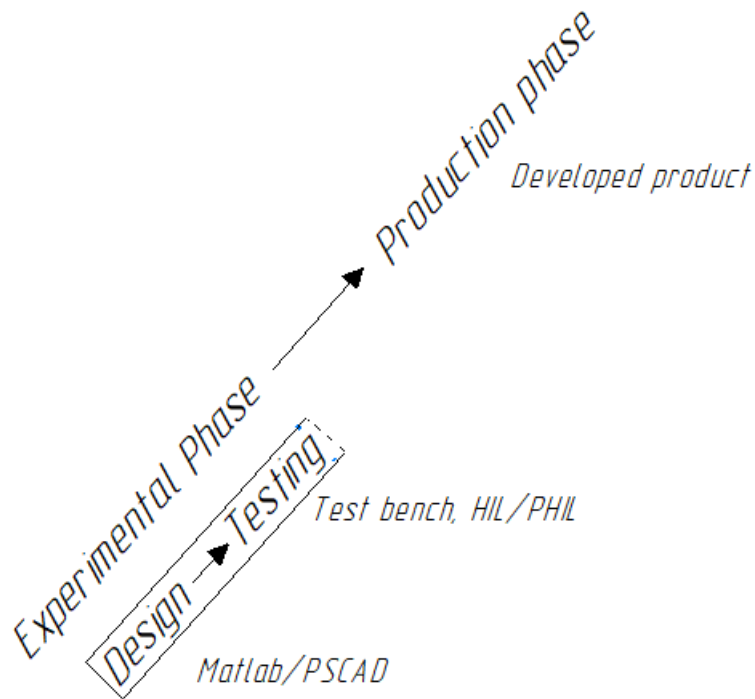


Fig. 4.1 — The steps in the product development process

[112]. In different way, these tasks can be carried out in laboratory by employing alternate facilities such as electromechanical test bench, Hardware-In-Loop (HiL) with its extension Power Hardware-In-Loop (PHiL) and their combination. The use of these methods have eased the experimentation phase for different applications. For example, emulation of wind turbine [113], electric vehicle [114; 115], lift [116], linear and non-linear loads [117], simulation of electric energy systems [118—120].

Sucker rod pump is considered a well-established technology in the oil and gas industry [2]. Their installation is easy, and they have low capital and operational costs. However, still there are ways for improving their operational performance. In other words, research and developments related to sucker rod pump technology are still on demand. Any solution must pass certain tests before it is applied. However, it is not practical to keep sucker rod pump in laboratory. In addition, most installations are situated on remote site, possibly installed in severe environmental condition [111]. Therefore, development of an experimental platform is essential.

### 4.3 Test Bench Configuration and Dynamics

A dynamometer is defined as a device for applying torque to the rotating member of the test machine, which is equipped with means for indicating torque and speed, and is not limited to a cradle base construction [121]. In the past, dynamometer was only employed to examine motor performance. However, it is also suitable for emulating both static and dynamic loads. Load emulation is a technique, in which the torque of dynamometer is controlled to create the same shaft torque on the drive under test as the desired load would do [122]. Fig. 4.2 shows a configuration where the dynamometer acts as a load for the drive machine. The dynamometer comprises load machine, power converter and the associated control system. The load machine is mechanically connected to the electrical machine in the drive under test and electrically connected to the power converter. The load machine can be any type of electrical machine that has the capability to be as motor or generator. The power converter is also required to allow the load machine to operate as a motor or generator.

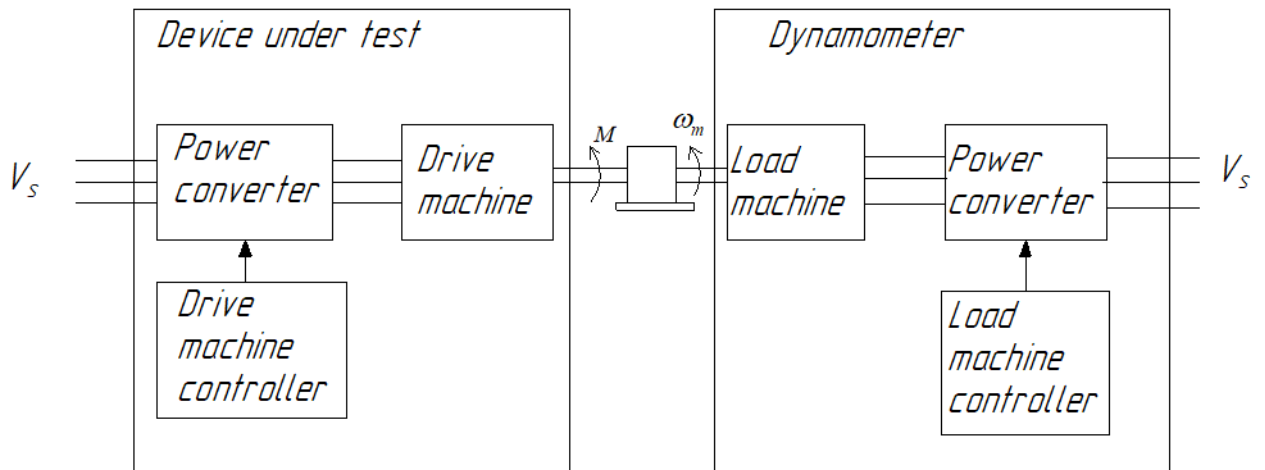


Fig. 4.2 — Diagram showing dynamometer acting as load

The test bench total dynamics can be mathematically described by:

$$M_m - M_e = J \frac{d\omega_m}{dt} + f_v \omega_m, \quad (4.1)$$

where:  $J = J_m + J_L$ ,  $f_v = f_{vm} + f_{vL}$ ,

$\omega_m$  – mechanical speed,

$M_m$  – moment developed by the driving machine,

$M_e$  – moment developed by load machine,

$J_m$  – mass inertia of driving machine,

$J_L$  – mass inertia of load machine,

$f_{vm}$  – viscous friction coefficient of driving machine,

$f_{vL}$  – viscous friction coefficient of the load machine.

Dynamometer can emulate various types of loads provided appropriate control strategy is employed. The control strategies available in literature are discussed in the next section.

#### **4.4 Review on Dynamometer Control Strategies for Emulating Mechanical Loads**

When emulating mechanical loads, dynamometer is required to develop a load torque, which has similar characteristic to that of the desired mechanical load. This requirement for load emulation is achieved using appropriate controller. In literature, load emulation can be classified into static load emulation and dynamic load emulation. In static load emulation, the reference torque to the dynamometer can be predetermined or can be determined from the speed or position of the rotor if the operating condition varies slowly. On the other hand, dynamic load emulation is an extension of static load emulation with improved software algorithms to account for cases with fast speed or torque changes [123]. Emulation of simulated load under open loop conditions is also another upgrade of static emulation.

To realize the basic idea of load emulation, it is important to have a clear knowledge on the dynamics of both the test bench and desired mechanism. Equation (4.1) describes the dynamics of the test bench mechanism but the dynamics of the

desired mechanism can be described by:

$$M_m - M_l = J_{em} \frac{d\omega_{em}}{dt} + f_{vem} \omega_{em}, \quad (4.2)$$

where:  $J_{em}$  – the moment of inertia of desired mechanism,

$f_{vem}$  – viscous friction coefficient of the desired system,

$\omega_{em}$  – the angular speed of the desired system,

$M_l$  – load torque.

It can be noted that the mechanical system in the test bench has constant inertia and viscous friction coefficient in both steady and transient state conditions. On the other hand, the inertia and viscous friction coefficient in the desired mechanism may change.

#### 4.4.1 Principle of Inverse Mechanical Dynamics

The principle of inverse mechanical dynamics is the earliest approach used in dynamic load emulation. To analyze and discuss the principle of inverse mechanical dynamics, first the open loop transfer function for the test bench and desired system are derived from (4.1) and (4.2) respectively as follows:

$$\frac{\omega_m(s)}{M_m(s)} = \frac{1}{Js + f_v}, \quad (4.3)$$

$$\frac{\omega_{em}(s)}{M_m(s)} = \frac{1}{J_{em}s + f_{vem}}, \quad (4.4)$$

where:  $s$  – Laplace operator.

The efforts of the load machine controller is intended to control the torque developed by the load machine ( $M_e$ ), so that the real speed of the imitating system tracks the desired speed. That is:

$$\omega_m = \omega_{em}. \quad (4.5)$$

After some manipulations, the reference torque for the load machine can be calculated from (4.6).

$$M_e = (J_{em}s + f_{vem})\omega_m - (Js + f_v)\omega_m \quad (4.6)$$

If the measured/estimated rotor speed is available, then emulation scheme shown in Fig. 4.3 can be used to generate the reference torque for the load machine. As the inverse of the transfer function is used for calculation of reference torque, this approach is known as the principle of inverse mechanical dynamics.

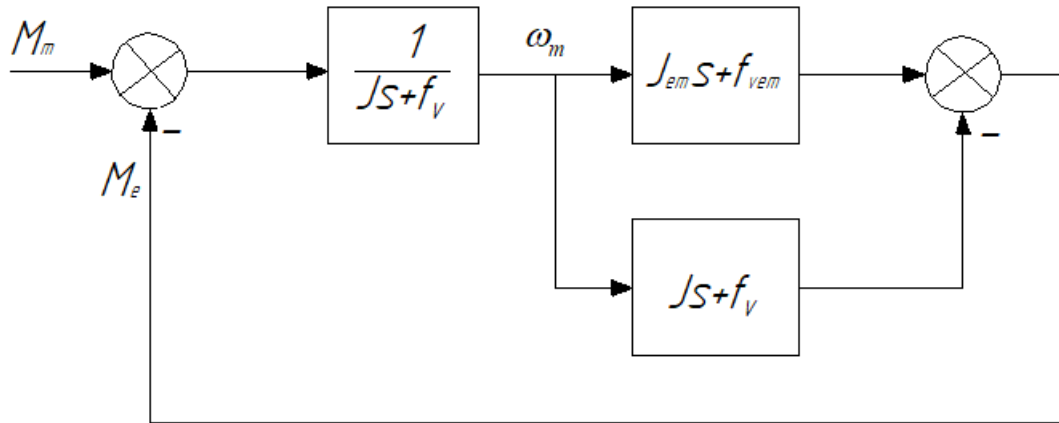


Fig. 4.3 — Load emulation based on the inverse model

Simplification of the block diagram in Fig. 4.3 gives the relation between the desired speed and motor torque (4.7), which indicates that this strategy preserves the physical causality of the system.

$$\frac{\omega_{em}(s)}{M_m(s)} = \frac{1}{J_{em}s + f_{vem}} \quad (4.7)$$

In practice, the strategy based on inverse dynamics is implemented in discrete time domain. It provides acceptable open loop emulations. However, its practical application is limited for closed loop control system. When it is used in closed loop control system, it has the following disadvantages [117; 124]:

- finding the inverse model might not be easy;
- it violates the pole-zero structure of the desired mechanical system;
- there are sampling issues.

#### 4.4.2 Feed Forward Speed Tracking with Analytical Compensator

The feed forward speed tracking with analytical compensator shown in Fig. 4.4 was proposed in [117; 125] to address the issues associated with inverse mechanical dynamics. In this approach, the desired speed ( $\omega_{em}$ ) is obtained by driving the desired dynamics ( $G_{em}$ ) by a torque produced by the feedback controller. The error between the desired speed and measured speed is applied to the speed controller  $G_t$  to generate load machine torque, which compensates the error. To cancel the motor drive torque ( $M_m$ ), the desired speed is applied to  $G_{em}^{-1}$ .

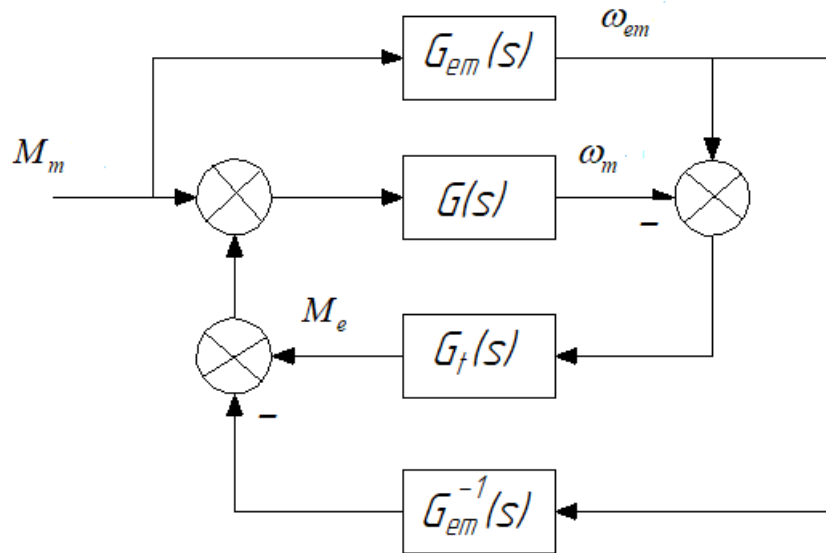


Fig. 4.4 — Load emulation using speed tracking with feed forward torque compensation

The block diagram in Fig. 4.4 can be reduced to a transfer function, which relates the real rotor speed ( $\omega_m$ ) and motor drive torque ( $M_m$ ), expressed by:

$$\frac{\omega_m(s)}{M_m(s)} = G_{em}(s) \frac{G(s)G_t(s)}{1 + G(s)G_t(s)} = G_{em}(s)G_{comp}^{-1}(s), \quad (4.8)$$

where: the compensator ( $G_{comp}$ ) is defined by:

$$G_{comp}(s) = \frac{1 + G(s)G_t(s)}{G(s)G_t(s)}.$$

Fig. 4.5 presents the equivalent system to Fig. 4.4. In Fig. 4.5, if the compensator is inserted in cascade to  $G_{em}$ , the drive loop control dynamics can be eliminated. This means, the desired transfer function  $\omega_m(s)/M_m(s)$  can be obtained and the physical

causality of the emulated system is preserved. Fig. 4.6 presents the control scheme based on speed tracking with feed forward torque compensation. Although, this approach can give very good closed-loop emulation results, but this approach considers that the dynamics are close to linear and assumes all dynamic models are well known. In fact, all dynamic models might not be well known due to parameter variation, unmodelled parameters and external disturbances.

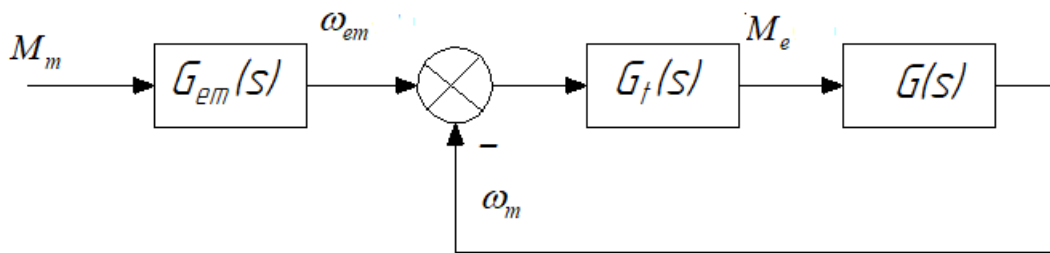


Fig. 4.5 — Load emulation using speed tracking with feed forward torque compensation after block reduction

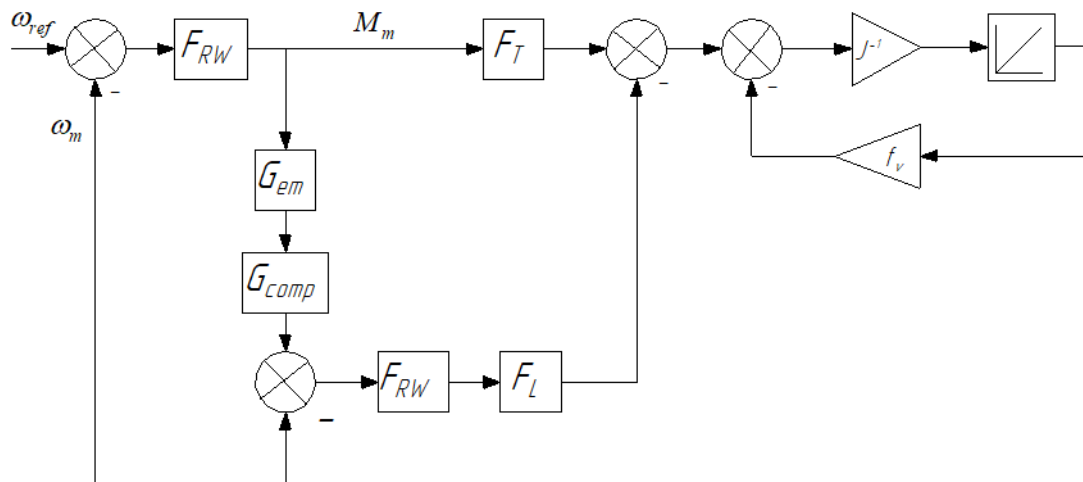


Fig. 4.6 — Control scheme based on speed with feed forward torque compensation

### 4.4.3 Nonlinear Control Based Speed Tracking

To investigate unmodeled dynamics and consider nonlinear effects, feedback PI controller [122; 126], PI estimator [126; 127] were proposed. In these methods, the

basic idea for dynamic load emulation is derived using dynamic representation of the electromechanical test bench mechanism.

Let the required load torque developed by the load machine is calculated from:

$$M_e = \hat{M}_m - u_c, \quad (4.9)$$

where:  $\hat{M}_m$  – measured or the estimated applied load torque,

$u_c$  – compensator output,

then, the dynamic equation describing the test bench configuration can be rewritten as:

$$J \frac{d\omega_m}{dt} + f_v \omega_m = M_m - \hat{M}_m + u_c. \quad (4.10)$$

If the estimated and the actual applied torques are equal, then:

$$J \frac{d\omega_m}{dt} + f_v \omega_m = u_c. \quad (4.11)$$

When the desired response ( $\omega_m = \omega_{em}$ ) is obtained, the compensator output can be written using the estimated parameters:

$$u_c = (\hat{J}s + \hat{f}_v)\omega_{em}, \quad (4.12)$$

where:  $\hat{J}$  – estimated inertia,

$\hat{f}_v$  – estimated viscous friction coefficient.

Therefore, the compensator can be defined by:

$$G_{comp}(s) = \hat{J}s + \hat{f}_v. \quad (4.13)$$

The input to the compensator can be calculated from the dynamics of the emulated mechanism:

$$G_{em}(s) = \frac{\omega_{em}(s)}{\hat{M}_m}. \quad (4.14)$$

The central thought described in the above is represented in Fig. 4.7. This method has limited practical application because its accuracy is affected by parameter variation, unmodeled dynamics, and external disturbances. To compensate the effects of parameter variation and unmodeled dynamics, the feedback controller ( $G_t$ ) as shown in Fig. 4.8 is added.

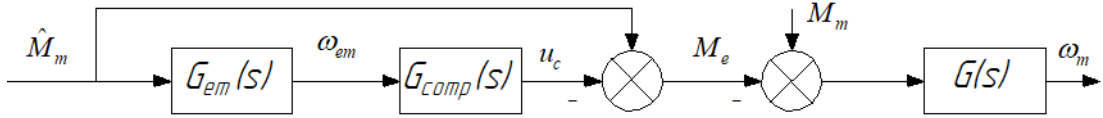


Fig. 4.7 — Dynamic emulation of mechanical loads

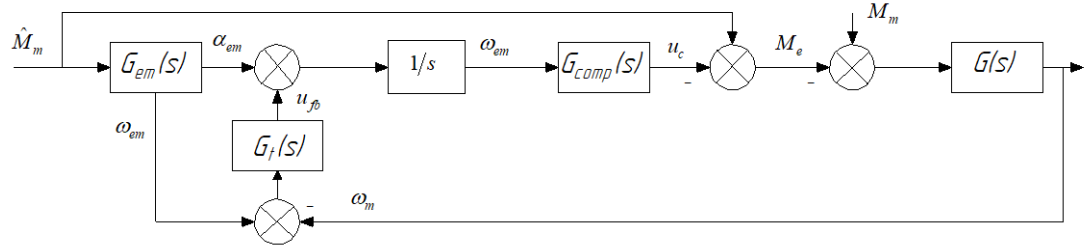


Fig. 4.8 — Dynamic emulation of mechanical loads-principle

Nonlinear disturbance torque ( $M_{fr}$ ) acts as an unknown input and significantly deteriorates the performance of the speed tracking [127]. Unknown disturbance torque can be estimated as:

$$\hat{M}_{fr} = h(\omega_{em}^c - \omega_m), \quad (4.15)$$

where:  $h$  – design parameter.

Finally, the overall control scheme with PI estimator and compensations is shown in Fig. 4.9. In Fig. 4.9, the reference torque for load machine is calculated as follows:

$$M_e = \hat{M}_m - u_c - \hat{M}_{fr}. \quad (4.16)$$

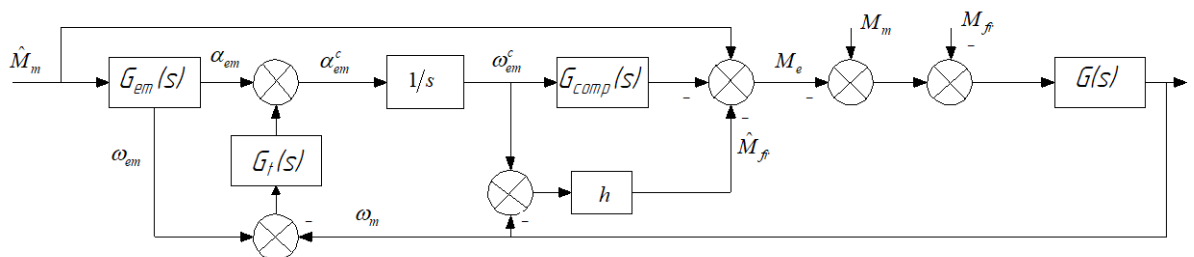


Fig. 4.9 — Final overall control scheme with PI estimator and compensations

#### 4.5 An Approach for Emulating Sucker Rod Pump Dynamics in Reduced Scale

The properties of mechanical part of an electric drive system can be described by the relation between the input (electrical torque) and output (speed). This relation is used in constructing the imitating system. When imitating any mechanical system using electromechanical test bench, the design of load machine control structure plays key role on the accuracy of the imitation process.

For sucker rod pump, the dynamic equation can be rewritten as:

$$J_{em}(\varphi_{cr}) \frac{d\omega_{em}}{dt} = M_{e1} - M_s, \quad (4.17)$$

where:  $J_{em}$  – the total reduced inertia,

$\omega_{em}$  – desired mechanical speed,

$M_{e1}$  – torque developed by the driving machine in the desired mechanism,

$M_s$  – total moment on gear reducer reduced to the rotor of the prime mover as expressed in (1.21), given by:

$$M_s = \frac{1}{u_r} \left( M_c(\varphi_{cr}) + \frac{\omega_{cr}^2}{2} \frac{dJ_{em}(\varphi_{cr})}{d\varphi_{cr}} \right)$$

$M_c$  – net gearbox torque,

$\omega_{cr}$  – angular speed of the crank,

$\varphi_{cr}$  – angular position of the crank,

$u_r$  – transformation ratio.

On the other hand, the total dynamics of the test bench can also be described by (4.1).

For economic reasons, emulating the sucker rod pump in reduced scale becomes important. A scaling factor can be deduced from the nominal torque of the drive machine driving the real mechanism and the nominal torque of the drive machine in the test bench. Therefore, the scaling factor ( $f_c$ ) can be defined as:

$$f_c = \frac{M_{n1}}{M_{n2}}, \quad (4.18)$$

where:  $M_{n1}$  – nominal torque of the driving machine in the desired mechanism (sucker rod pump),

$M_{n2}$  – the nominal torque of the driving machine in the test bench.

Now, (4.17) can be approximated as:

$$J_{em} \frac{d\omega_{em}}{dt} = f_c M_m - M_s. \quad (4.19)$$

The dynamic response of the imitated system and imitating system is an essential criterion in defining a control law used by the load machine. For accurate emulation, the following condition must be satisfied:

$$\begin{cases} \omega_m = \omega_{em}, \\ \frac{d\omega_m}{dt} = \frac{d\omega_{em}}{dt}. \end{cases} \quad (4.20)$$

Then, using (4.1), (4.19) and (4.20), the reference torque of the load machine can be obtained by:

$$M_e = \left(1 - \frac{J f_c}{J_{em}}\right) M_m + \frac{J}{J_{em}} M_s - f_v \omega_m. \quad (4.21)$$

The control structure for the drive machine can be the same as the control structure used in the real mechanism. On the other hand, the control law for the load machine must be established based on (4.21). In the practical implementation, estimated parameters are used as the dynamic model of drive machine-load machine mechanism is not always well known. The transfer function using the estimated parameters can be given by:

$$G(s) = \frac{1}{\hat{J}s + \hat{f}_v}, \quad (4.22)$$

where:  $\hat{J}$  – the estimated inertia,

$\hat{f}_v$  – estimated viscous friction coefficient.

Assuming the viscous friction coefficient is negligible, the control structure shown in Fig. 4.10 is proposed based on the established control law (4.21).  $F_T$  represents torque control loop of the drive machine and  $F_L$  represents torque control loop of the load machine. In real experimental system, the bandwidth of the torque loops is high and thus their equivalent transfer functions can be replaced by a unity gain [125].

The precision of the estimated parameters and bandwidth of the torque control loop influence the accuracy of emulation based on this strategy. If the parameters of

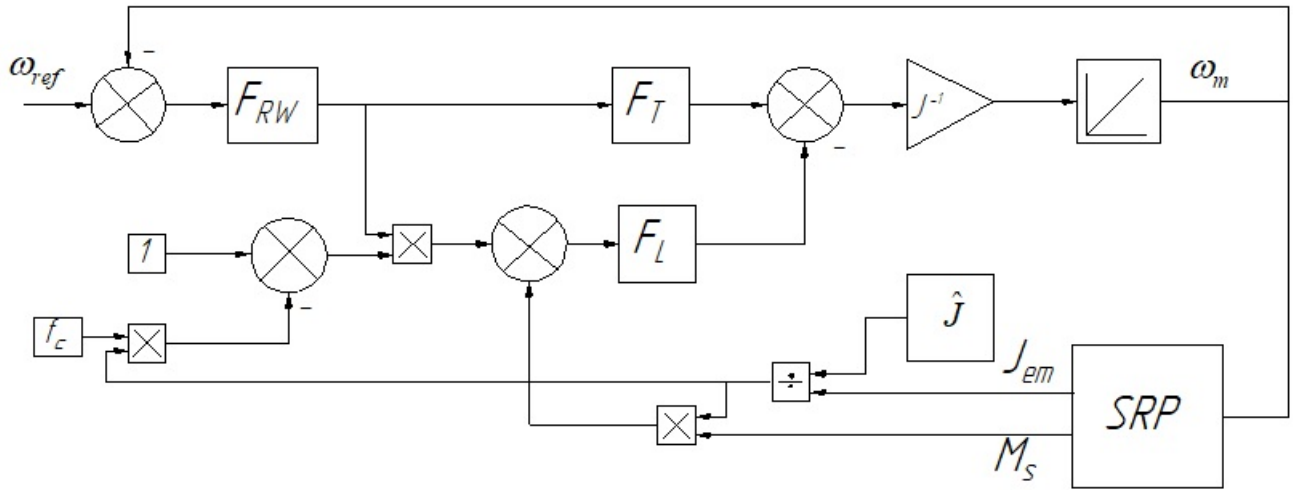


Fig. 4.10 — Proposed control strategy

the feedback controllers are selected such that the torque loops can be approximated with a unity gain, then from the control scheme shown in Fig. 4.10 the rotor speed can be expressed as:

$$\omega_m = \frac{\hat{J}}{J} \frac{1}{J_{em} s} (f_c M_m - M_s). \quad (4.23)$$

This means the relationship between the actual speed and desired speed is given by:

$$\omega_m = \frac{\hat{J}}{J} \omega_{em}. \quad (4.24)$$

Equation (4.24) shows that the rotor speed will be higher than the desired speed if moment of inertia is over estimated. Conversely, the rotor speed will be lower if moment of inertia is underestimated. In the same way, if the effect of torque control loops is considered, the rotor speed can be written as:

$$\omega_m = \left[ \left( \frac{F_T}{F_L} - \left( 1 - \frac{\hat{J} f_c}{J_{em}} \right) \right) M_m - \frac{\hat{J}}{J_{em}} M_s \right] \frac{F_L}{J_s}. \quad (4.25)$$

Equation (4.25) indicates that torque control loops affect the capability to tracking the desired speed. Therefore, this issue must be considered when selecting feedback controller parameters, otherwise, the operation will be limited to certain bandwidth.

## 4.6 Experimental Test Bench

### 4.6.1 Overview of Experimental Test Bench

For implementing the proposed control strategy, an experimental setup with the photograph shown in Fig. 4.11, where two induction motors of type 4AMA80B4Y3(1.5KW, efficiency of 77%) are connected on a common shaft, is used. Fig. 4.12 shows the schematic diagram of the overall experimental setup. The two induction motors are driven by frequency converter (ABB ACS580). A PC equipped with LabVIEW runs real time model of sucker rod pump and through a PCI data acquisition card (NI PCI- 6221), it sends analog reference speed and torque signals to the frequency converters, while at the same time it receives measured digital angular information signal from an encoder (E40S6-1000-3-24), analog shaft torque signal form torque sensor (ZMDN), voltage and current signals from voltage and current transformers.



Fig. 4.11 — Photograph of experimental test bench

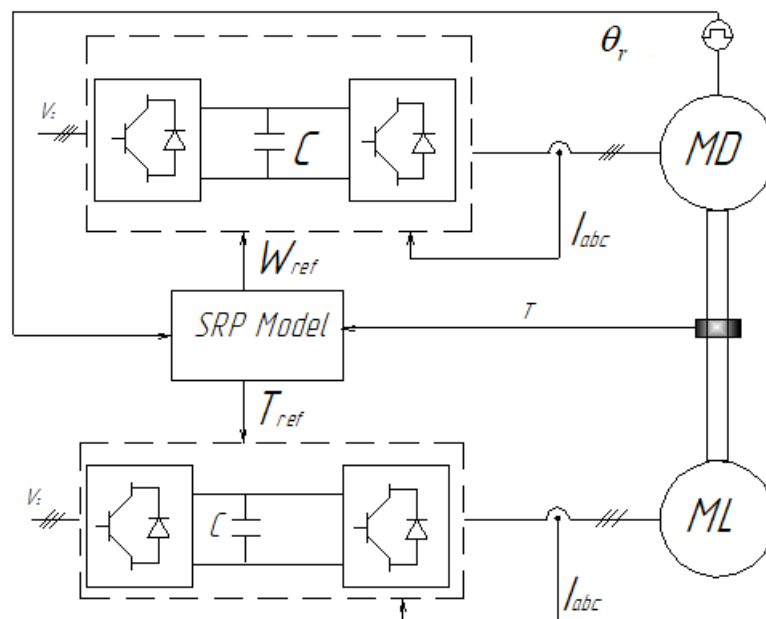


Fig. 4.12 — Schematic of experimental setup

#### 4.6.2 Sucker Rod Pump Real Time Simulator

Fig. 4.13 shows schematic of the real time simulator platform for sucker rod pump implemented in a PC. The real time model of the sucker rod pump is developed in LabVIEW programming environment. It is divided into slow subsystem with larger time step and faster subsystem with smaller time step. The slow subsystem includes the pumping unit model, dynamic emulation mechanical load algorithm. In this dissertation work, the real time simulator simulates the case when sucker rod pump is driven clockwise. The faster subsystem includes sucker rod string model, subsurface pump, and reservoir model. The PC communicates to external devices (encoder, torque sensor, voltage sensors, current sensors, and frequency converters) through a data acquisition device (NI PCI- 6221). When the real time simulator receives information, first data flows from sensor/device to hardware FIFO on NI PCI- 6221 and then from the PC buffer into the programming environment as shown in the Fig. 4.14 (top). However, when the real time simulator sends signals to an external device, first data flows from the software to an output buffer and then from the hardware FIFO to the external device as shown in Fig. 4.14 (bottom). In real time simulation, efficient data flow as well as synchronization must be ensured. These issues are influenced by:

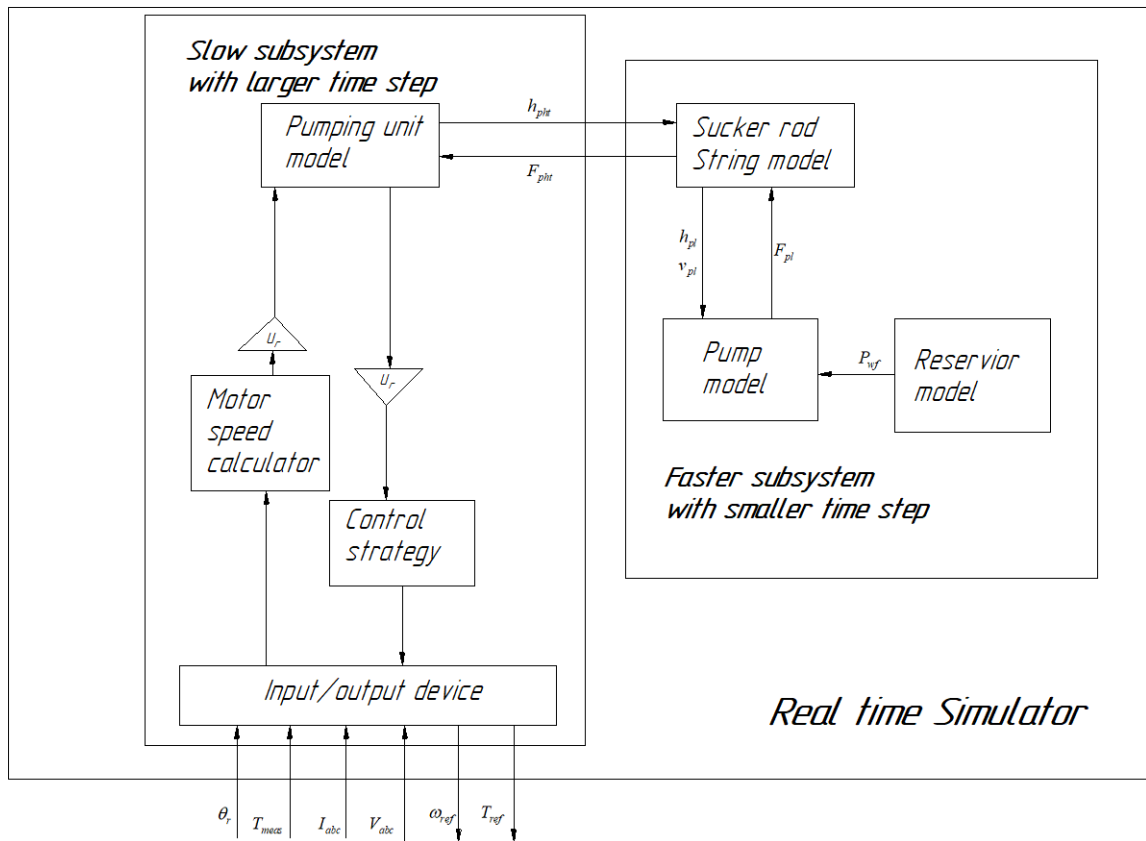


Fig. 4.13 — Real time simulation platform

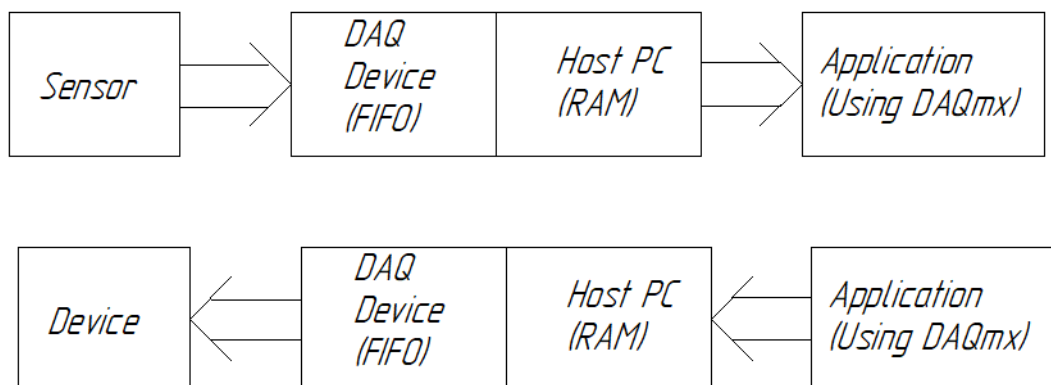


Fig. 4.14 — Schematic of data flow

- the rate of data flow from the sensor to the hardware FIFO;
- rate of data transfer from the PC buffer into the programming environment;
- the rate at which the data is put on the hardware FIFO;
- the rate at which data is generated.

The PCI 6221 National Instrument has found excellent application for performing experiments. It implements a high-performance digital engine, which provides many useful features such as flexible AI and AO sample and convert timing; independent

AI, AO, DI, and DO FIFOs; two flexible 32 bit counter/timer modules with hardware gating; PCI/PXI interface; PLL for clock synchronization; etc [128]. Moreover, like other NI devices, the use of NI-DAQmx software driver with NI PCI- 6221 helps to simplify the configuration and measurement process.

The configuration on the DAQmx Timing function determines how fast the samples are acquired and put on the hardware FIFO and the configuration on the DAQmx Read function determines how many samples are pulled from the PC buffer to the programming environment. Similarly, the configuration on the DAQmx Timing function determines how fast the samples are retrieved from the hardware FIFO and send to the external device. 0.01 second is used as the time step for the slow subsystem and 0.0001 second for the faster subsystem. This means for each time step of the slow subsystem, the faster subsystem runs 100 times.

### **4.6.3 ABB ACS 580**

ABB ACS580 (Fig. 4.15) is a frequency converter, which is suitable for many different applications. It includes rectifier, dc link, as well as inverter, which can be controlled based on direct torque control (DTC) [129] or scalar control. This converter possesses several control macros, which are set of default parameter values suitable for a certain control configuration [114]. The use of macros have eased the configuration of this converter. For example, by selecting suitable macro, the control principle can be switched from scalar to vector or vice-versa. When vector control is selected, the ABB ACS580 provides an external torque reference as an alternative to the reference torque generated by the speed controller. In addition, ACS580 offers better process control as it has many built-in features and functions such as input/output, reverse function, ramp time acceleration/deceleration, variable torque v/Hz setting, safe torque-off, etc [130]. ACS 580 drive can obtain information about different kinds of processes through inputs/outputs to control the motor. Moreover, it possesses braking chopper,

through which braking resistors can be connected to handle regenerative power from a decelerating motor.



Fig. 4.15 — Picture of ACS580

The converter which supplies the drive machine is configured to regulate the speed of the driving machine while the converter which supplies the load machine controls the developed torque by the load machine.

#### 4.6.4 Current, Voltage, Torque, and Speed Measurement

To examine the experimental system, electrical and mechanical measurements are taken. Electrical measurements at the input and out of the frequency converter are measured using voltage and current transformers. The shaft torque is measured using ZMDN dynamic torque transducer. This transducer consists of strain gauges configured in bridge form and can measure both positive and negative torques. For all the analogue input signals, the configuration on the DAQmx Timing function determines how fast the samples are acquired. An incremental rotary encoder is commonly used to measure the

shaft speed of an electric motor. It employs a rotary electromechanical device to convert shaft rotation into electronic pulses from which the machine position and velocity are determined. Incremental rotary encoders have excellent accuracy and flexibility. Due to these advantages, they are suitable for applications which require motion control. In the experimental setup, the angular information of the common shaft of the test bench mechanism is measured through E40S6-1000-3-24, which is an incremental rotary encoder. With E40S6-1000-3-24, the angular information of the shaft is provided by two quadrature signals while a third signal indicates the reference position. The incremental rotary encoder is interfaced to the real time simulator through the NI PCI 6221 data acquisition card. Using the DAQmx function, the shaft speed is determined. The overall system resolution is 1000 pulses per revolution.

#### **4.6.5 Creation of Surface Dynamometer Card from Motor Measurements**

Dynamometer card is the first-hand tool for performance analysis and diagnosis in sucker rod pump installations. It is constructed from a time series data of polished rod load and polished rod displacement. There are different types of sensors for measuring the polished rod load and displacement. However, their accuracy and/or reliability is not satisfactory. In a different way, the polished rod load can be calculated from net motor torque signal while the polished rod displacement from rotor speed. Modern frequency converters provide estimates of motor torque and rotor speed. The study in [131] related to the accuracy of frequency converter estimates based on induction motor drives indicate that the relative errors are very low (0.2% for rotor speed, 2.1% for shaft power and shaft torque). Since estimation of net motor torque signal and rotor speed are based on more reliable voltage and current measurements, this approach improves the reliability of the source of information.

For a given machine, it is possible to predict an efficiency curve from electrical and mechanical measurements. Fig. 4.16 shows the efficiency curve obtained from

experiments conducted on the driving machine in the test bench. The shaft power can be determined using the efficiency curve shown in Fig. 4.16. Once, the shaft power is known, the shaft torque can be determined.

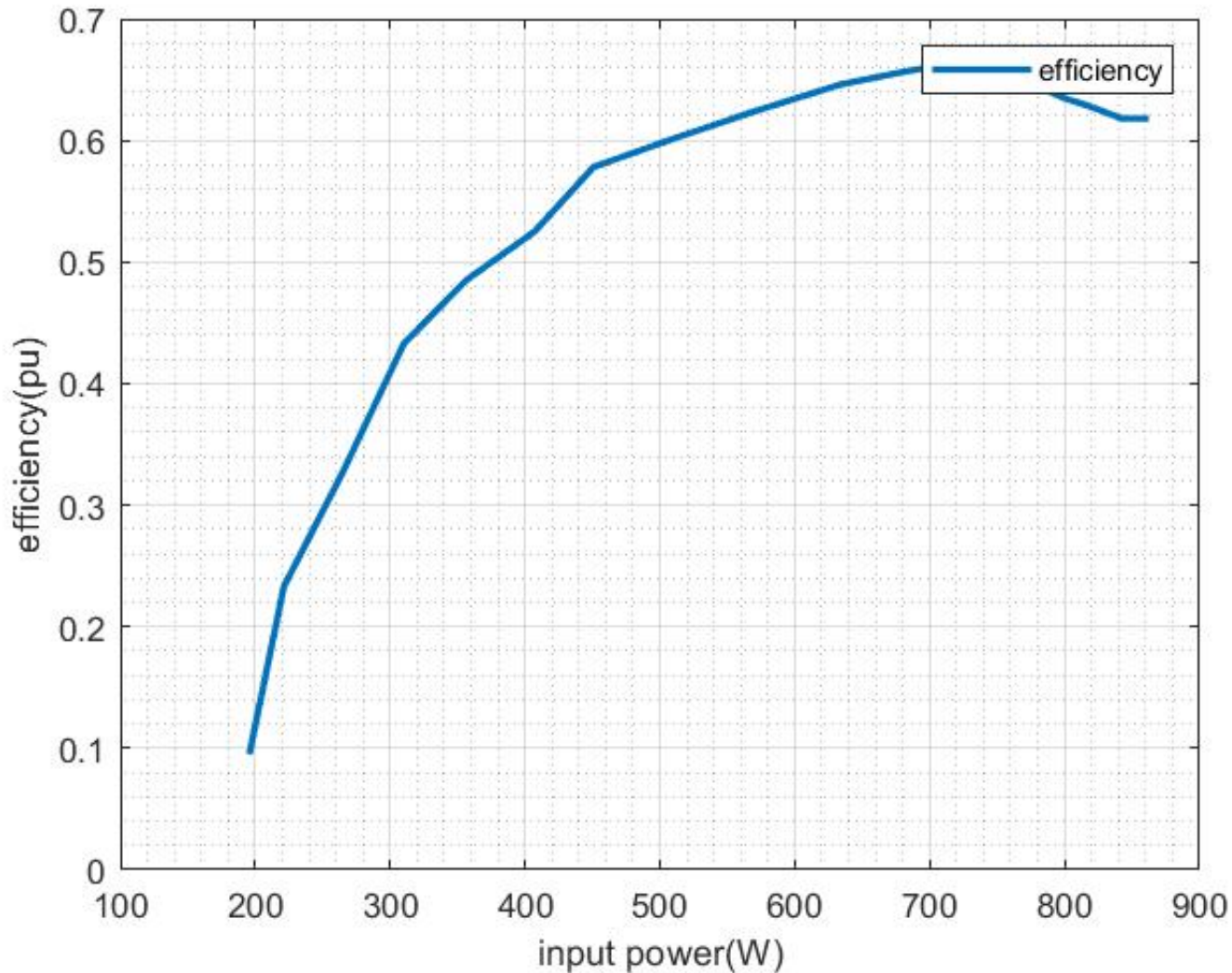


Fig. 4.16 — Efficiency curve

The gearbox torque analysis is important to define a procedure that helps to find the correspondence between the polished rod load and the net motor torque. The net torque on the gearbox is the sum of polished rod load, counterbalance torque, inertial torques and frictional torques. If inertial and frictional torques are neglected, then the net gearbox torque:

$$M_s = M_{pht} + M_{cb}, \quad (4.26)$$

where:  $M_{pht}$  – the torque due to polished rod load,

$M_{cb}$  – the torque due to counterweight.

The equivalent moment due to polished rod load on the crank side can be given:

$$M_{pht} = F_{pht}TF(\varphi_{cr}), \quad (4.27)$$

where:  $F_{pht}$  – polished rod load at crank angle ( $\varphi_{cr}$ ),

$TF$  – the torque factor defined in (1.16).

The net gearbox torque can also be calculated from the motor torque by:

$$M_s = u_r M_m. \quad (4.28)$$

Using (4.26)-(4.28), the polished rod load can be expressed as:

$$F_{pht} = (M_m u_r - M_{cb}) \frac{1}{TF(\varphi_{cr})}. \quad (4.29)$$

The crank speed can also be expressed as a function of rotor speed as:

$$\omega_{cr} = \frac{\omega}{u_r z_p}. \quad (4.30)$$

Once the crank speed is known, the torque factor and polished rod displacement can be calculated using the kinematic analysis methods.

## 4.7 Experimental Results

The load emulation capability of the experimental setup is evaluated using current, voltage, torque and speed measurements. The mechanical power and active power at terminals of the converter which supplies the drive machine can be calculated from these measurements.

First, the real time simulation model of the sucker rod pump was set to simulate the normal working condition and then, the sucker rod pump was emulated in reduced scale using the experimental setup based on the proposed control strategy. The results shown here are for the case when the real time simulator simulates a clockwise driven pumping unit (motoring mode in III quadrant of the mechanical characteristics). Fig.

4.17 depicts comparison between measured rotor speed and reference speed. The measured speed shows variations compared to reference speed due to load fluctuation. Fig. 4.18 depicts comparison between reference torque and measured shaft torque. Generally, the measured torque nearly follows the reference torque but there is a small error. As can be seen, the error during time of rotor deceleration differs from the error during time of rotor acceleration. Fig. 4.19 depicts comparison between active power at the input terminals of the converter which supplies the drive machine and the mechanical power. The curves of the active power and mechanical power are similar, but the input power is greater than the mechanical power due to electrical and mechanical losses. The drive machine used in this experimental setup have low efficiency. Its efficiency becomes even lower as it is operated at speed and torque lower than the nominal values. For this reason the total losses in this experiment are more. The mechanical power becomes negative in some parts of the cycle. This shows that the motor operates in regenerative mode. Regenerative operation mode is not seen in the curve of active power input at the converter as the energy is dissipated in the machine itself. Fig. 4.20 depicts the calculated dynamometer card from motor measurements. The shape of the dynamometer card is a sign of normal working condition. This validates the use of the proposed control strategy for emulating sucker rod pump.

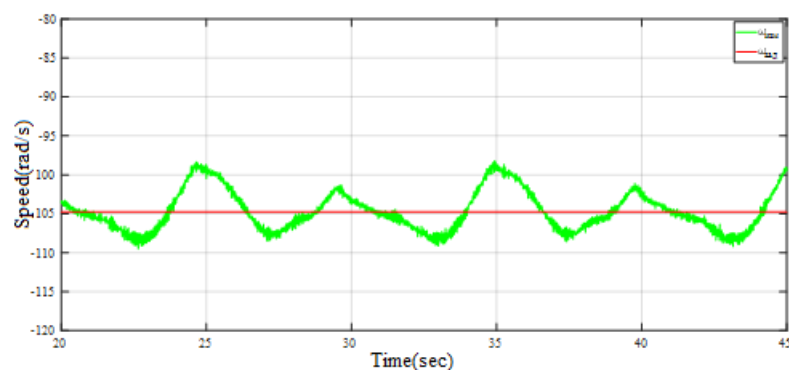


Fig. 4.17 — Reference speed (red) and measured speed (green) comparison

The sucker rod pump often works under faulty conditions. Some faulty working conditions are emulated using the experimental setup based on the proposed strategy. Comparison of active power input with mechanical power and dynamometer card calculated from motor measurements are presented in Fig. 4.21 and Fig. 4.22

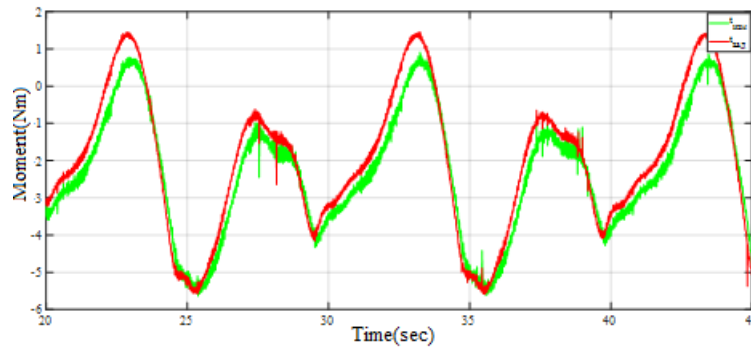


Fig. 4.18 — Reference torque (red) and measured torque (green) comparison

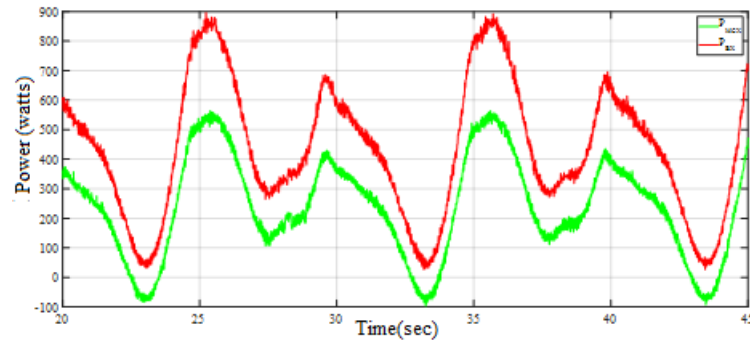


Fig. 4.19 — Normal working state: active power at the input of converter (red) and mechanical power (green)

respectively for gas affected , Fig. 4.23 and Fig. 4.24 respectively for travelling valve leakage, Fig. 4.25 and Fig. 4.26 respectively for plunger hitting top dead center, Fig. 4.27 and Fig. 4.28 respectively for plunger hitting bottom dead center. It is not easy to identify the working state directly from motor power curve. Working state detection from motor power curve requires computer aided techniques. However, the working state of the sucker rod pump can be detected by noting the shape of the calculated dynamometer card.

#### 4.8 Emulating the Sucker Rod Pump Using PHiL Simulator

The PHiL simulator have eased the experimentation phase for various electric energy systems by imitating the power generation or consumption. The input power to the sucker rod pump drive is periodic with period equal to the period of one cycle of pump operation. Moreover, the input power curve reflects the effects of different

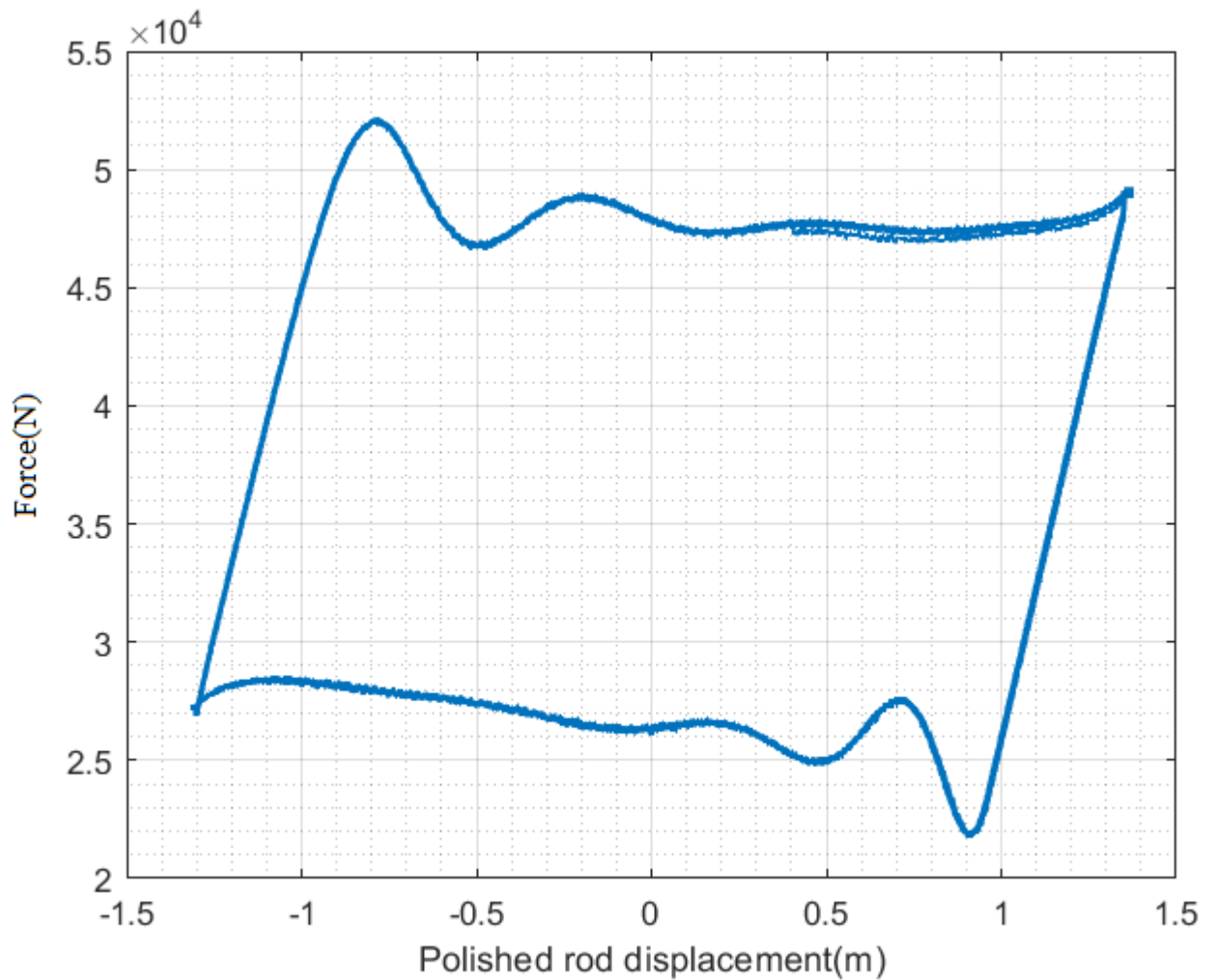


Fig. 4.20 — Dynamometer card for normal working state

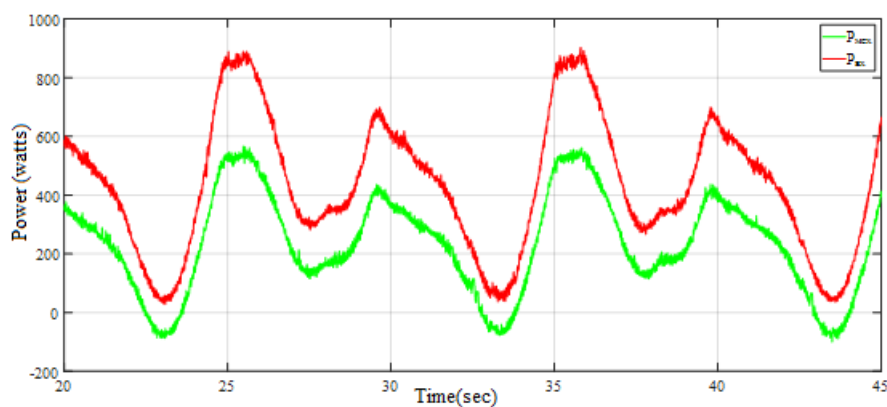


Fig. 4.21 — Gas affected: active power at the input of converter (red) and mechanical power (green)

forces exerted on the surface and subsurface components along their corresponding time. Therefore, the PHiL simulator can also be used to emulate the sucker rod pump dynamics by imitating the simulated input power curve to sucker rod pump drive. The PHiL structure as shown in Fig. 4.29 is developed in Simulink using Simscape library

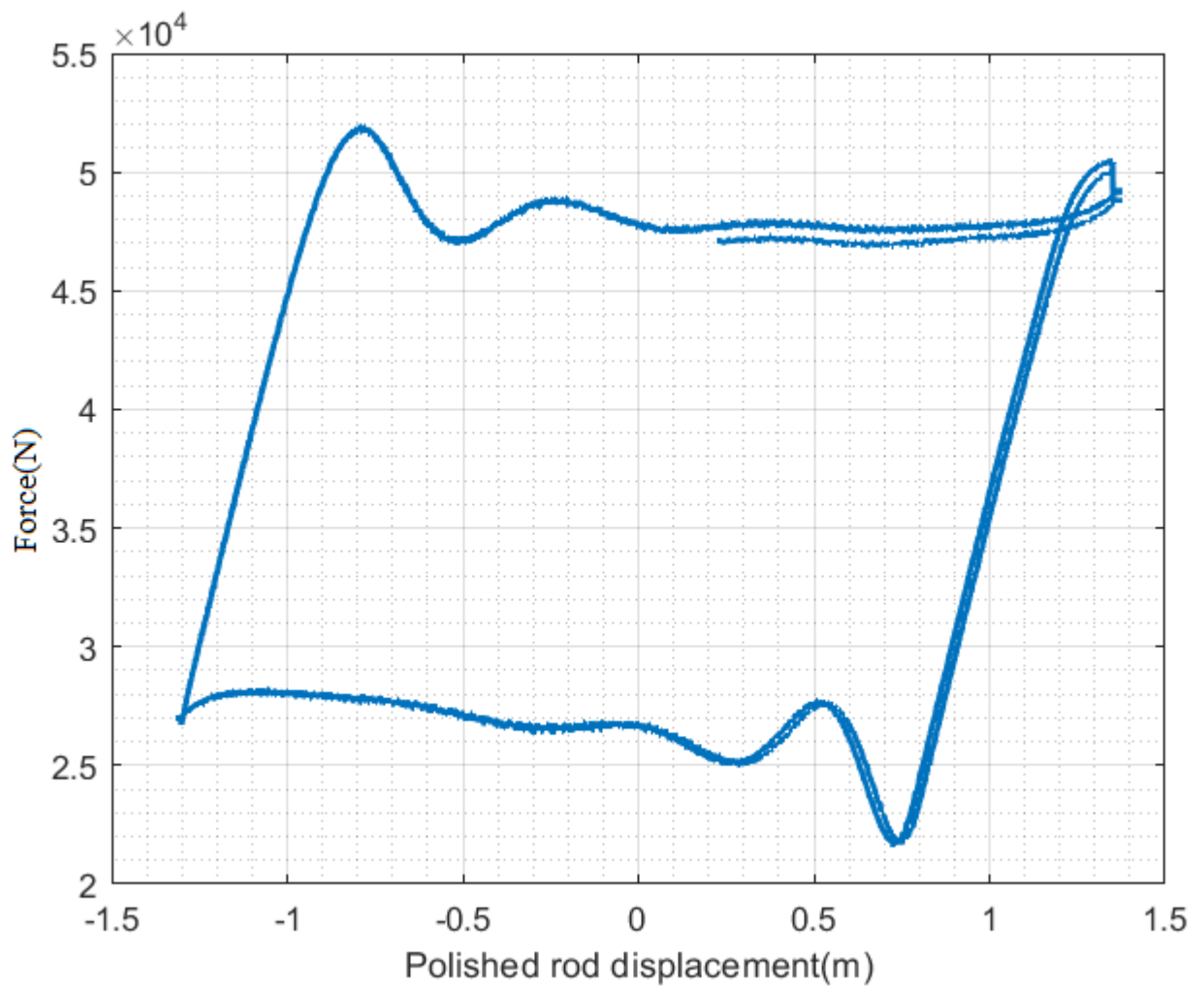


Fig. 4.22 — Dynamometer card for gas affected

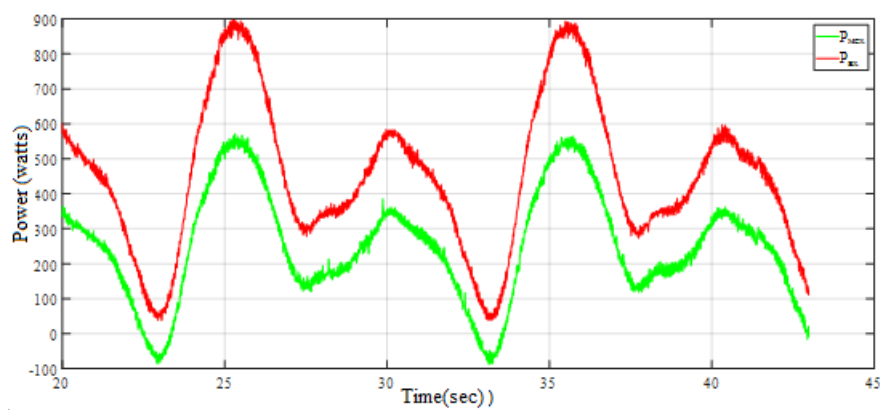


Fig. 4.23 — Travelling valve leakage: active power at the input of converter (red) and mechanical power (green)

to examine the PHiL simulator's capability to emulate the sucker rod pump. In this structure, if the load converter is controlled such that it forces the current flowing through the coupling inductor to follow the model generated stator current of the motor

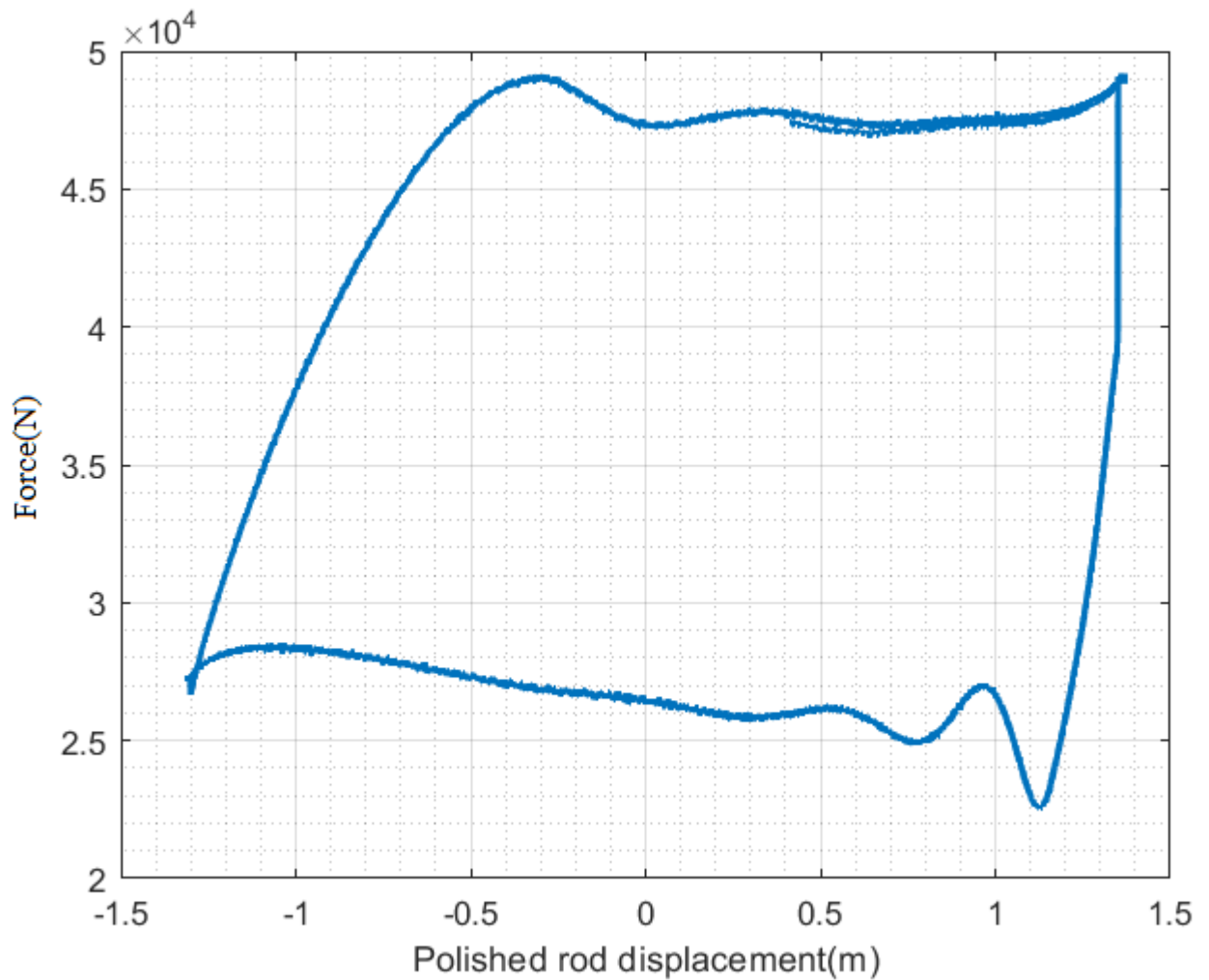


Fig. 4.24 — Dynamometer card for traveling valve leakage

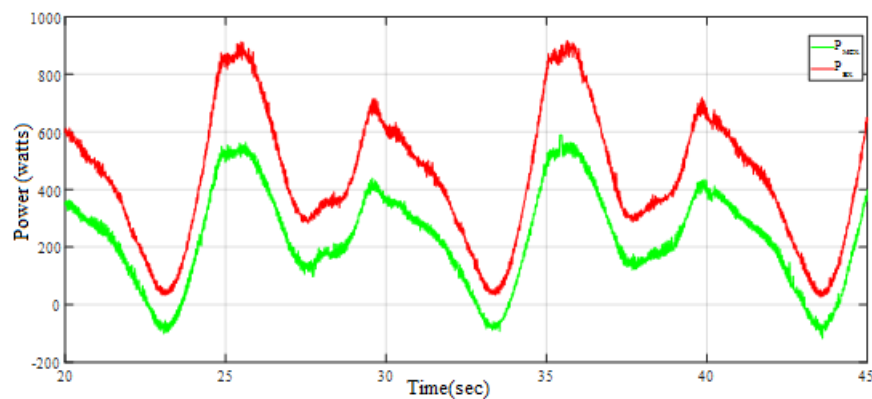


Fig. 4.25 — Plunger hitting top dead center: active power at the input of converter (red) and mechanical power (green)

driving the sucker rod pump, the power supplied to the boost converter will be equal to the simulated power.

The power supplied to the boost converter can be calculated by:

$$P_{in} = u_a i_{la} + u_b i_{lb} + u_c i_{lc}, \quad (4.31)$$

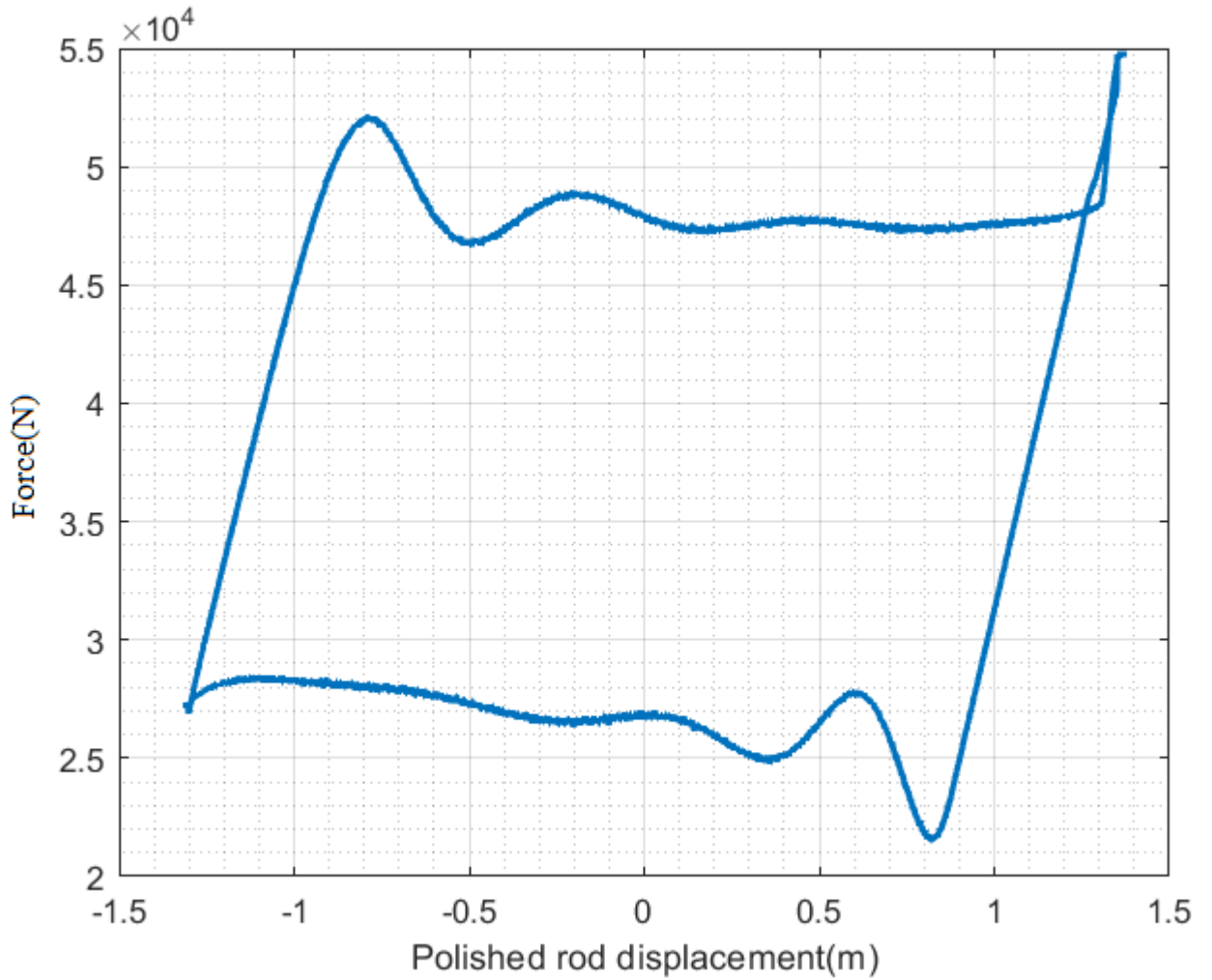


Fig. 4.26 — Dynamometer card for plunger hitting top dead center

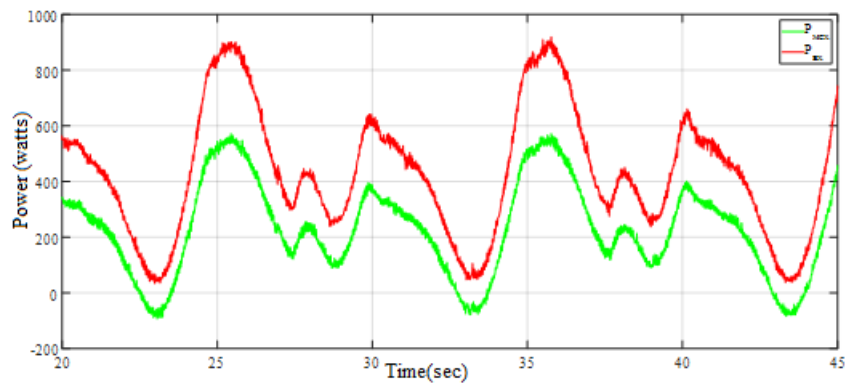


Fig. 4.27 — Plunger hitting bottom dead center: active power at the input of converter (red) and mechanical power (green)

where:  $u_a, u_b, u_c$  are phase voltages at the output of three phase test converter,

$i_{la}, i_{lb}, i_{lc}$  are line currents in the coupling inductor.

From the HiL system, the total electrical losses in motor can also be calculated by:

$$P_{loss} = R_s(i_{as}^2 + i_{bs}^2 + i_{cs}^2) + R_r(i_{\alpha_r}^2 + i_{\beta_r}^2), \quad (4.32)$$

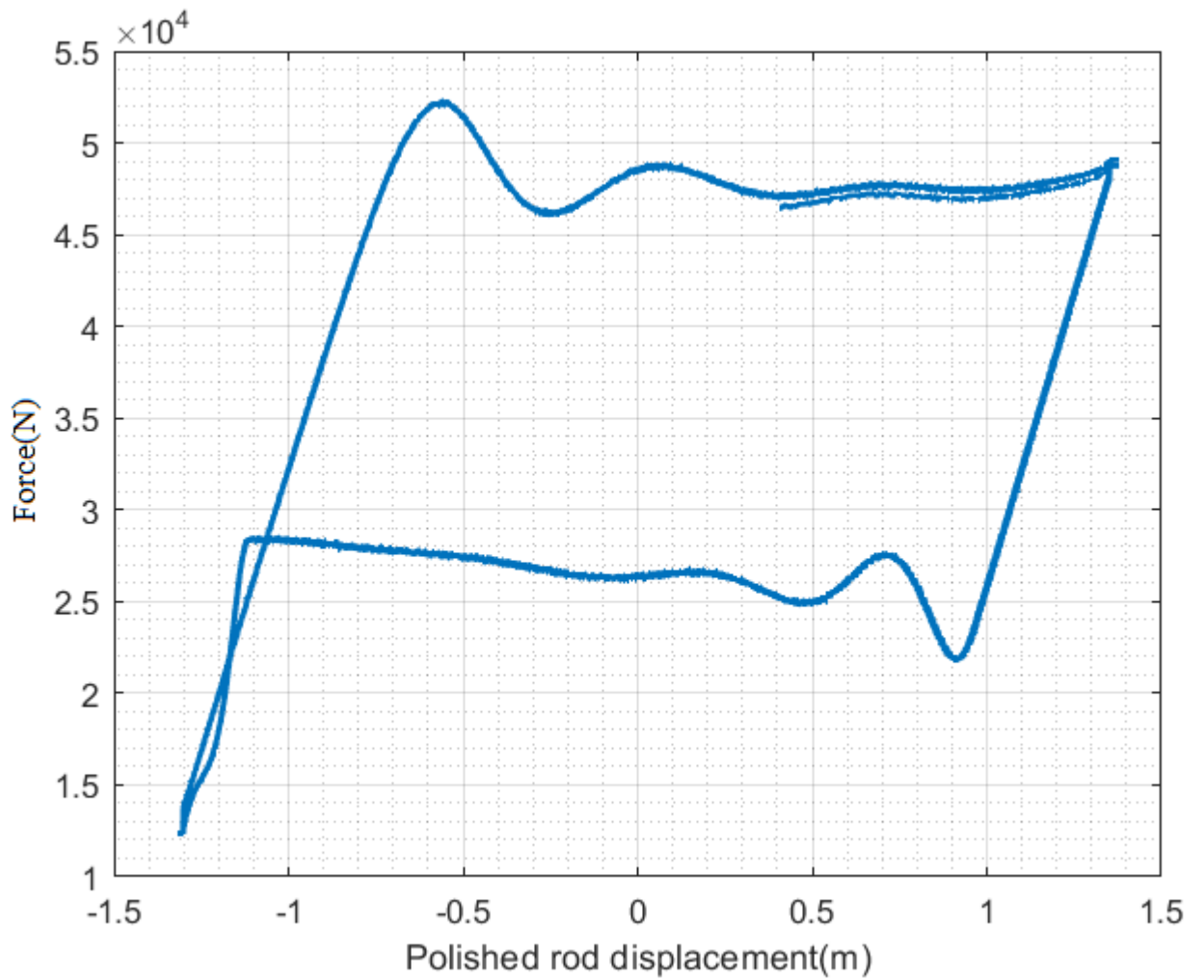


Fig. 4.28 — Dynamometer card for plunger hitting bottom dead center

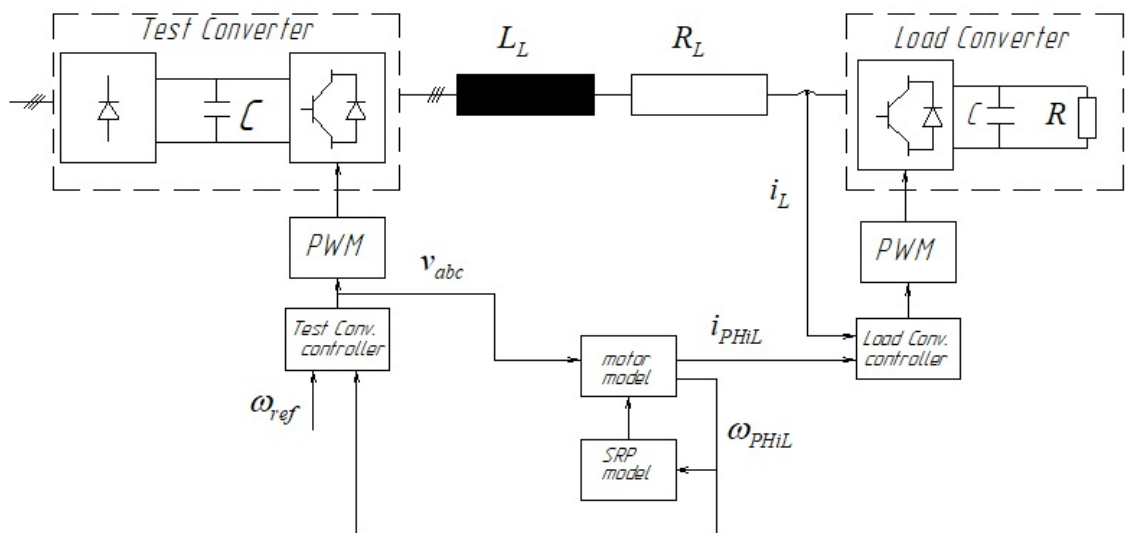


Fig. 4.29 — PHiL simulator

where:  $i_{\alpha r} = \frac{1}{x_r}(\psi_{ra} - x_m i_a)$ ,

$$i_{\beta r} = \frac{1}{\sqrt{3}x_r}(\psi_{rb} - \psi_{rc} - x_m(i_{sb} - i_{sc})),$$

$x_r$  and  $x_m$  are rotor and mutual inductive reactance respectively,

$\psi_{ra}, \psi_{rb}, \psi_{rc}$  are rotor flux for phase a, b, and c respectively.

Then, the net motor torque can be obtained by:

$$M_e = \frac{P_{in} - P_{loss}}{\omega_{HiL}} \quad (4.33)$$

where:  $\omega_{HiL}$  is the simulated speed.

The net motor torque and simulated speed can be used to calculate the polished rod load and displacement from which the dynamometer card is produced. For normal working state, the obtained dynamometer card is compared with the dynamometer card which is obtained from the experimental results of electromechanical test bench in Fig. 4.30. It can be seen that the two dynamometer cards are nearly comparable.

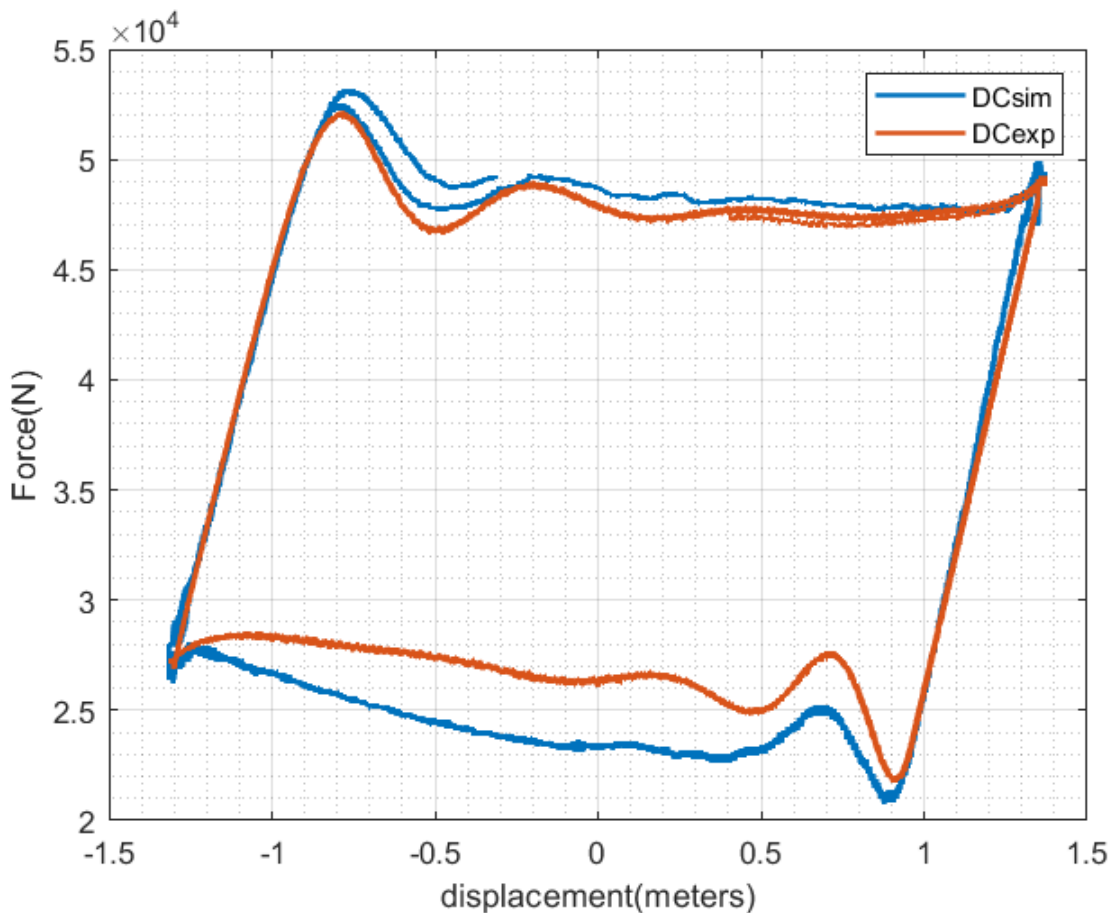


Fig. 4.30 — Comparison of dynamometer cards produced from PHiL simulator and test bench

## 4.9 Summary

In this chapter, load machine control strategy for emulating sucker rod pump in reduced scale has been developed. To verify the emulation strategy, an experimental test bench has been developed in laboratory. Using the experimental setup, the dynamics of sucker rod pump under different working states was emulated. From the recorded motor measurements, dynamometer cards are calculated. The shape of each calculated dynamometer card is a sign of the working state simulated on the real time simulator. The experimental results are also comparable with the PHiL simulation results. This validates the proposed emulation strategy. The experimental setup can serve as an effective platform for generating a training set (motor power curves for different sucker rod pump working states). Moreover, studies on optimal counterbalance and optimal energy efficiency operation could be conducted using this test bench.

## Conclusion

The work presented in this dissertation concerns research on sucker rod pump particularly: in developing an integrated simulation model, establishing a diagnostic model based on motor power curve, studying energy efficiency improvement and developing emulating system. The research is assisted with an integrated simulation model and electromechanical test bench. The research findings are demonstrated by simulation and experimental results. The main issues and corresponding findings are summarized eventually.

Chapter 1 presents mathematical models of induction motor, v-belt, gear reducer, pumping unit, sucker rod string, subsurface pump and reservoir. All these models are combined to form an integrated model of sucker rod pump system. The integrated simulation model is developed in LabVIEW programming environment and MATLAB (in form text files, using Simulink and Simscape libraries). It allows to simulate different sucker rod pump working states. Therefore, through the developed model different samples can be generated and used to build training set, which is the main requirement in developing computer aided diagnostic models. Moreover, the models are helpful to study energy efficiency of sucker rod pump and in developing emulating system for sucker rod pump.

Chapter 2 presents development of computer aided diagnostic model based on motor power curve. The motor power curve is more reliable source of information to diagnostic systems, however, its utilization requires computer aided techniques. In the development of computer aided diagnostic model, the issue related to data requirement is addressed by generating several samples, which represent different sucker rod pump working states, through an integrated simulation model of the sucker rod pump. The valve working points and the relative energy of different parts of a cycle provide meaningful information about sucker rod pump working condition. Thus, each sample is represented by a feature vector, which is constructed based on the relative work coefficient of the four parts of the cycle and distances between valve working

points. The feature vector constructed based on this idea has been seen to uniquely represent a given sample of motor power curve. A training set is prepared by generating samples of motor power curves after extracting useful features for each sample. Finally, the SVM algorithm uses the training set to develop a diagnostic model. The SVM algorithm is the most suitable algorithm for model generated data. Simulation tests on the capability of the developed diagnostic model indicate satisfactory results. The SVM algorithm, the programs for classification and feature extraction processes have been developed in MATLAB programming environment but they can also be rewritten in other programming languages. Moreover, the programs for classification and feature extraction processes can be prepared to run on simple device, which can be used for onsite applications, with the training process performed in a centralized unit.

In chapter 3, the model of induction motor in the integrated simulation model is modified to include the effects of iron loss. The model of AC-DC-AC converter is added to the modified integrated model. A loss model and control structure that allows to control the magnetizing current are developed. Applying unconstrained optimization technique, an expression for computing optimal flux producing current is derived. In the base speed region including the current constraints, the relation between optimal flux and torque producing currents is outlined and the torques at the limits are predicted. The predicted torques are used in guiding the development of special strategy for generating magnetizing current trajectory, which is used as a command by a vector control system used to control induction motor driving sucker rod pump. The effectiveness of this strategy was examined in simulation. The simulation results indicate that about 1.6% of the required energy can be saved compared to operation at rated magnetizing current. This strategy, with further research and development, can help to meet energy efficiency targets and standards.

In chapter 4, an experimental platform consisting of two induction motors coupled on a common shaft, two frequency converters, and PC equipped with LabVIEW and input/output device is constructed. By considering equal dynamic response of the electromechanical test bench and desired system (sucker rod pump), load machine control structure for emulating the sucker rod pump in reduced scale is established.

The proposed load machine control structure was implemented and tested in the developed experimental platform with the real time model of the sucker rod pump set to simulate different working states. It is seen that the measured torque nearly follows the reference torque. The shape of the calculated dynamometer card from the motor measurements also very well reflects the simulated working state and is comparable to the dynamometer card calculated from PHiL simulation results. This indicates that the proposed imitating system can effectively emulate the sucker rod pump working condition.

Since the research deals with modeling, optimal control for energy efficiency operation and emulation of the sucker rod pump, one potential direction for future research could be to study the integration of renewable energy sources to power sucker rod pump drive. The technical and economic feasibility of combination of renewable energy source and storage can be studied using the developed emulating system and simulation model. Another research potential can be thought noting the nature of the load it exerts on the prime mover. The use of proper counterbalance helps to smooth the net torque. However, load fluctuation will remain even if the sucker rod pump is optimally balanced. The effect of load variation on the power quality at the point of common coupling, especially for group of sucker rod pumps supplied from a common point, may not be tolerable. Moreover, reliable supply of such loads is obtained at increased installation cost. Thus, development of control strategies to smooth the net power loading for a group of sucker rod pumps can also be a further research interest.

## References

1. bp Statistical Review of World Energy June 2022. — 2022. — URL: <https://www.bp.com/content/dam/bp/business-sites/en/global/corporate/pdfs/energy-economics/statistical-review/bp-stats-review-2022-full-report.pdf>.
2. Fakher S., Khlaifat A., Hossain M. E., and Nameer H. A comprehensive review of sucker rod pumps' components, diagnostics, mathematical models, and common failures and mitigations // *Journal of Petroleum Exploration and Production Technology*. — 2021. — Vol. 11, no. 10. — P. 3815—3839.
3. Takacs G. Sucker-rod pumping handbook: production engineering fundamentals and long-stroke rod pumping. — Waltham: Gulf Professional Publishing, 2015. — 585 p.
4. Takacs G. A critical analysis of power conditions in sucker-rod pumping systems // *Journal of Petroleum Science and Engineering*. — 2022. — Vol. 210. — P. 110061.
5. Lea J., Pattillo P., Studenmund W. Interpretation of calculated forces on sucker rods // *SPE Production & Facilities*. — 1995. — Vol. 10, no. 01. — P. 41—45.
6. Reges G. D., Schnitman L., Reis R., and Mota F. A new approach to diagnosis of sucker rod pump systems by analyzing segments of downhole dynamometer cards // *SPE artificial lift conference—Latin America and Caribbean, Salvador, Bahia, Brazil*. — OnePetro. 2015.
7. Zhang A., Gao X. Fault diagnosis of sucker rod pumping systems based on Curvelet Transform and sparse multi-graph regularized extreme learning machine // *International journal of computational intelligence systems*. — 2018. — Vol. 11, no. 1. — P. 428—437.

8. Takacs G., Kis L. A new model to find optimum counterbalancing of sucker-rod pumping units including a rigorous procedure for gearbox torque calculations // *Journal of Petroleum Science and Engineering*. — 2021. — Vol. 205. — P. 108792.
9. Neely A., Opal K., Tripp H. Power savings and load reductions on sucker rod pumping wells // *SPE Annual Technical Conference and Exhibition*. — OnePetro. 1989.
10. Neely A. B., Tolbert H. Experience with pumpoff control in the permian basin // *Journal of petroleum technology*. — 1988. — Vol. 40, no. 05. — P. 645—649.
11. Yingli L. et al. A multifunction energy-saving device with a novel power-off control strategy for beam pumping motors // *IEEE Transactions on Industry Applications*. — 2011. — Vol. 47, no. 4. — P. 1605—1611.
12. Jalikop S. V., Scheichl B., Eder S. J., and Hönig S. Computational fluid dynamics model to improve sucker rod pump operating mode // *SPE Annual Technical Conference and Exhibition*. — OnePetro. 2020.
13. Wang Y., Wang S., Yang L., Pu H., and Ling K. A New Model to Evaluate Polished Rod Load of Sucker Rod Pumping System // *SPE Liquids-Rich Basins Conference-North America*. — OnePetro. 2018.
14. Zhang X., Yang X., Guo Z. Kinematics and dynamics analysis of drive mechanism of parallel four-bar energy-saving pumping unit // *Wuhan University journal of natural sciences*. — 2012. — Vol. 17, no. 1. — P. 73—78.
15. Koncz Á. Sucker Rod Pumping Analysis Based on Measured Electrical Parameters : PhD thesis. — University of Miskolc, 2018.
16. Takacs G. Profitability of sucker-rod pump operations is improved through proper installation design // *Latin American and Caribbean Petroleum Engineering Conference*. — OnePetro. 1997.
17. Ganat T. Pumping System of Heavy Oil Production // *Processing of Heavy Crude Oils* / ed. by R. M. Gounder. — Rijeka : IntechOpen, 2019. — Chap. 4.

18. PetroWiki. Hydraulic Pumping. — 2016. — URL: [https://petrowiki.spe.org/Hydraulic\\_pumping](https://petrowiki.spe.org/Hydraulic_pumping) ; (online; accessed: 25.08.2022).
19. Batalović V., Danilović D., Maricic V. K. Hydraulic lift systems with piston type pump // *Journal of Petroleum Science and Engineering*. — 2011. — Vol. 78, no. 2. — P. 267—273.
20. Cholet H. Well production practical handbook. — Editions Technip, 2008. — 546 p.
21. PetroWiki. Progressing cavity pump (PCP) systems. — 2016. — URL: [https://petrowiki.spe.org/Progressing\\_cavity\\_pump\\_\(PCP\)\\_systems](https://petrowiki.spe.org/Progressing_cavity_pump_(PCP)_systems) ; (online; accessed: 25.08.2022).
22. Brown K. E. Overview of artificial lift systems // *Journal of Petroleum Technology*. — 1982. — Vol. 34, no. 10. — P. 2384—2396.
23. Di Tullio M. T., Marfella F. Enhanced Sucker Rod Pumping Model: A Powerful Tool for Optimizing Production, Efficiency and Reliability // *SPE Middle East Artificial Lift Conference and Exhibition*. — OnePetro. 2018.
24. Gibbs S. Predicting the behavior of sucker-rod pumping systems // *Journal of petroleum technology*. — 1963. — Vol. 15, no. 07. — P. 769—778.
25. Wang Dy., Liu Hz. Dynamic modeling and analysis of sucker rod pumping system in a directional well // *Mechanism and Machine Science: Proceedings of ASIAN MMS 2016 & CCMMS 2016*. — Springer. 2017. — P. 1115—1127.
26. Li W., Dong S., Sun X. An improved sucker rod pumping system model and swabbing parameters optimized design // *Mathematical Problems in Engineering*. — 2018. — Vol. 2018. — Article ID 4746210, 15 pages.
27. Xing M., Dong S. An improved longitudinal vibration model and dynamic characteristic of sucker rod string // *Journal of Vibroengineering*. — 2014. — Vol. 16, no. 7. — P. 3432—3448.

28. Shardakov I., Wasserman I. Numerical modelling of longitudinal vibrations of a sucker rod string // *Journal of Sound and Vibration*. — 2010. — Vol. 329, no. 3. — P. 317—327.
29. Xing M. Response analysis of longitudinal vibration of sucker rod string considering rod buckling // *Advances in engineering software*. — 2016. — Vol. 99. — P. 49—58.
30. Lv J., Xing M. Characteristic analysis of longitudinal vibration sucker rod string with variable equivalent stiffness // *MATEC Web of Conferences*. Vol. 153. — EDP Sciences. 2018. — P. 06009.
31. Sun X., Dong S., Liu M., and Zhang J. The simulation model of sucker rod string transverse vibration under the space buckling deformation excitation and rod-tubing eccentric wear in vertical wells // *Journal of Vibroengineering*. — 2018. — Vol. 20, no. 1. — P. 283—299.
32. Huang W., Gao D., Liu Y. A study of tubular string buckling in vertical wells // *International Journal of Mechanical Sciences*. — 2016. — Vol. 118. — P. 231—253.
33. Quang N.P. and Dittrich J.A. *Vector Control of Three-Phase AC Machines: System Development in the Practice*. Vol. 2. — Berlin/Heidelberg, Germany : Springer, 2008. — 340 p.
34. Zheng B., Gao X., Li X. Diagnosis of sucker rod pump based on generating dynamometer cards // *Journal of Process Control*. — 2019. — Vol. 77. — P. 76—88.
35. Vogel J. Inflow performance relationships for solution-gas drive wells // *Journal of petroleum technology*. — 1968. — Vol. 20, no. 01. — P. 83—92.
36. Lv X.-X., Wang H.-X., Xin Z., Liu Y.-X., and Zhao P.-C. Adaptive fault diagnosis of sucker rod pump systems based on optimal perceptron and simulation data // *Petroleum Science*. — 2022. — Vol. 19, no. 2. — P. 743—760.

37. A Special Report from Norris: Sucker Rod Failure Analysis. — available: <https://dokumen.tips/documents/a-special-report-from-norris-sucker-rod-failure-librarynorrisresourcestechnical.html?page=1>.
38. Smith, B., Hall, M., Franklin, A., Johansen, E.S. and Ünalmiş, Ö.H. Field-wide deployment of in-well optical flowmeters and pressure/temperature gauges at buzzard field // Intelligent Energy Conference and Exhibition. — OnePetro. 2008.
39. Wang S.-W. Simultaneous Determination of Reservoir Pressure and Initial Fluid-in-Place From Production Data and Flowing Bottom Hole Pressure— Application // SPE Permian Basin Oil and Gas Recovery Conference. — OnePetro. 2001.
40. Ordóñez B., Códas A., Moreno U. F., and Teixeira A. Sucker-rod pumping system: Simulator and dynamic level control using bottom hole pressure // 2008 IEEE International Conference on Emerging Technologies and Factory Automation. — IEEE. 2008. — P. 282—289.
41. Ordóñez B., Códas A., Moreno U. F. Improving the operational conditions for the sucker-rod pumping system // 2009 IEEE Control Applications,(CCA) & Intelligent Control,(ISIC). — IEEE. 2009. — P. 1259—1264.
42. Shinyakov Y., Sukhorukov M., Torgaeva D., and Soldatov A. Methods and facilities for monitoring the operation of a sucker rod pump // International Journal of Mechanical Engineering and Technology. — 2018. — Vol. 9, no. 1224—1231. — P. 1224—1231.
43. Chevelcha E. Acoustic and Statistical Methods for Sucker Rod Pump States Description : PhD thesis. — University of Leoben, 2014.
44. Allison A. Accurate Load & Position Measurement Is Critical to Quality Dynamometer Analysis // Annual Sucker Rod Pumping Workshop Renaissance Hotel Oklahoma City, Oklahoma. — 2015.

45. Silva W. L., de Souza Netoy D. G., de Almeida Barreto Filho M., Lima A. M. N., and Oliveiray A. Determining the surface dynamometer card of a pumping system from the torque curve of a three-phase induction motor // *Anais do XX Congresso Brasileiro de Automática*, Belo Horizonte. — 2014.
46. Lindh T., Montonen J.-H., Grachev M., and Niemelä M. Generating surface dynamometer cards for a sucker-rod pump by using frequency converter estimates and a process identification run // *2015 IEEE 5th International Conference on Power Engineering, Energy and Electrical Drives (POWERENG)*. — IEEE. 2015. — P. 416—420.
47. Ilyin A., Milovzorov G. and Khakimyanov M. Diagnostics of the condition of sucker-rod pumping units after the analysis of wattmeter cards // *2019 International Conference on Electrotechnical Complexes and Systems (ICOECS)*. — IEEE. 2019. — P. 1—4.
48. Lima F., Guedes L., Silva D. Comparison of Border Descriptors and Pattern Recognition Techniques Applied to Detection and Diagnosis of Faults on Sucker-Rod Pumping System // *Digital Image Processing*. Rijeka, Croatia: InTechOpen. — 2012.
49. Yu Y., Shi H., Mi L. Research on feature extraction of indicator card data for sucker-rod pump working condition diagnosis // *Journal of Control Science and Engineering*. — 2013. — Vol. 2013. — P. 1—6.
50. Zheng B., Gao X., Li X. Fault detection for sucker rod pump based on motor power // *Control Engineering Practice*. — 2019. — Vol. 86. — P. 37—47.
51. Bishop C. M., Nasrabadi N. M. *Pattern recognition and machine learning*. Vol. 4. — Springer, 2006. — 738 p.
52. Li K., Gao X., Tian Z., and Qiu Z. Using the curve moment and the PSO-SVM method to diagnose downhole conditions of a sucker rod pumping unit // *Petroleum Science*. — 2013. — Vol. 10, no. 1. — P. 73—80.

53. Zhou B., Wang Y., Liu W., and Liu B. Identification of working condition from sucker-rod pumping wells based on multi-view co-training and hessian regularization of SVM // 2018 14th IEEE International Conference on Signal Processing (ICSP). — IEEE. 2018. — P. 969—973.
54. Liu J., Feng J., Gao X. Fault diagnosis of rod pumping wells based on support vector machine optimized by improved chicken swarm optimization // IEEE Access. — 2019. — Vol. 7. — P. 171598—171608.
55. Gao Q., Sun S., Liu J. Fault diagnosis of suck rod pumping system via extreme learning machines // 2015 IEEE International Conference on Cyber Technology in Automation, Control, and Intelligent Systems (CYBER). — IEEE. 2015. — P. 503—507.
56. Rogers J., Guffey C., Oldham W. Artificial neural networks for identification of beam pump dynamometer load cards // SPE Annual Technical Conference and Exhibition. — OnePetro. 1990.
57. De Souza A., Bezerra M., Barreto Filho M. d. A., and Schnitman L. Using artificial neural networks for pattern recognition of downhole dynamometer card in oil rod pump system // Proceedings of the 8th WSEAS international conference on artificial intelligence, knowledge engineering and data bases. — 2009. — P. 230—235.
58. Li K., Gao X.-W., Zhou H.-B., and Han Y. Fault diagnosis for down-hole conditions of sucker rod pumping systems based on the FBH-SC method // Petroleum Science. — 2015. — Vol. 12, no. 1. — P. 135—147.
59. Xing M., Dong S. A new simulation model for a beam-pumping system applied in energy saving and resource-consumption reduction // SPE Production & Operations. — 2015. — Vol. 30, no. 02. — P. 130—140.
60. Takacs G. Ways to Decrease Production Costs for Sucker-rod Pumping // Internal report, Petroleum Engineering Department, University of Miskolc. — 2000.

61. Zuo Y., Wu X. A comparative study of four rod load reduction techniques for deep-rod pumping // *Journal of Petroleum Exploration and Production Technology*. — 2018. — Vol. 8, no. 2. — P. 475—483.
62. Zhao X., Han Q., Zhang J., Gao D., and Wang Y. Development of the ZJZ type rod string absorber // *Hydraulics Pneumatics & Seals*. — 2014. — Vol. 34. — P. 45—47.
63. Velichkovich A. Shock absorber for oil-well sucker-rod pumping unit // *Chemical and Petroleum Engineering*. — 2005. — Vol. 41, no. 9. — P. 544—546.
64. Zhao H., Liu F. The application and research of deep pumping technology in TAHE oilfield // *The 5th international symposium of oil and gas reservoir geology and exploitation. Oil and gas reservoir exploitation. Production and operations*. Beijing. — 2009. — P. 919—917.
65. Feng Z.-M., Tan J.-J., Li Q., and Fang X. A review of beam pumping energy-saving technologies // *Journal of Petroleum Exploration and Production Technology*. — 2018. — Vol. 8, no. 1. — P. 299—311.
66. Brown K. E. *The technology of artificial methods*. Vol. 1. — PennWell Books/Petroleum Publishing Co., Tulsa, Ok, 1980. — 720 p.
67. Takács G. *Sucker-rod pumping manual*. — Tulsa, Oklahoma: PennWell Corporation, 2003. — 359 p.
68. Zyuzev A., Bubnov M. SRPU balance monitoring by wattmeter card // *2018 17th International Ural Conference on AC Electric Drives (ACED)*. — IEEE. 2018. — P. 1—5.
69. Gibbs S. G. *Rod pumping: modern methods of design, diagnosis and surveillance*. — Sam Gavin Gibbs, 2012. — 660 p.
70. Solodkiy E.M., Kazantsev V. P. and Dadenkov D. A. Improving the energy efficiency of the sucker-rod pump via its optimal counterbalancing // *2019 International Russian Automation Conference (RusAutoCon)*. — IEEE. 2019. — P. 1—5.

71. Guo X. Energy-saving reconstruction technology of low barbell beam pumping units wells. — *Priv Sci Technol* 21:11–12, 2015.
72. Takacs G., Kis L., Koncz A. The calculation of gearbox torque components on sucker-rod pumping units using dynamometer card data // *Journal of Petroleum Exploration and Production Technology*. — 2016. — Vol. 6, no. 1. — P. 101–110.
73. Shi G., Feng Z., Zhang D., and Jiang M. Influence of inertial load to dynamic characteristic of beam pumping units // *Oil Field Equipment*. — 2015. — Vol. 44, no. 3. — P. 34–37.
74. Jiang M., Cai Y. Study on changes of operation parameters of variable-speed driven pumping wells // *Oil Field Equipment*. — 2010. — Vol. 39, no. 10. — P. 4–7.
75. Li W., Vaziri V., Aphale S. S., Dong S., and Wiercigroch M. Energy saving by reducing motor rating of sucker-rod pump systems // *Energy*. — 2021. — Vol. 228. — P. 120618.
76. *API. Specification for pumping units / API*. — 2008.
77. Bose B. K. *Modern power electronics and ac drives*. Vol. 123. — Prentice hall Upper Saddle River, NJ, 2002. — 728 p.
78. Khakimyanov M. and Khusainov F. Ways of increase energy efficiency of electric drives sucker rod pump for oil production // 2018 X International Conference on Electrical Power Drive Systems (ICEPDS). — IEEE. 2018. — P. 1–5.
79. McCoy G. A., Litman T. and Douglass J. G. *Energy-efficient electric motor selection handbook : tech. rep. / Washington State Energy Office, Olympia, WA (USA)*. — 1990.
80. Gupta V., Tiwari B., Dewangan B. Efficiency optimization of induction motor drive: a review // *International Journal of Innovative Science, Engineering & Technology*. — 2015. — Vol. 2, no. 12. — P. 650–665.

81. Farhani F., Zaafour A., Chaari A. Real time induction motor efficiency optimization // *Journal of the Franklin Institute*. — 2017. — Vol. 354, no. 8. — P. 3289—3304.
82. Hopper W. B., Rajan S. NEMA Standards for Induction Motors and Their Application to the Cement Industry // *IEEE Transactions on Industry Applications*. — 1974. — No. 1. — P. 34—41.
83. Zhang D., Ren Z., Koh C.-S. Multi-objective optimal design of a NEMA design D three-phase induction machine utilizing Gaussian-MOPSO algorithm // *Journal of Electrical Engineering and Technology*. — 2014. — Vol. 9, no. 1. — P. 184—189.
84. Поляков В. Н., Шрейнер Р. Т. Энергоэффективные режимы двигателей переменного тока в системах частотного управления: Учебное пособие. — Екатеринбург : Издательство Уральского университета, 2017. — 260 с.
85. Raj C.T., Srivastava S.P. and Agarwal P. Energy Efficient Control of Three-Phase Induction Motor-A Review // *International journal of computer and electrical engineering*. — 2009. — Vol. 1, no. 1. — P. 61.
86. Abrahamsen F., Blaabjerg F., Pedersen J. K., and Thøgersen P. B. Efficiency-optimized control of medium-size induction motor drives // *IEEE Transactions on Industry Applications*. — 2001. — Vol. 37, no. 6. — P. 1761—1767.
87. Khoury G. Energy efficiency improvement of a squirrel-cage induction motor through the control strategy : PhD thesis. — UNIVERSITÉ DE TOULOUSE, 2018.
88. Hung N. T., Thien N. C., Nguyen T. P., Le V. S., and Tuan D. A. Optimization of electric energy in three-phase induction motor by balancing of torque and flux dependent losses // *AETA 2013: Recent Advances in Electrical Engineering and Related Sciences*. — Springer, 2014. — P. 497—507.

89. Baba A., Mendes E., Razek A. Losses minimisation of a field-oriented controlled induction machine by flux optimisation accounting for magnetic saturation // 1997 IEEE International Electric Machines and Drives Conference Record. — IEEE. 1997. — P. MD1—2.
90. García G. O., Luis J. C. M., Stephan R. M., and Watanabe E. H. An efficient controller for an adjustable speed induction motor drive // IEEE Transactions on Industrial Electronics. — 1994. — Vol. 41, no. 5. — P. 533—539.
91. Mendes E., Baba A., Razek A. Losses minimization of a field oriented controlled induction machine // 1995 Seventh International Conference on Electrical Machines and Drives (Conf. Publ. No. 412). — IEEE. 1995. — P. 310—314.
92. Mohan N. Advanced electric drives: analysis, control, and modeling using MATLAB/Simulink. — John wiley & sons, 2014. — 199 p.
93. Kazmierkowski M. P., Krishnan R., Blaabjerg F. Control in power electronics. Vol. 17. — Elsevier, 2002. — 518 p.
94. Sousa G. C., Bose B. K., Cleland J. G. Fuzzy logic based on-line efficiency optimization control of an indirect vector-controlled induction motor drive // IEEE Transactions on Industrial Electronics. — 1995. — Vol. 42, no. 2. — P. 192—198.
95. Xiaogang F., Boshi C. Constant slip control of induction motor at light load // IECEC 96. Proceedings of the 31st Intersociety Energy Conversion Engineering Conference. Vol. 3. — IEEE. 1996. — P. 1828—1833.
96. Abrahamsen F., Blaabjerg F., Pedersen J. K., Grabowski P. Z., and Thogersen P. On the energy optimized control of standard and high-efficiency induction motors in CT and HVAC applications // IEEE Transactions on Industry Applications. — 1998. — Vol. 34, no. 4. — P. 822—831.

97. Chakraborty C., Ta M. C., Uchida T., and Hori Y. Fast search controllers for efficiency maximization of induction motor drives based on DC link power measurement // Proceedings of the Power Conversion Conference-Osaka 2002 (Cat. No. 02TH8579). Vol. 2. — IEEE. 2002. — P. 402—408.
98. Vukosavic S. N., Levi E. Robust DSP-based efficiency optimization of a variable speed induction motor drive // IEEE Transactions on Industrial Electronics. — 2003. — Vol. 50, no. 3. — P. 560—570.
99. Cacciato M., Consoli A., Scarcella G., Scelba G., and Testa A. Efficiency optimization techniques via constant optimal slip control of induction motor drives // International Symposium on Power Electronics, Electrical Drives, Automation and Motion, 2006. SPEEDAM 2006. — IEEE. 2006. — P. 33—38.
100. Blanuša B., Knezevic B. Simple Hybrid Model for Efficiency Optimization of Induction Motor Drives with Its Experimental Validation. // Advances in Power Electronics. — 2013. — Vol. 2013. — P. 1—8.
101. Branko B. New Trends in Efficiency Optimization of Induction Motor Drives // New Trends in Technologies: Devices, Computer, Communication and Industrial Systems / M. J. Er. — Sciyo, 2010. — P. 341—358.
102. Elfadili A., Giri F., Ouadi H., El Magri A., Dugard L., and Abouloifa A. Induction motor control through AC/DC/AC converters // Proceedings of the 2010 American Control Conference. — IEEE. 2010. — P. 1755—1760.
103. Malinowski M. Sensorless control strategies for three-phase PWM rectifiers : PhD thesis. — Warsaw University of Technology Faculty of Electrical Engineering Institute of Control, Industrial Electronics. Warsaw, Poland, 2001.
104. Sanjuan S. L. Voltage oriented control of three-phase boost PWM converters: design, simulation and implementation of a 3-phase boost battery charger. — Chalmers University of Technology, 2010.
105. Leonhard W. Control of electrical drives. — Springer Science & Business Media, 2001. — 474 p.

106. Mendes E., Razek A. A simple model for core losses and magnetic saturation in induction machines adapted for direct stator flux orientation control // 1994 Fifth International Conference on Power Electronics and Variable-Speed Drives. — IEEE. 1994. — P. 192—197.
107. Ojo J., Consoli A., Lipo T. A. An improved model of saturated induction machines // Conference Record of the 1988 IEEE Industry Applications Society Annual Meeting. — IEEE. 1988. — P. 222—230.
108. Fratila M., Benabou A., Tounzi A., and Dessoude M. Calculation of iron losses in solid rotor induction machine using FEM // IEEE transactions on magnetics. — 2014. — Vol. 50, no. 2. — P. 825—828.
109. Kowal D., Sergeant P., Dupré L., and Vandebossche L. Comparison of iron loss models for electrical machines with different frequency domain and time domain methods for excess loss prediction // IEEE Transactions on Magnetism. — 2014. — Vol. 51, no. 1. — P. 1—10.
110. Rolim L., Miranda U., França B., Fernandes R., and Aredes M. Hardware-in-the-loop evaluation of DSP-controlled converters // 2009 Brazilian Power Electronics Conference. — IEEE. 2009. — P. 805—809.
111. Teclé S. I., Andreevich N. A., Ziuzev A. An Experimental Test Bench for Studying Sucker Rod Pump // 2022 29th International Workshop on Electric Drives: Advances in Power Electronics for Electric Drives (IWED). — IEEE. 2022. — P. 1—6.
112. Žalman M., Macko R. Design and realization of programmable emulator of mechanical loads // IFAC Proceedings Volumes. — 2005. — Vol. 38, no. 1. — P. 246—250.
113. Himani G., Dahiya R. Modelling and Development of Wind Turbine Emulator for the Condition Monitoring of Wind Turbine // International Journal of Renewable Energy Research. — 2015. — Vol. 5, no. 2. — P. 591—597.

114. Rassõlkin A., Vodovozov V. A test bench to study propulsion drives of electric vehicles // 2013 International Conference-Workshop Compatibility And Power Electronics. — IEEE. 2013. — P. 275—279.
115. Oh S. C. Evaluation of motor characteristics for hybrid electric vehicles using the hardware-in-the-loop concept // IEEE transactions on vehicular technology. — 2005. — Vol. 54, no. 3. — P. 817—824.
116. Saarakkala S., Alahäivälä A., Hinkkanen M., and Luomi J. Dynamic emulation of multi-mass mechanical loads in electric drives // Proceedings of the 2011 14th European Conference on Power Electronics and Applications. — IEEE. 2011. — P. 1—10.
117. Akpolat Z. H., Asher G. M., Clare J. C. Dynamic emulation of mechanical loads using a vector-controlled induction motor-generator set // IEEE Transactions on industrial electronics. — 1999. — Vol. 46, no. 2. — P. 370—379.
118. Liu Y., Steurer M., Ribeiro P. A novel approach to power quality assessment: real time hardware-in-the-loop test bed // IEEE transactions on power delivery. — 2005. — Vol. 20, no. 2. — P. 1200—1201.
119. Grubic S., Amlang B., Schumacher W., and Wenzel A. A high-performance electronic hardware-in-the-loop drive-load simulation using a linear inverter (LinVerter) // IEEE Transactions on Industrial Electronics. — 2009. — Vol. 57, no. 4. — P. 1208—1216.
120. Suryanarayanan S., Steurer M., Woodruff S., and Meeker R. Research perspectives on high-fidelity modeling, simulation and hardware-in-the-loop for electric grid infrastructure hardening // 2007 IEEE Power Engineering Society General Meeting. — IEEE. 2007. — P. 1—4.
121. *IEEE*. IEEE standard test procedure for polyphase induction motors and generators / IEEE. — 2004.

122. Rodic M., Jezernik K., Trlep M. Dynamic emulation of mechanical loads—position control approach // Proceedings of 14th International Power Electronics and Motion Control Conference EPE-PEMC 2010. — IEEE. 2010. — S10—23.
123. Rodic M., Jezernik K., Trlep M. Mechatronic systems' control design using dynamic emulation of mechanical loads // *Automatika: casopis za automatiku, mjerenje, elektroniku, racunarstvo i komunikacije*. — 2006. — Vol. 47, no. 1/2. — P. 11—18.
124. Akpolat Z. H., Asher G. M., Clare J. C. Experimental dynamometer emulation of nonlinear mechanical loads // *IEEE transactions on Industry Applications*. — 1999. — Vol. 35, no. 6. — P. 1367—1373.
125. Arellano-Padilla J., Asher G. M., Sumner M. Control of an AC dynamometer for dynamic emulation of mechanical loads with stiff and flexible shafts // *IEEE Transactions on Industrial Electronics*. — 2006. — Vol. 53, no. 4. — P. 1250—1260.
126. Rodic M., Jezernik K., Trlep M. Control design in mechatronic systems using dynamic emulation of mechanical loads // Proceedings of the IEEE International Symposium on Industrial Electronics, 2005. ISIE 2005. Vol. 4. — IEEE. 2005. — P. 1635—1640.
127. Kyslan K. et al. Design and analysis of torque control for load drive with dynamic emulation // 2017 International Conference on Optimization of Electrical and Electronic Equipment (OPTIM) & 2017 Intl Aegean Conference on Electrical Machines and Power Electronics (ACEMP). — IEEE. 2017. — P. 299—304.
128. DAQ M Series: M Series User Manual NI 622x, NI 625x, and NI 628x Multifunction I/O Modules and Devices / National Instruments. — 2016. — URL: <https://www.ni.com/docs/en-US/bundle/pci-pcie-pxi-pxie-usb-62xx-features/resource/3710221.pdf>.

129. ABB. DTC: A motor control technique for all seasons / ABB White Paper. — 2016. — URL: [https://library.e.abb.com/public/0e07ab6a2de30809c1257e2d0042db5e/ABB\\_WhitePaper\\_DTC\\_A4\\_20150414.pdf](https://library.e.abb.com/public/0e07ab6a2de30809c1257e2d0042db5e/ABB_WhitePaper_DTC_A4_20150414.pdf).
130. ABB. ACS580 general purpose drives: Technical eBook / ABB drive technology. — 2017. — URL: [https://library.e.abb.com/public/e670a466d31e469a80e653b759f40091/ACS580\\_technical\\_eBook\\_3AUA0000197173%20RevB\\_EN.pdf](https://library.e.abb.com/public/e670a466d31e469a80e653b759f40091/ACS580_technical_eBook_3AUA0000197173%20RevB_EN.pdf).
131. Ahonen T., Tamminen J., Ahola J., and Niemelä M. Accuracy study of frequency converter estimates used in the sensorless diagnostics of induction-motor-driven systems // Proceedings of the 2011 14th European Conference on Power Electronics and Applications. — IEEE. 2011. — P. 1—10.

## Appendix A

## Sucker Rod Pump Simulator: program registration and Its Interface

## Свидетельство о государственной регистрации программы для ЭВМ

## «Симулятор ШГНУ»

РОССИЙСКАЯ ФЕДЕРАЦИЯ



RU2020666580

 ФЕДЕРАЛЬНАЯ СЛУЖБА  
 ПО ИНТЕЛЛЕКТУАЛЬНОЙ СОБСТВЕННОСТИ  
 ГОСУДАРСТВЕННАЯ РЕГИСТРАЦИЯ ПРОГРАММЫ ДЛЯ ЭВМ

Номер регистрации (свидетельства): 2020666580 Дата регистрации: 11.12.2020 Номер и дата поступления заявки: 2020665912 04.12.2020 Дата публикации и номер бюллетеня: 11.12.2020 Бюл. № 12 Контактные реквизиты: нет	Автор(ы): Семенов Александр Владимирович (RU), Зюзев Анатолий Михайлович (RU), Текле Самуэль Исаак (ER) Правообладатель(и): Федеральное государственное автономное образовательное учреждение высшего образования «Уральский федеральный университет имени первого Президента России Б.Н.Ельцина» (RU)
---	---

Название программы для ЭВМ:  
 Симулятор штанговой глубинно насосной установки.

**Реферат:**

Программа предназначена для анализа режимов работы электропривода скважинного насоса в составе штанговой глубинно-насосной установки. Имеет гибкий и понятный интерфейс, позволяющий выполнить настройку параметров электрической, механической и гидравлической систем комплекса и получить динамические характеристики системы в виде динамограмм и ваттметрограмм. Программа рекомендуется к использованию при проведении проектно-конструкторских работ в области электропривода и для обучения студентов электромеханических специальностей вузов.

**Язык программирования:** Matlab, Simulink

**Объем программы для ЭВМ:** 2019 КБ

A program interface with standard elements such as input fields, inscription, button, tabs is shown in Fig.A.1. The program interface allows the user to navigate through the different subsystems of the sucker rod pump system. Fig.A.2 shows the

tabs where parameters related to the pumping unit and sucker rod string can be entered. Fig.A.3 also shows the tabs where parameters related to subsurface pump and prime mover can be entered.

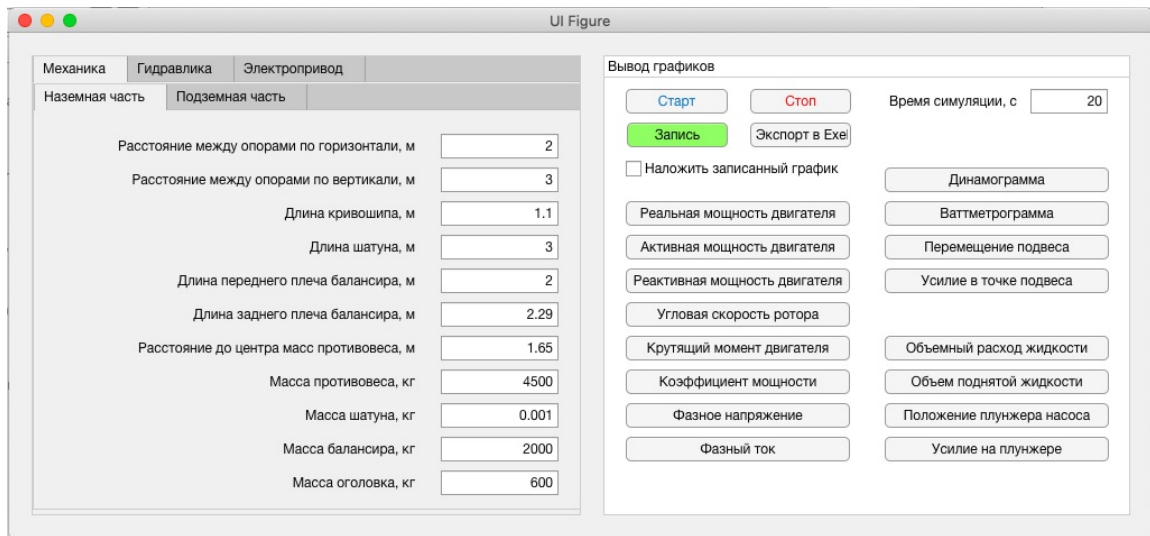


Fig. A.1 — Graphical user interface of the sucker rod pump simulator.

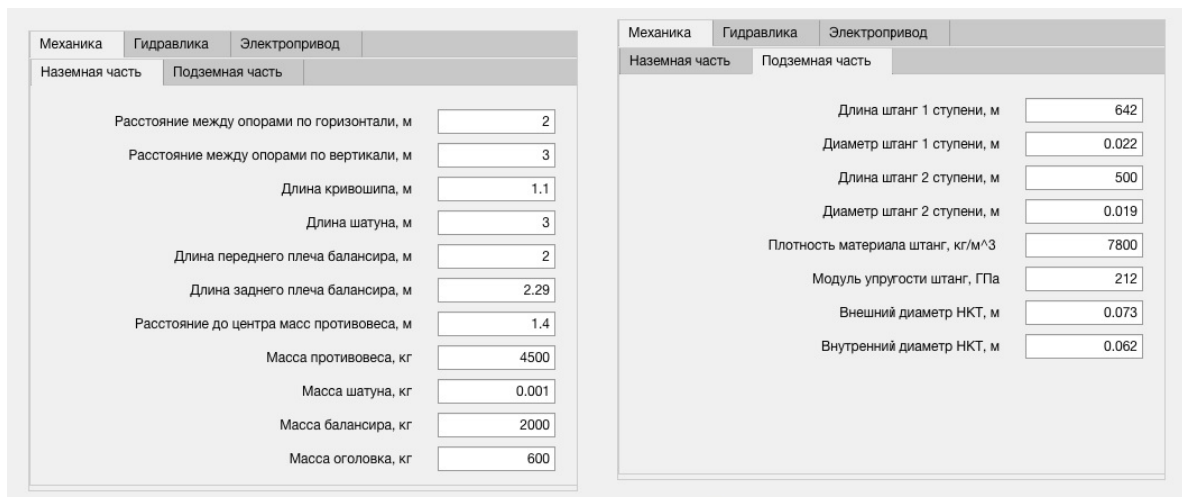


Fig. A.2 — Tabs for entering parameters of pumping unit and sucker rod string.

Механика	Гидравлика	Электропривод	
		Доля газа в нефти, о.е.	0.005
		Площадь утечки в приемном клапане, м <sup>2</sup>	1e-12
		Площадь утечки в нагнетательном клапане, м <sup>2</sup>	1e-12
		Начальное положение плунжера, м	5
		Затрубное давление, Атм	5
		Плотность смеси в НКТ, кг/м <sup>3</sup>	900
		Кинематическая вязкость, м <sup>2</sup> /с	0.0001
		Объемный модуль упругости жидкости, Па	8e+08
		Длина корпуса насоса, м	10
		Диаметр плунжера насоса, м	0.062
		Коэффициент вязкого трения насоса, Н/(м·с)	1500

Механика	Гидравлика	Электропривод	
		Частота сети номинальная, Гц	50
		Мощность номинальная, Вт	3e+04
		Число пар полюсов	3
		Напряжение фазы номинальное, В	220
		Активное сопротивление фазы статора, Ом	0.046
		Активное сопротивление фазы ротора, Ом	0.022
		Реактивное сопротивление рассеяния фазы статора, Ом	0.12
		Реактивное сопротивление рассеяния фазы ротора, Ом	0.13
		Реактивное сопротивление контура намагничивания, Ом	3.7
		Передаточное число редуктора	170

Fig. A.3 — Tabs for entering parameters of subsurface pump and prime mover.

## Appendix B

### Implementation of Results



Утверждаю:

директор ООО «Большие системы»

Вишняков Д. В.

« 15 » « 02 » 2023 г.

#### АКТ

внедрения результатов диссертации Текле Самуэль Исаак  
«Разработка и исследование методов диагностики и повышения  
энергоэффективности штанговых глубинно-насосных установок с приводом  
от асинхронного двигателя», представленной на соискание учёной степени  
кандидата технических наук по специальности 2.4.2 – Электротехнические  
комплексы и системы

На электромеханическом стенде-имитаторе режимов работы штангового насоса, созданном при непосредственном участии Текле Самуэль Исаак, в лаборатории кафедры «Электропривод и автоматизация промышленных установок» УралЭНИН УрФУ выполнено тестирование мобильного комплекса ваттметрирования ШГНУ типа СК ШС-2 (ПКБСК), производимого ООО «Большие системы» для объектов нефтедобычи.

Испытания проводились для случаев различной степени неуравновешенности, которые задавались программной настройкой модели механической части ШГНУ в составе электромеханического стенда.

Результаты испытаний показали полное соответствие оценки степени неуравновешенности, выявленное прибором СК ШС-2 (ПКБСК) и заданное настройкой модели механической части ШГНУ в составе электромеханического стенда, что подтвердило высокую степень достоверности воспроизводимых стендом режимов работы ШГНУ.

Считаем, что разработанный электромеханический стенд-имитатор электропривода ШГНУ и его модификация в виде РНЛ-симулятора могут быть эффективно использованы в практике проектирования, лабораторных испытаний и наладки интеллектуальных станций управления ШГНУ, снижая затраты на проведение полевых испытаний.